3D IMAGING OF WHOLE CELL ULTRASTRUCTURE USING CRYO-ELECTRON MICROSCOPIES

A Dissertation

Presented to the Faculty of the Graduate School

of Cornell University

In Partial Fulfillment of the Requirements for the Degree of

Doctor of Philosophy

by

Jade M. Noble

August 2018

3D IMAGING OF WHOLE CELL ULTRASTRUCTURE USING CRYO-ELECTRON MICROSCOPIES

Jade M. Noble, Ph. D.

Cornell University 2018

Cryo-transmission electron microscopy (cryo-TEM) allows ultrastructural imaging of soft matter materials with high, and often, near-atomic resolution. Imaging whole cells with cryo-TEM, however, requires consideration of the cell's thickness: some cells are naturally electron transparent, while others are too thick for analysis with the TEM. High-resolution imaging, therefore, relies not only on selecting the appropriate microscopy technique, but also on the inherent dimensions of the cell under examination.

This dissertation presents three reports of three cell types with different dimensions. The first report explores the post-insemination phenomenological changes to the spermatozoa of *Aedes aegypti* mosquitoes. Because spermatozoa are naturally electron semi-transparent, we utilized cryo-energy-filtered TEM to produce high-resolution information documenting the removal of the sperm coat and outer membrane. We then describe a correlation between modifications in sperm ultrastructure and motility, and enhanced fecundity in female *Aedes aegypti.*

The second report explores the formation of extracellular vesicles in MCF10A and hyaluronic acid synthase 3 (HAS3)-overexpressed MCF10A cells. Both cell lines are electron-opaque, and their morphologies were examined using florescence, conventional, and cryo-scanning electron microscopies. Using different microscopies elucidated the strengths and limitations of each technique, and how they could be combined to best characterize the effects of HAS3 overexpression on transformed MCF10A cells. Secreted extracellular vesicles were electron-transparent and their surface structures were examined with cryo-TEM. Microvesicles contained surface structure and exosomes did not, providing a pathway for differentiating between vesicle subpopulations in the future.

The third report characterizes the chromatophores of photosynthetic bacteria *Rhodobacter sphaeroides*. Because whole *R. sphaeroides* are too thick to analyze with cryo-TEM, we thinned the cell with cryo-focused ion beam milling. Additionally, we used cryo-electron tomography to understand the 3D arrangement of chromatophores within the cell. We determined that chromatophores adopt both isolated and connected morphologies. Connected chromatophores exist as either budded structures, or linked to neighboring chromatophores through ~10 nm long extrinsic linkers.

Cryo-TEM provides ultrastructural information of cells and cellular components. However, the exact approach depends on the dimensions of the cell and the feature of interest. When carefully chosen, the techniques described in this dissertation provide invaluable insight into cell structure.

BIOGRAPHICAL SKETCH

1. Jade M. Noble was born on the last day of the Twelve Days of Christmas (12 drummers drumming!).
2. The daughter of two members of the United States Air Force, Jade has lived at fourteen permanent addresses in eight states and two countries. She is now a recovering semi-nomadic.
3. She bats left and throws right because Walmart ran out of left-handed gloves the day before the 1997 little league season began.
4. During the first week of August 2011, Jade spent the night on a plane, a train, a subway, the blacktop of a Spanish primary school, and on an airport runway in Madrid.
5. Jade spent the first week of January 2014—including her 23rd birthday—polar vortexed at the Detroit Metropolitan Airport. A big thanks to the USO for providing her with free snacks to hold her over between airport meal vouchers.
6. In 2008, Jade left for New York, where she received a Bachelor of Arts in Chemical Physics from Columbia University in May 2012, a Masters of Science in Chemical Engineering from Cornell University in March 2016, and a PhD in Chemical Engineering from Cornell University in August 2018. The experience has left Jade much more intelligent, but much more liberal than her parents would have preferred.

For the family that can't be with us:

Eugene Noble Sr., Dillard Phifer, Eulately Drummond, Joe Drummond, Myrtle Drummond, and Jeanette Phifer.

Fly high.

ACKNOWLEDGMENTS

A toast to those who have gotten me this far!

To my family, especially Mom and Dad. Thank you for your service. Thank you for not letting me join the Service. To my brother Rome and my niece Kaiya. To my grand- and great-grandparents. You're not with me anymore, but I stand on your shoulders.

To my lab fam: Katie, Berit, Ben, Ismail, Michael, David, Michelle, Duncan, Taylor, and Yue. The PhD program has been a journey, and I couldn't imagine making this journey with anybody else.

To the faculty in the Robert Frederick Smith School of Chemical and Biomolecular Engineering. A special thanks to my committee members, Tobias Hanrath and Matt Paszek. And thank you to Jim Engstrom, Abe Stroock, Susan Daniel, Roseanna Zia, Lynden Archer, Paulette Clancy, Al Center, and Mike Duncan for the kind words and support.

To the PhDs in CBE, especially the members of CEL and ChEGSA. You have been my friends, intramural teammates, fellow croupiers, Fantasy Football rivals, and the best moments of my graduate school career. Cornell CBE is nothing without its PhDs.

To Diversity Programs in Engineering, especially Sara Xayarath Hernandez, Jami Joyner, Alan Zehnder, and Mark Lewis. Thank you for creating a community for me on campus.

To the CCMR staff: John Grazul, Mariena Silvestry-Ramos, and Mick Thomas for their expertise and enduring patience. I have become an expert cryo-electron microscopist (and a better person) because of you.

To my former advisers, Laura J. Kaufman at Columbia University, and Doug T. Petkie at Worcester Polytechnic Institute (formerly at Wright State University). You kick-started my career, and I am grateful. Also, to my K-12 teachers! You never get the appreciation you deserve!

To my friend of 11+ years, Wes Trainum, my best friend Khalilha Haynes and my "special friend" Ethan Degner.

And of course, thank you Lena for giving me a second chance at a graduate school career. A young Neil DeGrasse Tyson wrote about his visit with Carl Sagan in Ithaca: "I knew I already wanted to become a scientist, but that afternoon I learned from Carl the kind of person I wanted to become." I imagine that I feel similarly about another Cornell physicist.

Here here!

TABLE OF CONTENTS

LIST OF FIGURES

LIST OF TABLES

LIST OF ABBREVIATIONS

0D—Zero-dimensional

1D—One-dimensional

2D—Two-dimensional

3D—Three-dimensional

A—Acrosome

Ae. aegypti—*Aedes aegypti*

AN—Axoneme

ART—Algebraic reconstruction technique

ATP—Adenosine triphosphate

BSA—Bovine serum albumin

CA—Centriole adjunct

CAT—Computerized axial tomography

CCD—Charge-coupled device

CM—Cytoplasmic membrane

CMOS—Complementary-metal-oxide-semiconductor

Cryo-CLEM—Cryo-correlative light and electron microscope/y

Cryo-EM—Cryo-electron microscopy

Cryo-ET—Cryo-electron tomography

Cryo-FIB—Cryo-focused ion beam milling

Cryo-FM—Cryo-florescence microscope/y

Cryo-TEM—Cryo-transmission electron microscope/y

CT—Computed tomography

CTF—Contrast transfer function

CW—Cell wall

DAPI—4’,6-diamidino-2-phenylindole

DED—Direct electron detector

DI—Deionized

dpe—Days post-emergence

DQE—Detective quantum efficiency

EFTEM—Energy-filtered transmission electron microscope/y

ET—Electron tomography

ETD—Everhart-Thornley detector

EV—Extracellular vesicle

FEG—Field emission gun

FFT—Fast Fourier transform

FRET—Förster resonance energy transfer

GLM—General linearized model

HAS3— hyaluronan synthase 3

hpm—Hours post-mating

FIB—Focused ion beam

FM—Florescence microscope/y

FOV—Field-of-view

fps—Frames per second

GA—Glutaraldehyde

GIS—Gas injection system

HV—High vacuum

IB—Inclusion bodies

LH—Light-harvesting

LM—Light microscope/y

LSD—Least significant difference

MAP—Monolithic active pixel sensor

MD—Mitochondrial derivative

MFP—Mean-free path

MRI—Magnetic resonance imaging

MTF—Modulation transfer function

MV—Microvesicle

N—Nucleus

NTA—Nanoparticle tracking analysis

OM—Outer membrane

PBS—Phosphate-buffered saline

PFA—Paraformaldehyde

PG—Peptidoglycan

PS—Periplasmic space

PSA—Photosynthetic apparatus

Rba. capsulatus—*Rhodobacter capsulatus*

Rba. sphaeroides—*Rhodobacter sphaeroides*

RC—Reaction center

rcf—Relative centrifugal force

ROI—Region of interest

SC—Sperm coat

SEM—Scanning electron microscope/y

SIRT—Simultaneous iterative reconstruction technique

SNR—Signal-to-noise ratio

SPA—Single particle analysis

TEM—Transmission electron microscope/y

VPP—Volta phase plate

WBP—Weighted backprojection

ZPP—Zernike phase plate

LIST OF SYMBOLS

θ — Tilt angle
c—Speed of light
D—Diameter
δ— Number of connection points between chromatophores and unobserved bonds lying inside the missing wedge
δ_0—Number of missed connections attaching to apparently unconnected chromatophore
eV—Kinetic energy
f—Observed connection of unconnected chromatophores
f_u—Fraction of unconnected chromatophores
h—Planck constant
λ—Wavelength
m—Mass
N_{ob}^0—Number of chromatophores with no observed connections
N_u^0—Total number of unconnected chromatophores
n_{ob}—Observed number of bonds
n_{mw}—Number of missing wedge bonds
p—Momentum
r— Resolution
v—Velocity
V—Voltage

CHAPTER 1

ELECTRON MICROSCOPY FOR THE LIFE SCIENCES

1. 1 Summary

Transmission electron microscopy (TEM; the same abbreviation is used for transmission electron *microscope*) is a powerful tool for interrogating cells and subcellular components. Long used for probing solid-state materials in the materials science community, TEM was recognized early for its potential in cell biology. However, several critical challenges specific to biological specimen had to be addressed:

Biological materials are mostly water, and therefore must be properly fixed before introduction into a vacuum environment. Chemical fixation, the traditional approach, is a harsh method that could lead to the structural alteration of cellular components. Fixation through vitrification preserves the sample in a frozen-hydrated, near-native state without staining, optimally preserving the sample. The sample is then imaged with TEM under cryogenic conditions. This technique is called cryo-TEM.

Organic materials are very sensitive to the electron beam, limiting the maximum tolerable dose that can be used for imaging. Although freezing a sample decreases its beam sensitivity, low-dose imaging methodologies were developed to avoid pre-exposing an area of interest by focusing and correcting the microscope optics in a neighboring area. Additionally, soft matter materials, like cells, are made of low-Z

elements. This fact, combined with low-dose imaging, results in low signal-to-noise ratio (SNR) micrographs. Noisy images of soft materials limit attainable resolution. Much effort has been dedicated to improving the SNR by careful consideration of microscope optics and instrumentation.

The thickness of biological materials varies greatly, from intrinsically electron transparent to too thick for direct imaging in the TEM. Thicker specimens, including many cell types, often need to be thinned before imaging. Cryo-ultramicrotomy uses an oscillating diamond knife to produce ultra-thin sections of vitrified cells. Severe artifacts like sample compression limit the structural analysis of cryo-ultramicrotomed slices. Cryo-focused ion beam (cryo-FIB) milling is an alternative approach that uses a collimated beam of ions to thin a vitrified sample to electron transparency. This technique is much gentler than cryo-ultramicrotomy, and has fewer associated artifacts.

An additional challenge to imaging subcellular components is that transient structural features and cellular processes may be difficult to locate in the electron microscope. Such features are easy to identify with florescent labeling, but florescence microscopy (FM) does not provide the high-resolution imaging conditions necessary for ultrastructural analysis of key structures. Techniques such as cryo-correlative light and electron microscopy (cryo-CLEM) combine the two techniques into an integrated workflow. In cryo-CLEM, vitrified, fluorescently labeled features are identified with cryo-FM. These features are then correlated with low-mag maps of the same grid

imaged with cryo-TEM. Once these regions of interest have been identified, their ultrastructure is probed with cryo-TEM, often with nanoscale resolution.

Finally, cells and subcellular components are 3D objects, and are not sufficiently assessed with 2D projection images. This limitation hinders our understanding of the arrangement and proposed functions of macromolecular assemblies within a cell. 3D imaging modalities like cryo-electron tomography (cryo-ET) have been developed to probe the *in situ* organization of a cell with near-atomic resolution.

The future of cryo-EM depends on the advancement of instrumentation. Next-generation equipment, such as more efficient direct electron detectors and Volta phase plates, will further promote the "resolution revolution" enjoyed in recent years. Techniques such as single particle analysis (SPA) have benefitted from improved instrumentation, and will likely dominate the field for years to come. However, the limitations of SPA in conjunction with the desire to understand how macromolecular assemblies function together within a cell will welcome a more holistic assessment of cellular structures, an approach called molecular sociology.

1.2 Microscopy for Cell Biology

Cell biology has its origins in the 1660's, when Robert Hooke used a compound microscope to visualize what he called "cells," or the cell walls of cork tissue (Mazzarello, 1999). Because these "cells" were dead, they lacked the internal structure and organelles characteristic of living cells. Beginning in the 1670's, Antonie van

Leeuwenhoek used microscopy to describe living cells, including unicellular organisms, bacteria, spermatozoa, and red blood cells (Gest, 2004). He also described larger cellular organelles such as vacuoles (Viotti, 2014). Unfortunately, the resolution of light microscopy (LM) is limited by half the wavelength of light, about 300 nm. While this resolution is sufficient to image tissues and larger cells, resolving cellular organelles and macromolecules presents a formidable—if not impossible—challenge with most light microscopies. One important exception—super-resolution microscopy—pushes the resolution limits of light microscopy, but is beyond the scope of this thesis. However, the reader is encouraged to read a review of the technique authored by (Sydor et.al, 2015).

1.3 Transmission Electron Microscopy

The transmission electron microscope was developed to overcome the resolution limitations associated with LM. The resolving power of a microscope is governed by the wavelength of its photon (light) source. In the 1920's, Louis de Broglie first hypothesized that all matter displays wavelike behavior, including electrons (De Broglie, 1923; De Broglie, 1925). The wavelength of an electron is given by the de Broglie wavelength:

$$\lambda = \frac{h}{p} \quad (1.1)$$

where p is the electron's momentum and h is Planck's constant.

A few years later, Ernst Ruska realized that electrons, which have much shorter wavelengths than light, could be used to produce microscopes with much greater resolving power (Ruska, 1987). Ruska and his collaborator Max Knoll used this concept to develop the first TEM in 1931.

In TEM, the velocity, *v*, of the electrons is modulated by the acceleration voltage *V*, giving the electron a specific kinetic energy, *eV*. From elementary physics, kinetic energy is also equal to one-half the product of the particle's mass *m* and squared velocity. By setting the two expressions for kinetic energy equal to each other, one gets:

$$eV = \frac{1}{2}mv^2 \quad (1.2)$$

Recalling the momentum equation, $p = mv$, one can solve (1.2) in terms of p and substitute the result into (1.1). This equation defines the wavelength of an electron in terms of the acceleration voltage:

$$\lambda = \frac{h}{\sqrt{2meV}} \quad (1.3)$$

When considering relativistic effects, (1.3) becomes:

$$\lambda = \frac{h}{\sqrt{2meV\left(1 + \frac{eV}{2mc^2}\right)}} \quad (1.4)$$

A 300 kV TEM has a theoretical relativistic electron wavelength of 1.97 pm, far smaller than the wavelength of light.

In TEM, a parallel beam of collimated electrons transmits a sample. During transmission, some electrons do not interact with a sample and transmit unaffected until a detector collects them. Other electrons interact with atomic potentials within the sample. This interaction causes the electrons to "bounce off," or scatter, from the potential. If the electron scatters without transferring energy to the atom, it is elastically scattered. If energy transfer occurs, it is inelastically scattered. Inelastically scattered electrons transmit the sample with varying, usually unknown energies and incidence angles. These electrons add noise to the images, and are usually removed by apertures or filters before image formation (Grimm *et al.*, 1998; Williams and Carter, 2009). The energies of both unscattered and elastically scattered electrons are known, and the angle of incidence for elastically scattered electrons can be derived from the law of the conversation of momentum. The detector uses the information about the angle of incidence and the energy of electrons to generate a grayscale image of the collected electrons. The contrast in a TEM image is generated from both amplitude contrast and phase contrast. Amplitude contrast is the dominant source of contrast in stained samples (Nagayama and Danev, 2008), while phase contrast is the dominant

source in unstained samples, including frozen samples (Toyoshima and Unwin, 1988; Nagayama and Danev, 2008).

Although Ruska and Knoll's first TEM had a magnification of 17.4x (Ruska, 1987), modern electron microscopes have magnifications of 1,000,000x or greater and allow for atomic-scale resolution imaging of a material. The electron microscope is arguably one of the most important inventions of the 20th century and is a powerful technique for visualizing atomic structures in the solid-state community. Although a promising technique for cell biology, the inherent nature of soft matter materials posed several critical challenges that had to be addressed.

1.4 Challenge #1: Sample Fixation

To increase the mean-free path of the electron beam, most TEMs operate in a high vacuum (HV) environment. This does not fare well for biological samples, which are up to 70% water. If introduced into a HV, the water in these samples would evaporate, both desiccating the sample and contaminating the pressure within the TEM. Biological samples must be fixed before introduction into the microscope.

1.4.1 Chemical fixation

Conventional sample preparation for TEM involves chemically fixing the sample with aldehydes mixed in buffer, staining with heavy metal ions to improve contrast, dehydrating in graduated concentrations of an alcohol series, embedding in a plastic resin, and microtoming before analysis in the TEM (Karnovsky, 1965; Bainton et al.,

1971). This technique, called chemical fixation, has been used for decades to explore the structure of cells. However, it is a harsh processing method with several limitations to consider (Hayat, 1986). If staining whole cells, it is unlikely that one fixation protocol will uniformly both fix and stain all of the cell's subcellular constituents. It is likely that some organelles will preferentially fix and stain, and some will not. Chemical fixation and dehydration can also lead to cell swelling or shrinkage; degradation or rearrangement of key cellular structures. A combination of the chemical processing and uneven staining may make data interpretation challenging. For nanoscale visualization of subcellular structures, it is critical that the cell remains unaltered by the sample preparation process.

1.4.2 Vitrification

Vitrification is the conversion of a liquid into an amorphous solid. Biological materials are embedded in a layer of glassy instead of crystalline ice because water expands as it crystallizes, damaging the sample. When vitrified, samples are preserved in a hydrated, "near-native" condition. Because the density of biological materials is greater than water, the sample can be visualized without staining. Humberto Fernández-Morán proposed vitrification as an alternative to traditional fixation methods in the 1960's (Fernández-Morán, 1960), but the technique's potential was not realized until the 1970's, when Taylor and Glaeser vitrified catalase crystals for electron microscopy diffraction experiments in cryogenic conditions (Taylor and Glaeser, 1974). This paper marked the advent of cryo-TEM for the life sciences. In the 1980's, Jacques Dubochet and colleagues developed protocols for biological sample

preparation for cryo-TEM studies (Dubochet and McDowall, 1981). By the 1990's, sample fixation by vitrification was commonplace. Now, vitrification and cryo-TEM are ubiquitous techniques for understanding cellular structure and function in their native context.

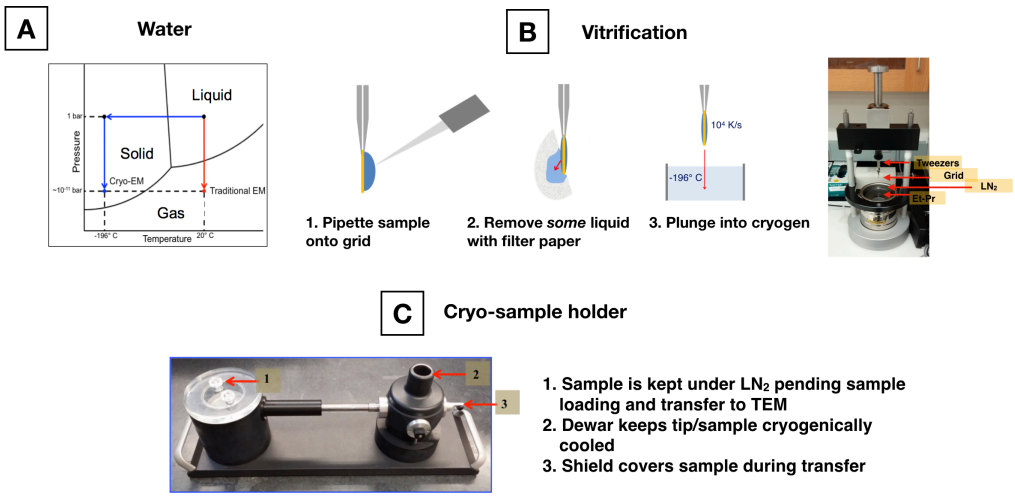

Fig. 1.1. Sample preparation for cryo-TEM. Samples prepared for cryo-EM are fixed in an amorphous layer of ice, which is achieved by freezing samples below the devitrification temperature at a rate that prevents the formation of a crystalline lattice associated with normal ice (A). Samples are vitrified by pipetting samples onto a TEM grid, blotting away excess liquid, and rapidly freezing into a cryoprotectant cooled to liquid nitrogen temperatures. Vitrification is achieved with either homemade or commercialized apparatuses (B). Samples remain under cryogenic conditions through the use of specialized cryo-EM holders and workstations, which themselves are cooled with liquid nitrogen (C). This prevents devitrification and recrystallization of the sample.

Although pure water must be cooled to below the vitrification temperature of -135 $^{\circ}$C at a rate of $\sim 10^{5}$–10^{6} K s^{-1} to prevent the formation of crystalline ice (Brüggeller and

Mayer, 1980), biological samples can be cooled at slower rates ~10^4 K s^{-1}. Plunge freezing is the standard method of sample vitrification for biological materials. In this method, a small amount (2-5 μL) of sample suspended in buffer is applied to a holey carbon electron microscopy grid. Alternatively, cells can be cultured directly onto the EM grid. Excess solution is blotted from the grid with filter paper, leaving the sample immersed in a thin liquid layer on the grid. The sample is rapidly plunged into a cryoprotectant (such as an ethane-propane mixture) cooled by liquid nitrogen. Plunge freezing is an automated procedure that can be performed with either homemade or commercialized apparatuses. This procedure is summarized pictorially in Fig. 1.1B. Plunge freezing has a reliable penetration depth of ~10 μm, so thinner cells are successfully vitrified with this technique. Thicker cells may only partially vitrify, and crystallization of water in the remaining parts may propagate to damage the specimen. For thicker samples, high-pressure freezing (HPF) is a suitable alternative. HPF involves freezing samples at 2 kbar and below the devitrification temperature (Moor, 1987). These conditions suppress crystalline ice formation up to a depth of ~ 10 μm (Sartori *et al.*, 1993; McDonald and Auer, 2006).

Vitrified samples must be stored in liquid nitrogen to prevent devitrification of the amorphous ice layer. The sample must also remain in cryogenic conditions during transfer into the electron microscope and imaging. To this end, vitrified EM grids are loaded under liquid nitrogen into specialized holders, which are also cooled by liquid nitrogen. The holders are designed to keep the sample fixed during image acquisition

via a miniature liquid nitrogen dewar that is refilled every few hours. An example of such a holder is seen in Fig. 1.1C

1.5 Challenge #2: Sample Sensitivity

Biological materials are highly sensitive to beam irradiation. Radiation damage is the greatest challenge to imaging cellular structure with sub-nanometer resolution (Glaeser, 2008). Electrons that interact with organic specimen inelastically scatter, ionize, and break chemical bonds. Secondary effects include the formation of free radical species, sample heating, and molecular fragmentation and diffusion (Carlson and Evans, 2012). All of these effects contribute to sample damage and significantly lower image resolution.

Sample sensitivity is additional motivation for vitrifying biological samples. The amorphous layer of ice acts as a cryo-protectant and increases the sample's resilience to the electron beam. Additionally, lowering the temperature at which samples are imaged also improves beam sensitivity. Vitrified samples imaged in cryogenic conditions have a 2-to-6-fold increase in radiation tolerance over those imaged in room temperature conditions (International Study Group, 1986; Frank, 2006). Specimen cooling delays—but does not prevent—irradiation damage. The maximum tolerable dose of an organic specimen is about 100 $e^-/Å^2/s$ (compared to the critical dose of solid state specimen, ~10^9 $e^-/Å^2/s$).

1.5.1 Low Dose Imaging Methodologies

Low-dose approaches were developed to search for a region of interest (ROI) on the grid and focus without unnecessarily exposing the ROI before image acquisition. Most microscopes have low-dose imaging software. On the FEI Titan Themis (FEI, Eindhoven, Netherlands), Low Dose mode is partitioned into three sections: Search, Focus, and Exposure modes. Search mode is a low-magnification setting used to locate an ROI. Because the ROI is pre-exposed, the total dose in Search mode should be no more than 0.1 $e^-/Å^2/s$. The images in Search and Exposure modes are aligned so that the ROI located in Search mode is the one imaged in Exposure mode. Because of the low magnification and low dose, the defocus in Search mode is high (-20 μm or more) to enhance contrast.

In Focus mode, the image is properly focused and astigmatism is corrected. The Focus magnification should be the same or slightly greater than the Exposure magnification, but the spot size or beam intensity should be set so that the dose on the sample is high enough to focus. This dose can be—and usually is—much higher than the Exposure dose. Because of the high dose requirement, Focus mode is usually operated in a region close to, but far enough away, from the ROI so that the focus is accurate but pre-exposure will not damage the ROI. The microscope will apply the defocus value in Focus mode to Exposure mode.

Exposure mode is where the image is acquired. For cryo-EM, Exposure mode is set to an intermediate magnification (25-91kx) for whole cell imaging, but with a dose below the critical dose. Low Dose saves individual lens settings for Search, Focus, and

Exposure modes, eliminating the need to readjust the optics between settings. If Low Dose was set up and used properly, the ROI in Exposure mode would have had less than 0.5 $e^-/ Å^2/s$ of pre-exposure before image acquisition.

1.6 Challenge #3: Low Signal-to-Noise Ratio Micrographs

Cryo-EM specimens contain low-Z elements that interact weakly with impinging electrons. Embedding samples in ice further reduces the contrast in electron micrographs. This, combined with the low dose imaging requirement, means that most cryo-electron micrographs will have a low SNR. Increasing the electron dose results in sample damage and is not an appropriate solution.

1.6.1 Adjusting the Microscope Optics

The most straightforward approach to increasing the SNR in images is by adjusting the microscope optics. Changing the image defocus alters the contrast transfer function (CTF), which mathematically describes the amount of information transfer as a function of spatial frequency. Larger defocus will improve contrast, but at the expense of eliminating high-resolution information in the image (Kourkoutis *et al.*, 2012). Using an objective aperture will increase contrast by removing the high-frequency information that contributes to noisy images, but also at the expense of decreased maximum resolution (Cheng *et al.*, 2015). In the case of whole cells or large macromolecular structures, which are limited to molecular resolution, larger defoci are often used to increase contrast without a significant compromise in resolution. These

effects become more important when imaging smaller or lighter biomolecules with nanoscale resolution.

1.6.2 Electron Source

Choosing the appropriate instrumentation is another means of increasing image contrast. The microscope's electron source is an important consideration. There are two kinds of electron sources: thermionic sources and field-emission sources (Williams and Carter, 2009). On the microscope, these sources are contained within an apparatus called an electron gun. The electron gun generates an electron beam by emitting and accelerating electrons through a potential. A thermionic gun will contain either a tungsten filament or lanthanum hexaboride (LaB_6) crystals (Williams and Carter, 2009). Field emission guns (FEGs) A FEG contains a tungsten source. FEGs are preferred because they are brighter and more temporally coherent than thermionic sources (Thompson *et al.*, 2016). Both parameters allow for a beam with small energy spread, which allows for high-resolution, high-contrast imaging in cryo-EM by limiting the effect of chromatic aberration on the final image.

1.6.3 Direct Electron Detectors

Cryo-electron micrographs are intrinsically noisy due to sample sensitivity and low critical doses. Another source of noise in the micrograph is from the detector. An ideal detector would contribute no noise to the image, but such a detector does not exist. Careful consideration of electron detectors could reduce the amount of noise in a cryo-micrograph and improve the SNR.

The performance of a detector is determined by two metrics: the modulation transfer function (MTF) and the detective quantum efficiency (DQE). The MTF measures how much contrast is transferred from the specimen to the image at a specific resolution. The MTF is modulated by parameters such as pixel size and shape (Chen *et al.*, 2000; Karimzadeh, 2014). A more important metric for low-dose imaging is the DQE, which mathematically describes the amount of noise a detector contributes to an image during signal conversion (Faruqi and McMullan, 2011) . The DQE is defined as the ratio of the square of the output signal to the square of the input signal:

$$DQE = \frac{SNR_o^2}{SNR_i^2} \quad (1.5)$$

In pixelated detectors, the maximum spatial frequency recorded by a detector is limited by the pixel size, since the shortest wavelength must be sampled twice (McMullan *et al.*, 2016). This limit is the Nyquist frequency, or the inverse of twice the detector pixel size. DQE is most commonly stated in terms of one-half Nyquist.

The first cryo-EM datasets were collected on photographic film (Henderson, 1990). Despite its widespread use, data acquisition on film had its disadvantages (Vinothkumar and Henderson, 2016). Long acquisition times resulted in sample drift and blurry images, and the contrast in film is poor at lower frequencies. To improve contrast, the image had to be greatly defocused (Cheng *et al.*, 2015), generating lower-

resolution images. Finally, photographic film had to be developed before viewing, prohibiting automated data collection (Wu *et al.*, 2016).

Beginning in the 1990's, scintillator-based technologies such as charged-coupled device (CCD) cameras were explored as alternatives to photographic film (Krivanek and Mooney, 1993). In CCDs, primary electrons impinge on a phosphor scintillator, generating photons that are converted into an electronic signal. The signal is transferred through lenses or fiber optic cabling to the CCD sensor, where it is digitized into an image (Clough *et al.*, 2014). CCD cameras allow for automated data acquisition and immediate image visualization. Faster acquisition times and improved contrast at lower frequencies resulted in cryo-micrographs with less drift and defocus, ultimately improving the resolution of the image.

A major disadvantage is that CCDs operate as indirect electron detectors because the CCD sensor is easily damaged when directly exposed by primary electrons (Roberts *et al.*, 1982). The primary electrons scatter when incident on the scintillator, reducing spatial variation and lowering the MTF and the DQE of the CCD camera (Clough *et al.*, 2014). The effect is that CCD cameras performed only moderately better than photographic film at low frequencies and accelerating voltages (80-100 kV), and photographic film outperforms CCD cameras at high frequencies and acceleration voltages (McMullan *et al.*, 2016). For example, the DQE of a CCD camera at 300 kV—a very common acceleration voltage for cryo-EM data collection—was 7-10% at half-Nyquist, while for photographic film at this acceleration voltage was 30-35%

(McMullan, Chen, *et al.*, 2009). For these reasons, film was the detector of choice for high-resolution cryo-EM studies until the mid-2010's (for example, Zhang *et al.*, 2010; Grigorieff and Harrison, 2011).

Nevertheless, CCD cameras routinely generate cryo-electron micrographs with nanoscale resolution, and their use in automated data acquisition has proven invaluable for cryo-EM experiments. CCD cameras have now replaced photographic film on most modern instruments.

Over the last decade, the "resolution revolution" of cryo-TEM has been attributed in part to the advent of direct electron detectors (DEDs). Primary electrons impinge directly onto a sensor, eliminating the need for photoconversion by a scintillator (Wu *et al.*, 2016). DEDs rely on complementary-metal-oxide-semiconductor monolithic active pixel sensors (CMOS/MAPs) technology, which is more resilient to beam irradiation than CCDs (McMullan *et al.*, 2014). DED sensors detect electrons directly as they pass through a lightly-doped silicon epilayer supported on a highly-doped silicon substrate. Some incident electrons are backscattered from the substrate and pass through the epilayer a second time, which can create noise (McMullan, Chen, *et al.*, 2009). Consequently, substrates are backthinned to about 30 μm, which can increase MTF, DQE, and the lifetime of a DED at least twofold (McMullan, Faruqi, *et al.*, 2009; McMullan *et al.*, 2016). Most modern DEDs have higher DQEs than either CCDs or film (McMullan *et al.*, 2014).

DEDs operate in either integrating or counting mode. In integrating mode, the total charge deposited on the detector by each electron is integrated to form the final image (Wu *et al.*, 2016). This approach is fast and amenable to high-dose imaging. However, the variation in charge deposited by each primary electron while interacting with the sensor is not removed from the image in integration mode. This can lead to a higher DQE than a CCD camera, but lower than theoretically possible with a direct detector.

In counting mode, each incident electron is individually detected and localized when it strikes the detector (Wu *et al.*, 2016). Detecting individual electrons is made possible by a high camera speed (< 300 fps). In this mode, each primary electron event is represented as a single count in a single pixel or sub-pixel. Counting mode significantly increases the DQE for low-dose imaging.

The benefits to using DEDs over traditional cameras are manifold. The high frame rate allows DEDs to partition the dose between frames, creating movies of the imaged object. Each frame can be aligned, correcting for sample drift and increasing both SNR and resolution. Images with beam damage or high-frequency noise can be removed from the movie. The disadvantages of using DEDs arise primarily from operating the detector in counting mode. The saturation dose is significantly lower than in integration mode, primary to avoid coincidence loss. Frames with doses less than 0.03 e^-/px/400 Hz are reasonable. To compensate for lower doses, longer acquisition times are necessary. This can lead to longer experiments with larger data sets.

1.7 Challenge #4: Specimen Thickness

Biological materials span a wide range of thicknesses, from inherently electron transparent to too thick for direct imaging in the TEM. High-resolution imaging of thicker specimen, such as cells, is challenging since the specimen thickness is greater than the inelastic MFP of electrons in the specimen, about ~ 350 nm for a 300 kV source (Grimm *et al.*, 1996). Electrons incident on a thicker sample undergo multiple inelastic scattering events through the specimen volume, resulting in loss of coherence and compromised resolution in those regions. Structural biology studies of whole cells are often limited to medium-resolution imaging of "semi-thick" cells or the electron-transparent peripheral regions of thick cells.

1.7.1 Energy-Filtered Transmission Electron Microscopy

Zero-loss energy filtering can remove inelastically scattered electrons with energies outside of a certain range. These electrons do not contribute to the recorded image, resulting in higher image contrast. Energy-filtered transmission electron microscopy (EFTEM) is particularly useful for specimens that are slightly thicker than the inelastic MFP, about 500 nm - 1 μm. For biological specimen with thicknesses about a micron or more, additional sample preparation is required before analysis with the cryo-TEM. Techniques for thinning cells are abundant, and include freeze fractionation, cryo-ultramicrotomy, and cryo-focused ion beam milling.

1.7.2 Freeze Fractionation

In freeze-fractionation, cells are either plunge- or high-pressure frozen to immobilize cellular components. The vitrified specimens are then fractured with a microtome along a plane through the cell. The cells cleave into fragments, revealing interior constituents. After cleaving, the exposed surfaces are coated with a layer of platinum film. The film creates a stable replica of the surface. Acid is used to digest any organic material attached to the platinum cast, which is then carbon-coated. The replica is then introduced into the electron microscope for analysis (Severs, 2007). Freeze fractionation has been particularly useful for understanding the arrangement and organization of cellular membranes, but artifacts can come from specimen pre-preparation (ie, vitrification or chemical fixation), the fractionation process, and the replica creation process (Sleytr and Robards, 1982). Consequently, this technique often results in non-uniform, unpredictable fractionation characteristics and the formation of irreproducible casts.

1.7.3 Cryo-Ultramicrotomy

In cryo-ultramicrotomy, vitrified samples are thinned to electron transparency with an oscillating diamond knife. Cryo-ultramicrotomy can produce ultrathin (< 70 nm) slices of the original cellular volume, but is prone to severe artifacts, such as compression along the sectioning direction, variable section thickness, chattering, and knife marks (Al-Amoudi et al., 2005; Han et al., 2008; Pierson et al., 2011). This effect becomes more pronounced for slices thicker than 100 nm

1.7.4 Cryo-Focused Ion Beam Milling

An alternative technique is cryo-FIB milling. Cryo-FIB milling results in electron-transparent regions that can then be directly imaged in the TEM. In the case of cells, cryo-FIB accesses cytoplasmic content that would have otherwise been inaccessible in cryo-TEM due to specimen thickness. Cryo-FIB is a comparatively gentle technique that does not create compression artifacts and knife marks associated with cryo-ultramicrotomy. Furthermore, the penetration depth of implanted Ga^+ ions is limited to the first 5-20 nm of most biological samples, and localized heating has negligible effect on the thinned sample (Marko et al., 2006; Ziegler, 1988). The consequence is excellent preservation of the cellular landscape and, in the case of thicker cells, access to subcellular components. Thinned specimens are either imaged with the scanning electron microscope (SEM) inside the dual-beam setup (as in serial block-face milling), or transferred to a TEM.

1.7.4.a Operating Principle

Cryo-FIB is typically a dual-beam setup consisting of an SEM and a FIB (Fig. 1.2A). Most systems also include a gas injection system (GIS), which contains organometallic platinum. During cryo-FIB milling, ions are generated by a liquid metal ion source and extracted by an extraction electrode located near the top of the ion beam column. The ions are collimated into a beam by electromagnetic lenses. The beam is then further focused through electrostatic lenses and apertures before reaching the sample. Although other ion species can be used, gallium is the most common

source because of its low vapor pressure, melting point, and volatility. A more detailed description of the SEM/FIB instrument is found in (Rigort and Plitzko, 2015).

The operating principle of cryo-FIB is as follows: The SEM is used to navigate a vitrified grid and to find an ROI. The ROI is coated with 1-2 μm thick layer of platinum from the GIS. This platinum layer acts as a protective capping layer for the milled surface. However, it is unlikely that the deposited platinum layer is uniform or smooth. A rough capping layer will result in a non-uniform milling rate, and a nonhomogeneous final product. One can smooth the capping layer by exposing it to the ion beam at a relatively high current (~1 nA) for 30 seconds (Hayles *et al.*, 2007).

1.7.4.b Milling a Sample

Cryo-FIB then employs a beam of highly collimated Ga^+ ions to site-specifically sputter surface atoms away from an ROI on the grid (Fig. 1.2B-C). Samples can be milled into different geometries. A lamella is a thin film of uniform thickness, while a wedge is a milled slice of a gradient thickness. Milling for both geometries starts with drawing a milling rectangle below the ROI (wedge) or both above and below the ROI (lamella). The rectangles are typically ~10 μm long and ~5 μm wide, although there is some creative liberty with milling dimensions. The milling direction is set top-to-bottom for one rectangle, and bottom-to-top for the other to prevent redeposition of ablated material.

Once the rectangles have been defined and the proper current and voltage set, the user may press the "play" button on the FIB software interface to watch the milling in real time. When thinning soft-matter material, the milling voltage is set and usually remains at 30 kV. The milling current is incrementally reduced as more material is sputtered away from the thinned specimen. For the initial cleaning steps, starting currents in cryo-FIB can be as high as 0.2 nA. During milling, users should pay special attention to evidence of charging, drift, and astigmatism, as these poor milling conditions will likely lead to artifacts in the thinned specimen.

The milling is complete when the material within the milling rectangles has been completely removed. To observe progress, users can take single scan images in the ion beam window or live image in the electron beam window. In subsequent milling steps, the height of the milling rectangle is reduced and the current is iteratively lowered. The lowest milling current is reserved for the final cleaning steps with the intention of producing a uniform, smooth milled surface. An example of graduated milling currents is 0.2 nA, 49 pA, and 9 pA.

The final thickness of a lamella is 200-500 nm thick. This can be estimated by measuring a profile of the lamella captured by a single-frame image in the ion beam window.

1.7.4.c Cryo-FIB Milling for Cells

Since the first successful cryo-FIB experiment on a biological specimen, (Moulders, 2003), the technique has been used to probe the molecular machinery of both prokaryotic and eukaryotic cells (Rigort *et al.*, 2012; Noble *et al.*, 2017). The technique is often combined with cryo-ET and subtomogram averaging to provide 3D visualization of cellular components (Engel et al., 2015; Mahamid et al., 2016; Marko et al., 2007). Many cryo-FIB experiments are now performed on cells cultured directly onto TEM grids (for example,

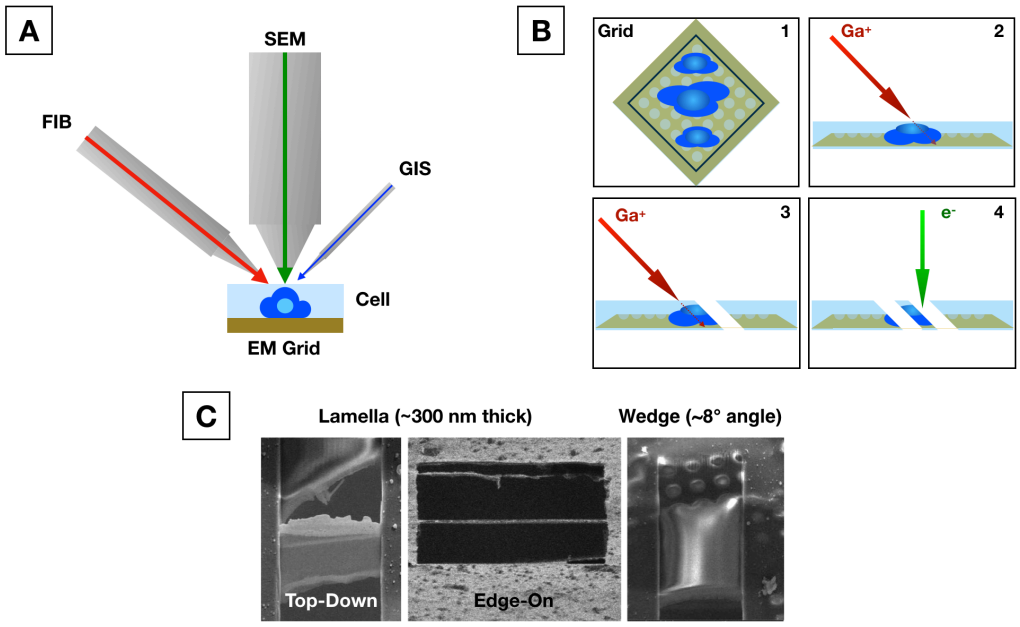

Fig.1.2. Cryo-focused ion beam milling schematic. The cryo-FIB is typically a dual-beam setup consisting of a scanning electron microscope (SEM) and a FIB (A). The SEM is used to navigate a vitrified grid and find an area of interest. The cryo-FIB then site-specifically mills material away from a region of interest. This is seen schematically in B. A beam of gallium ions impinges on the surface, sputtering material from that region. One can mill into two different geometries. The wedge geometry is seen in B.3, and the lamella is seen in B.4. An SEM image of both geometries is also seen in C.

(Mahamid et al., 2016)). This reduces the probability of morphological changes resulting from collecting and pelleting cells cultured in a Petri dish.

1.7.4.d Cryo-FIB Lift-Out

A more recent advance is cryo-FIB lift-out, an analogue of the lift-out technique routinely employed in the materials science community. Lift-out involves milling a lamella from a localized region of bulk material and removing that lamella with a sharp metal needle. The lamella is then transferred to a specialized TEM grid (Overwijk *et al.*, 1993). Cryo-FIB lift-out remains underutilized in the life sciences community because of its technical difficulty. One challenge is keeping the lamella below the devitrification temperature while transferring to the TEM grid. Nevertheless, proof-of-concept studies have demonstrated cryo-FIB lift-out as a viable technique with significant promise in future studies (Mahamid *et al.*, 2015; Parmenter *et al.*, 2016; Zachman *et al.*, 2017).

1.7.4.e Experimental Considerations

Although cryo-FIB has increasingly become the preferred sample thinning technique, there are important considerations to keep in mind. Cryo-FIB can introduce artifacts, such as redeposition of sputtered material onto the milled surface. Most cryo-FIB setups have an anticontaminator to mitigate this problem. Curtaining may also occur, though depositing a platinum capping layer can protect against curtaining artifacts. Another potential drawback to cryo-FIB is that it is a time-consuming, costly

technique. An expert cryo-FIB user can mill only a handful of lamellae a day. However, if the cell density on the TEM grid is sufficiently high, one can thin several cells with a single lamella. For an example, see Figure 3 in (Villa *et al.*, 2013).

One final consideration is that special precaution must be taken to ensure that the milled samples are not contaminated during transfer from the SEM/FIB setup. Assuming the FIB is under sufficient vacuum, the best protection against this artifact is user experience, especially with sample handling and transfer.

1.8 Challenge #5: Localizing Features of Interest

Cellular processes are both spatial and temporal events. Often, the structures of the macromolecules associated with these processes are rare or transient. Finding these structures in cryo-EM can be prohibitively challenging due to the limited FOV. Furthermore, contrast variations in cryo-micrographs can help determine the presence of the structure, but not its identity. Florescent labeling can localize dynamic processes and specific macromolecules, but high-resolution imaging is difficult with cryo-FM. One approach is to combine the strengths of both techniques into an integrated workflow. This technique is called cryo-correlated light and electron microscopy. In cryo-CLEM, structures of interest are fluorescently labeled and identified with cryo-FM. Identified structures are then imaged with high-resolution using cryo-TEM.

1.8.1 Cryo-CLEM

In cryo-CLEM, features and phenomena of interest are identified through florescent labeling of previously vitrified samples. Once the feature of interest has been identified, high-resolution imaging of that feature is performed with cryo-TEM. The challenge of identifying the same feature of interest after transferring between microscopes is nontrivial. Because florescent markers do not appear in cryo-EM images, one strategy is to image the same sample on the two separate instruments and use grid landmarks or fiduciary markers to correlate the image maps acquired in the different imaging systems. Once the images from the different instruments have been correlated, one should be able to target the feature of interest and image in high-resolution with cryo-TEM.

The drawbacks are the possibility of contamination while transferring a sample between instruments and the possible challenge of correlating images between the two microscopes. An additional challenge for samples that are not fixed before imaging with FM is that one will have to account for the shifting of cells on a grid due to the plunge freezing process. Consequently, most cells are vitrified before florescent imaging. Studies have shown that not only will vitrified samples fluoresce, but photobleaching is significantly reduced (Schwartz et al., 2007).

Cryo-CLEM is most commonly combined with cryo-EM and cryo-ET, but the technique can also be combined with cryo-FIB (Rigort *et al.*, 2010; Arnold *et al.*, 2016). Because a small slice is milled from the larger cellular volume, it is important

to know the relevant features have been captured within the lamella. Cryo-CLEM is used to inform the experimenter precisely where to mill to capture the features and processes of interest. Cryo-CLEM is a developing field, but has already provided a key role in providing information on the ultrastructural underpinnings of dynamic cellular events.

1.9 Challenge #6: Visualizing Structures in 3D

Unlike the ultrathin, 0D, 1D, and 2D materials commonplace in the physical sciences, cells are 3D objects whose structures cannot be fully interpreted with a single 2D projection image. Without a 3D visualization of the cell, the structure and function of macromolecular assemblies cannot be understood in their native context. As mentioned in section 1.6.3, single particle techniques are not particularly useful for cells. Another technique—cryo-electron tomography (Baumeister *et al.*, 1999)—does not rely on purified or high symmetric structures, and is well-poised for *in situ,* 3D analysis of whole cells and cellular landscapes.

1.9.1 Cryo-Electron Tomography

Computed tomography (CT) is more common in the medical community, where 3D imaging techniques such as computerized axial tomography (CAT) scans and magnetic resonance imaging (MRI) are routine. In CAT scans and MRIs, the patient remains still, and the beam of X-rays rotate around the patient, generating 2D images of the patient acquired from different angles. In ET—where specimen comfort is certainly not a consideration—the object of interest is rotated while the beam remains

fixed. Beyond this difference, medical CT and ET are remarkably similar, and even employ some of the same 3D reconstruction algorithms.

1.9.1.a Data Acquisition and Alignment

Experimentally, ET and cryo-ET operate the same: 3D information is obtained by collecting a series of 2D projection images of an object as it is incrementally rotated about its tilt axis in the electron microscope. The resulting collection of 2D projection images is called a "tilt series." In cryo-ET, samples are vitrified, and manually adjusting the optics during acquisition risks overexposing the sample. Most cryo-tilt series are acquired through an automated procedure operating in low dose mode. The software identifies and corrects for the apparent shifting of the object during tilting, autofocuses in an adjacent region to the object, and records a projection image (Dierksen *et al.*, 1992).

Mechanical instabilities in both the sample holder and the microscope stage (primarily backlash as the stage is tilted) can cause the object of interest to shift within the FOV between images. The individual images in the tilt series must be computationally aligned to a common axis of rotation post-acquisition. This is best done through fiduciary markers, such as gold nanoparticles, that were introduced to the sample just before vitrification.

The aligned tilt series is reconstructed *in silico* to form a 3D density map of the object. The ability to derive 3D information from 2D projection images is explained by the

Fourier Projection Theorem (Crowther *et al.*, 1970). The theorem states that the Fourier transform of a projection image of an object acquired at tilt angle θ corresponds to a central slice through the object's 3D Fourier space at that same angle. Experimentally, one can populate an object's 3D Fourier space by taking the Fourier transforms of a collection of 2D projection images acquired at different angles. An inverse Fourier transform of the sampled 3D Fourier space will produce a 3D reconstruction of the object in real space. An overview of the cryo-ET workflow is seen in Fig. 1.3.

1.9.1.b Weighted Back Projection

The first reconstructions were performed in Fourier space (De Rosier and Klug, 1968), which requires transforming the information from polar to Cartesian coordinates. This is a difficult undertaking, so most reconstruction methods reconstruct the object in real space. A common reconstruction method is weighted back projection (WBP). In this technique, a 3D reconstruction of the object is obtained by backprojecting the projection images into the object space along their original ray paths (Radermacher, 2007).

However, Fourier space is unevenly sampled, with oversampling near the origin and undersampling at higher frequencies (Gunjan *et al.*, 2017). This uneven sampling results in a blurry reconstruction of the original structure. To prevent low-frequency information from dominating the reconstruction, projection images are weighted with one of several types of filters before backprojection (Gunjan *et al.*, 2017).

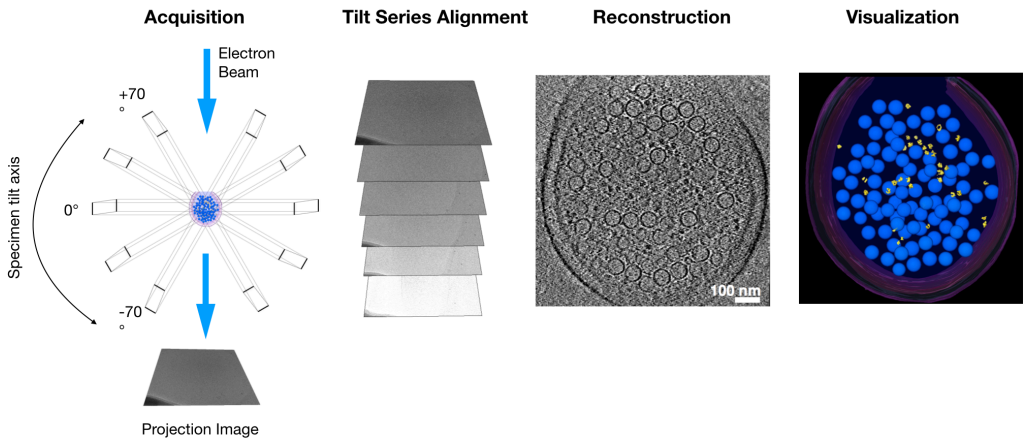

Fig.1.3. Cryo-electron tomography workflow. In the acquisition step, a collection of projection images are taken of an object as it is rotated about the tilt axis in the microscope. These images are collectively called a tilt series. Because of stage backlash, tilt series images may not be perfectly aligned relative to each other, and must be aligned to a common axis of rotation. This is typically done through computational means. An aligned tilt series is reconstructed *in silico* using one of several available algorithms. The resulting 3D density map can then be visualized using homemade or commercialized visualization software.

WPB is both quick and computationally efficient, but is not robust against noise. Another approach is to use iterative algebraic reconstruction techniques (ART) (Gordon *et al.*, 1970). The initial reconstruction is performed by WPB, and iteratively improved into a less blurry, higher-contrast reconstruction.

1.9.1.c Simultaneous Iterative Reconstruction Technique

Most iterative reconstruction techniques present projection images as a system of linear equations that is solved by a matrix inversion (Wolf *et al.*, 2014). Realistically, the size of the datasets and their overdetermination often preclude the possibility of direct matrix inversion (Natterer, 2001). Pseudo-inversion can be achieved through

iterative methods aimed at Euclidian norm minimization (Wolf *et al.*, 2014). An example of such an approach is the simultaneous iterative reconstruction technique (SIRT) (Gilbert, 1972). SIRT begins with a system of linear equations:

$$\boldsymbol{Ax = b} \quad (1.6)$$

$\mathbf{A = (A_{ij})}$ is an M x N projection matrix. Each row of **A** contains the coefficients describing individual ray paths. $\mathbf{A}_{ij}$ describes the contribution of the j^{th} detector pixel with the i^{th} ray path. **A** also describes the projection direction, with **A** representing the forward direction, and $\mathbf{A}^T$ representing the back projection**.** The values of the pixels in the reconstruction are contained in vector **x**, and **b** is the data from the projection images.

This system is solved by a least squares approach that minimizes $||\mathbf{Ax-b}||^2$. This occurs iteratively in the following process:

1. An initial reconstruction is generated by WPB: $\mathbf{x}^{(0)}$

   The following steps are for each SIRT iteration:

2. The reconstruction is forward projected and reconstructed as $\mathbf{Ax}^{(k)}$, where k is the iteration number
3. The result of the forward projection is subtracted from the values of the original projections: $\mathbf{b- Ax}^{(k)}$
4. This sum is then back projected into the reconstruction space: $\mathbf{A}^T\mathbf{(b-Ax}^{(k)})$. However, this term is not correct, because it does not account for the number

of pixels along a given ray path, or the number of ray paths seen by a particular pixel. In other words, this term has to be weighted to reflect that a single ray path contains multiple pixels, and a single pixel has been seen by multiple ray paths. These weighting factors are given by positive diagonal matrices **V** and **W**

5. The weighted term becomes: $\mathbf{VWA^T(b-Ax^{(k)})}$. In SIRT, this is called the correction factor, and it represents the difference in pixel values between reconstructions $\mathbf{x}^{(k)}$ and $\mathbf{x}^{(k+1)}$
6. The correction factor is added to the current reconstruction: $\mathbf{x}^{(k+1)} = \mathbf{x}^{(k)} + \mathbf{VWA^T(b-Ax^{(k)})}$. This equation is called the update equation and reflects the changes made to the values of the pixels in the reconstruction vector during a particular iteration

The procedure ends when a user-defined number of iterations have been completed. Ideally, one would iterate until the system converges, or approaches the iteration where the correction factor is negligible, and $\mathbf{x}^{(n+1)} \approx \mathbf{x}^{(n)}$. Because determining convergence is challenging, choosing the appropriate stopping criteria—such as the number of iterations—is not always easy. My experience is that 8-20 iterations are usually sufficient to reconstruct cryo-tomograms. A greater number of iterations may not only be a waste of computation time, but it might ultimately reintroduce noise into the reconstruction (Tang and Xie, 2018).

SIRT is more time-intensive than WBP, it is more resistant to noise because it iteratively reduces the difference between the original data and the reconstruction, which produces higher SNR tomograms. Regardless of the reconstruction technique, the outcome is a 3D density map of the object of interest. This map is generated into a 3D model using specialized visualization software, such as FEI Avizo, FEI Amira, or tomviz.

1.9.1.d Limitations to Cryo-ET

Cryo-ET's greatest limitation is its maximum resolution, especially when compared to other 3D imaging techniques, such as SPA and sub-tomogram averaging. The maximum attainable resolution *r* of the reconstruction is a function of the object diameter *D,* and the number of projections *n*. This estimation is called the Crowther criterion (Crowther *et al.*, 1970), and is given by:

$$r = \frac{\pi D}{n} \qquad (1.7)$$

Theoretically, improving the number of projections should increase the resolution of the resulting tomogram. However, the resolution of cryo-electron tomograms is hampered by fundamental factors. First, the number of projection slices is limited by the critical dose of biological specimen. Additionally, the cell is a single, asymmetric structure that cannot be averaged with other cells to improve resolution. Instrumental limitations also affect the resolution of cryo-electron tomograms. The effective

thickness of specimen at high tilt angles is $1/\cos(\theta)$, where θ is the tilt angle (Diebolder *et al.*, 2012). Recall that samples > 350 nm are increasingly difficult to image in cryo-TEM. This means that little information comes from images collected at higher tilt angles, which compromises resolution. As in cryo-EM, sample sensitivity limits the maximum tolerable dose, but the critical dose must be partitioned between each projection image in the tilt series, making the dose per projection slice ~1-4 $e^-/Å^2/s$. Furthermore, most microscopes are physically limited to a tilt range of ± 75°, and the specimen cannot be sampled in all of Fourier space. The missing information, colloquially called the "missing wedge," makes the reconstruction appear elongated in the direction of the electron beam (Arslan *et al.*, 2006). The missing wedge can be reduced into a "missing pyramid" by performing dual-axis tomography (Penczek *et al.*, 1995), where data is collected along two tilt axes instead of just one. Both acquisition schemes will result in missing information.

Although the resolution of cryo-electron tomograms is limited to a few nanometers, this is sufficient to visualize macromolecular complexes within a cell. Cells often contain numerous, rather symmetric molecules such as ribosomes, which can be averaged and reconstructed in a technique called subtomogram averaging (Wan and Briggs, 2016). Using this technique, subvolumes of macromolecules obtained from reconstructed tomograms are extracted, aligned, and averaged to generate a single, high-resolution model of the macromolecule. Because the reconstruction is an average of several subtomograms, both the noise and resolution are better than those found in the original tomogram.

1.10 Imaging and Averaging Symmetric Particles

If imaging symmetric macromolecules, yet another strategy is to image hundreds of thousands of identical, randomly-oriented copies of the macromolecule and computationally average them together to reduce noise, enhance contrast, and improve resolution. This approach is the principle behind single particle analysis, (van Heel *et al.*, 2000; Cheng and Walz, 2009; Elmlund and Elmlund, 2015; Vinothkumar and Henderson, 2016) and it will inevitably play a major role in the future of cryo-EM. While this technique is not useful for imaging whole cells or *in situ* imaging of subcellular components, SPA has been used to produce high-contrast images of isolated macromolecules with sub-nanometer resolution, significantly improving our understanding of the structure and function of cellular machinery.

1.11 Next-Generation Techniques for Cryo-Electron Microscopy

The limitations of cryo-ET are unfortunate considering the "resolution revolution" that has been made possible by significant advances in instrumentation and computation in the last decade. Microscopes have more stable stages, higher acceleration voltages, automated data collection, and superior detectors. These advances have proven invaluable for SPA, which can determine structures with < 3Å resolution, making it comparable to X-ray crystallography (Grant and Grigorieff, 2015; Liu *et al.*, 2017). The number of determined structures deposited into protein databases has increased dramatically within the last decade (Patwardhan *et al.*, 2014), and the technique received global recognition when the 2017 Nobel Prize in Chemistry was jointly awarded to Jacques Dubochet, Richard Henderson, and Joachim Frank for their

pioneering work in SPA. It is likely that SPA will be the predominant cryo-EM technique for at least the next few years. The success of SPA relies not only on current technology, but next-generation instrumentation for cryo-EM. This includes improvements on direct electron detectors and the widespread use of phase plates. Most of this technology exists but is in the early stages of development and testing. Nevertheless, the technology has already proven promising for direct applications in single particle analysis, and is expected to make a significant scientific impact in the near future.

1.11.1 Improving Direct Electron Detectors

Although DEDs are state-of-the-art technology, the now commonly used detector—Gatan K2 Summit—has a maximum DQE of well below 100%. If the location of incident primary electrons can be determined with sub-pixel accuracy, future detectors should reach 100% DQE without a significant drop at Nyquist (McMullan *et al.*, 2016). Such an outcome will require addressing the challenges limiting the DQE of current generations. First, all future detectors will operate in counting mode. Both FEI and DE have produced detectors that operate in counting mode, but performance studies on the devices are still limited. However, the results of one such study on the FEI Falcon III is reported in (Kuijper *et al.*, 2015).

Next-generation detectors will also have higher frame rates to reduce both coincidence loss and excessively long exposure times. The K3, Gatan's newest detector, will have a frame rate of 1500 fps. Future detectors should also have higher DQE (Nyquist) in

super resolution mode, which currently allows for images with more pixels but also more noise. No matter the improvements, the DQE(Nyquist) is unlikely to exceed 90% (McMullan *et al.*, 2016). These improvements will improve the resolution of the single particle reconstruction, perhaps pushing resolution into the 1 Å regime.

1.11.2 Volta Phase Plates

Contrast enhancement in cryo-TEM is usually achieved by defocusing the image. As explained in section 1.6.1 of this thesis, defocusing reduces the maximum resolution of an image.

Alternative phase contrast methods such as phase plates have been explored to enhance the contrast of an image with little or no defocus and no effect on resolution. Phase plates produce contrast by introducing a phase shift between scattered and unscattered waves in the diffraction plane in the microscope (Danev and Baumeister, 2016). Of the different types of phase plates available, the Zernike phase plate (ZPP) has been most useful in cryo-EM (Glaeser, 2013). A ZPP consists of a thin layer (~20 nm) layer of amorphous carbon that creates a $\pi/2$ phase shift between scattered and unscattered electrons, the so-called Zernike phase (Danev and Nagayama, 2001). The ZPP also contains a small (~ 1 μm) hole in the center for the beam of unscattered electrons.

ZPPs are limited by their short life spans (~ 1 week), and the necessity to precisely align the hole with the central diffraction beam. Additionally, the size of the hole is a

trade-off between enhanced contrast and the relative difficulty of aligning the beam. Finally, the CTF at the hole edge produces fringes around image features (Danev *et al.*, 2014). These limitations make using ZPPs rather cumbersome.

A suitable alternative is the Volta phase plate (VPP), which consists of a thin film (~ 10 μm) of amorphous carbon heated to around 200 °C. Heated amorphous carbon induces a Volta potential in the area exposed to the electron beam. While beam irradiation causes degradation in ZPPs, it creates a phase shift in VPP (Danev and Baumeister, 2016). This result has several consequences. The first is that there is no need for a hole in a VPP, so precise centering of the electron beam is unnecessary. Secondly, the fringes associated with CTF onset at the hole edges disappear. VPPs are not damaged by an electron beam and have virtually infinite shelf lives. Finally, a phase shift can be generated "on-the-fly, which is critical for automated data collection. The Volta phase plate can enhance the contrast of a specimen at little or no defocus, preserving the maximum attainable resolution.

Despite its merits, the VPP has its disadvantages. The first is that in-focus imaging requires very accurate focusing (Danev *et al.*, 2017; Chua *et al.*, 2017). Another consideration is that phase plates require positioning, conditioning and stigmation at every plate position that is used. These limitations are both tedious and can slow down data acquisition. Nevertheless, two years after its commercialization, the VPP has been used to determine the structures of the *Thermoplasma acidophilum* 20S proteasome and human hemoglobin with 3.2 Å resolution (Danev and Baumeister,

2016; Khoshouei *et al.*, 2017). Studies seeking to improve the resolution of reconstructed particles are already underway (Danev *et al.*, 2017).

1.11.3 Molecular Sociology

Despite the success of the technique, there are limitations to SPA that may make other techniques more appealing. First, SPA requires a high concentration of purified sample, and the isolation and purification procedure is nontrivial. Isolating molecules may induce additional conformations or create nonphysiological ones. Individual proteins or molecular assemblies cannot be contextualized once removed from the cell. It is rare that individual cellular components operate as isolated units within the cell, but this realization is lost when examining isolated particles. High-resolution reconstructions of individual proteins or protein complexes have their purpose, but they tell us little about the interplay between cellular components in their native environment, called the "molecular sociology" of the cell (Robinson *et al.*, 2007).

Molecular sociology does not require new techniques, but a new approach to understanding the cell. This approach is called a "post-reductionist" approach, and it aims to understand how cellular assemblies act in concert to perform specific functions (Beck and Baumeister, 2016). The work presented in (Mahamid *et al.*, 2016) demonstrates how cryo-FIB and cryo-ET can be used to understand the organization of the nuclear periphery of the HeLa cell. Similar experiments on other cells of scientific interest are sure to follow, and will likely mark a shift from SPA back to techniques such as cryo-ET and subtomogram averaging. If combined with advanced

instrumentation, molecular sociology could help understand the structure and function of macromolecular assemblies in their native context with atomic detail (Beck and Baumeister, 2016).

1.12 Concluding Remarks

Cryo-ET is a versatile technique that can bridge the gap between cell and molecular biology. With the ability to resolved structures on a large range of length scales, cryo-ET has been used to resolve a cell's membrane components, such as the nuclear pore complex, organelles such as chloroplasts and Golgi apparatuses, and protein complexes, such as ribosomes (Maimon *et al.*, 2012; Han *et al.*, 2013; Engel *et al.*, 2015; Pfeffer *et al.*, 2015). Cryo-ET allows interrogation into a cell's complex molecular machinery, which can then be paired with molecular data to provide a more complete understanding of cellular function.

1.13 Dissertation Layout

This dissertation contains three reports of three very different types of cells. The first report (Chapter 2) describes how cryo-EM was used to characterize post-insemination phenomenological changes in Zika-transmitting mosquito *Aedes aegypti.* The second report (Chapter 3) uses cryo-EM to investigate the formation of exosomes and microvesicles in metastatic breast cancer cells. The third report addresses how cryo-FIB and cryo-ET were used to gain access to and characterize the photosynthetic apparatuses of purple bacteria *Rhodobacter sphaeroides*. The first two reports are united by the use of cryo-EM to probe the macromolecular aspects of disease. The

third report focuses on a cell that is not related to disease, but enlists more challenging microscopy techniques which are better performed on a prokaryotic cell before moving on to complex, eukaryotic cells typical of disease. In Chapter 5, I present concluding remarks to this thesis, as well as potential directions for each project presented herein.

REFERENCES

1. Al-Amoudi, A., Studer, D., and Dubochet, J. (2005) Cutting artefacts and cutting process in vitreous sections for cryo-electron microscopy. *J Struct Biol* **150**: 109–121.

2. Arnold, J., Mahamid, J., Lučić, V., de Marco, A., Fernandez, J.-J., Laugks, T., *et al.* (2016) Site-specific sryo-focused ion beam sample preparation guided by 3D correlative microscopy. *Biophys J* **110**: 860–869.

3. Arslan, I., Tong, J.R., and Midgley, P.A. (2006) Reducing the missing wedge: high-resolution dual axis tomography of inorganic materials. *Ultramicroscopy* **106**: 994–1000.

4. Bainton, D.F., Ullyot, J.L., and Farquhar, M.G. (1971) The development of neutrophilic polymorphonuclear leukocytes in human bone marrow. *J Exp Med* **134**: 907–34.

5. Baumeister, W., Grimm, R., and Walz, J. (1999) Electron tomography of molecules and cells. *Trends Cell Biol* **9**: 81-85.

6. Beck, M., and Baumeister, W. (2016) Cryo-electron tomography: can it reveal the molecular sociology of cells in atomic detail? *Trends Cell Biol* **26**: 825–837.

7. Broglie, L. de (1925) Recherches sur la théorie des Quanta. *Ann Phys (Paris)* **10**: 22–128.

8. Broglie, L. de (1923) Waves and Quanta. *Nature* **112**: 540–540.

9. Brüggeller, P., and Mayer, E. (1980) Complete vitrification in pure liquid water and dilute aqueous solutions. *Nature* **288**: 569–571.

10. Carlson, D.B., and Evans, J.E. (2012) Low dose imaging techniques for imaging transmission electron microscopy. In: M. Khan (Ed.), *The Transmission Electron Microscope* (pp. 85-98). Croatia: InTech.

11. Chen, T., Catrysse, P.B., Gamal, A. El, and Wandell, B.A. (2000) How small should pixel size be? *Proc SPIE* **3965**: 451-459.

12. Cheng, Y., Grigorieff, N., Penczek, P.A., and Walz, T. (2015) A primer to single-particle cryo-electron microscopy. *Cell* **161**: 438–449.

13. Cheng, Y., and Walz, T. (2009) The advent of near-atomic resolution in single-particle electron microscopy. *Annu Rev Biochem* **78**: 723–742.

14. Chua, E.Y.D., and Sandin, S. (2017) Advances in phase plate cryo-EM imaging of DNA and nucleosomes. *Nucleus* **8**: 275-578.

15. Clough, R.N., Moldovan, G., and Kirkland, A.I. (2014) Direct detectors for electron microscopy. *J Phys Conf Ser* **522**: 012046.

16. Crowther, R.A., DeRosier, D.J., and Klug, A. (1970) The reconstruction of a three-dimensional structure from projections and its application to electron microscopy. *Proc R Soc A Math Phys Eng Sci* **317**: 319–340.

17. Danev, R., and Baumeister, W. (2016) Cryo-EM single particle analysis with the Volta phase plate. *Elife* **5**: e13046.

18. Danev, R., Buijsse, B., Khoshouei, M., Plitzko, J.M., Baumeister, W., Plitzko, J.M., *et al.* (2014) Volta potential phase plate for in-focus phase contrast transmission electron microscopy. *Proc Natl Acad Sci* **111**: 15635–15640.

19. Danev, R., and Nagayama, K. (2001) Transmission electron microscopy with Zernike phase plate. *Ultramicroscopy* **88**: 243–52.

20. Danev, R., Tegunov, D., and Baumeister, W. (2017) Using the Volta phase plate with defocus for cryo-EM single particle analysis. *Elife* **6**: e23006.

21. DeRosier, D.J., and Klug, A. (1968) Reconstruction of three dimensional structures from electron micrographs. *Nature* **217**: 130–134.

22. Diebolder, C.A., Koster, A.J., and Koning, R.I. (2012) Pushing the resolution limits in cryo electron tomography of biological structures. *J Microsc* **248**: 1–5.

23. Dierksen, K., Typke, D., Hegerl, R., Koster, A.J., and Baumeister, W. (1992) Towards automatic electron tomography. *Ultramicroscopy* **40**: 71–87.

24. Dubochet, J., and McDowall, A.W. (1981) Vitrificaiton of pure water for electron microscopy. *J Microsc* **124**: 3–4.

25. Elmlund, D., and Elmlund, H. (2015) Cryogenic electron microscopy and single-particle analysis. *Annu Rev Biochem* **84**: 499–517.

26. Engel, B.D., Schaffer, M., Kuhn Cuellar, L., Villa, E., Plitzko, J.M., and Baumeister, W. (2015) Native architecture of the Chlamydomonas chloroplast revealed by in situ cryo-electron tomography. *Elife* **4**: e04889.

27. Faruqi, A.R., and McMullan, G. (2011) Electronic detectors for electron

microscopy. *Q Rev Biophys* **44**: 357-390.

28. Fernández-Morán, H. (1960) Low-temperature preparation techniques for electorn microscopy of biological specimens based on rapid freezing with liquid helium II. *Ann N Y Acad Sci* **85**: 689–713.

29. Frank, J. (2006) *Three-Dimensional Electron Microscopy of Macromolecular Assemblies : Visualization of Biological Molecules in their Native State*. UK: Oxford University Press.

30. Gest, H. (2004) The discovery of microorganisms by Robert Hooke and Antoni Van Leeuwenhoek, fellows of the Royal Society. *Notes Rec R Soc Lond* **58**: 187–201.

31. Gilbert, P. (1972) Iterative methods for the three-dimensional reconstruction of an object from projections. *J Theor Biol* **36**: 105–117.

32. Glaeser, R.M. (2008) Retrospective: radiation damage and its associated "information limitations." *J Struct Biol* **163**: 271–276.

33. Glaeser, R.M. (2013) Invited review article: methods for imaging weak-phase objects in electron microscopy. *Rev Sci Instrum* **84**: 111101.

34. Gordon, R., Bender, R., and Herman, G.T. (1970) Algebraic reconstruction techniques (ART) for three-dimensional electron microscopy and X-ray photography. *J Theor Biol* **29**: 471–481.

35. Grant, T., and Grigorieff, N. (2015) Measuring the optimal exposure for single particle cryo-EM using a 2.6 Å reconstruction of rotavirus VP6. *Elife* **4**: e06980.

36. Grigorieff, N., and Harrison, S.C. (2011) Near-atomic resolution reconstructions of icosahedral viruses from electron cryo-microscopy. *Curr Opin Struct Biol* **21**: 265–273.

37. Grimm, R., Typke, D., Bärmann, M., and Baumeister, W. (1996) Determination of the inelastic mean free path in ice by examination of tilted vesicles and automated most probable loss imaging. *Ultramicroscopy* **63**: 169–179.

38. Grimm, Typke, and Baumeister (1998) Improving image quality by zero-loss energy filtering: quantitative assessment by means of image cross-correlation. *J Microsc* **190**: 339–349.

39. Gunjan V.K., Shaik F., Venkatesh C., and Amarnath M. (2017) Visual Quality

Improvement of CT Image Reconstruction with Quantitative Measures. In: *Computational Methods in Molecular Imaging Technologies* (pp.45-73). Singapore: Springer.

40. Han, H.-M., Bouchet-Marquis, C., Huebinger, J., Grabenbauer, M., (2013) Golgi apparatus analyzed by cryo-electron microscopy. *Histochem Cell Biol* **140**: 369-381.

41. Han, H.-M., Zuber, B., and Dubochet, J. (2008) Compression and crevasses in vitreous sections under different cutting conditions. *J Microsc* **230**: 167–171.

42. Hayat, M.A. (1986) Glutaraldehyde: Role in electron microscopy. *Micron Microsc Acta* **17**: 115–135.

43. Hayles, M.F., Stokes, D.J., Phifer, D., and Findlay, K.C. (2007) A technique for improved focused ion beam milling of cryo-prepared life science specimens. *J Microsc* **226**: 263–269.

44. Heel, M. van, Gowen, B., Matadeen, R., Orlova, E. V, Finn, R., Pape, T., *et al.* (2000) Single-particle electron cryo-microscopy: towards atomic resolution. *Q Rev Biophys* **33**: 307–69.

45. Henderson, R. (1990) Cryo-protection of protein crystals against radiation damage in electron and X-ray diffraction. *Proc R Soc B Biol Sci* **241**: 6–8.

46. International Study Group. Cryoprotection in electron microscopy (1986) *J Microsc* **141**: 385–391.

47. Karimzadeh, A. (2014) Modulation transfer function of a triangular pixel array detector. *J Opt Soc Am A Opt Image Sci Vis* **31**: 1688–91.

48. Karnovsky, M.J. (1965) A formaldehyde-glutaraldehyde fixative of high osmolality for sse in electron microscopy. *J Cell Biol* **27**: 1A-149A.

49. Khoshouei, M., Radjainia, M., Baumeister, W., and Danev, R. (2017) Cryo-EM structure of haemoglobin at 3.2 Å determined with the Volta phase plate. *Nat Commun* **8**: 16099.

50. Kourkoutis, L.F., Plitzko, J.M., and Baumeister, W. (2012) Electron microscopy of biological materials at the nanometer scale. *Annu Rev Mater Res* **42**: 33–58.

51. Krivanek, O.L., and Mooney, P.E. (1993) Applications of slow-scan CCD cameras in transmission electron microscopy. *Ultramicroscopy* **49**: 95–108.

52. Kuijper, M., Hoften, G. van, Janssen, B., Geurink, R., Carlo, S. De, Vos, M., *et al.* (2015) FEI's direct electron detector developments: embarking on a revolution in cryo-TEM. *J Struct Biol* **192**: 179–187.

53. Liu, Z., Gutierrez-Vargas, C., Wei, J., Grassucci, R.A., Sun, M., Espina, N., *et al.* (2017) Determination of the ribosome structure to a resolution of 2.5 Å by single-particle cryo-EM. *Protein Sci* **26**: 82-92.

54. Lučić, V., Förster, F., and Baumeister, W. (2005) Structural Studies by Electron Tomography: From Cells to Molecules. *Annu Rev Biochem* **74**: 833–865.

55. Mahamid, J., Pfeffer, S., Schaffer, M., Villa, E., Danev, R., Kuhn Cuellar, L., *et al.* (2016) Visualizing the molecular sociology at the HeLa cell nuclear periphery. *Science* **351**: 969–972.

56. Mahamid, J., Schampers, R., Persoon, H., Hyman, A.A., Baumeister, W., and Plitzko, J.M. (2015) A focused ion beam milling and lift-out approach for site-specific preparation of frozen-hydrated lamellas from multicellular organisms. *J Struct Biol* **192**: 262–269.

57. Maimon, T., Elad, N., Dahan, I., and Medalia, O. (2012). The human nuclear pore complex as revealed by cryo-electron tomography. *Structure* **20**: 998–1006.

58. Marko, M., Hsieh, C., Moberly-Chan, W. Mannella, C.A., and Frank, J. (2006) Focused ion beam milling of vitreous water: prospects for an alternative to cryo-ultramicrotomy of frozen-hydrated biological samples. *J Microsc* **222**: 42–47.

59. Marko, M., Hsieh, C., Schalek, R., Frank, J., and Mannella, C. (2007) Focused-ion-beam thinning of frozen-hydrated biological specimens for cryo-electron microscopy. *Nat Methods* **4**: 215–217.

60. Mazzarello, P. (1999) A unifying concept: the history of cell theory. *Nat Cell Biol* **1**: E13–E15.

61. McDonald, K.L., and Auer, M. (2006) High-pressure freezing, cellular tomography, and structural cell biology. *Biotechniques* **41**: 137, 139, 141.

62. McMullan, G., Chen, S., Henderson, R., and Faruqi, A.R. (2009) Detective quantum efficiency of electron area detectors in electron microscopy. *Ultramicroscopy* **109**: 1126–1143.

63. McMullan, G., Faruqi, A.R., Clare, D., and Henderson, R. (2014) Comparison

of optimal performance at 300keV of three direct electron detectors for use in low dose electron microscopy. *Ultramicroscopy* **147**: 156–163.

64. McMullan, G., Faruqi, A.R., and Henderson, R. (2016) Direct electron detectors. *Methods Enzymol* **579**: 1–17.

65. McMullan, G., Faruqi, A.R., Henderson, R., Guerrini, N., Turchetta, R., Jacobs, A., and Hoften, G. van (2009) Experimental observation of the improvement in MTF from backthinning a CMOS direct electron detector. *Ultramicroscopy* **109**: 1144–1147.

66. Moor, H. (1987) Theory and Practice of High Pressure Freezing. In *Cryotechniques in Biological Electron Microscopy* (pp.175-191). In: R.A. Steinbrecht & K. Zierold (Eds.) Berlin, Heidelbery: Springer Berlin Heidelberg.

67. Moulders H (2003) The use of a SEM/FIB dual beam applied to biological samples. *G.I.T. Imag Microsc* **2**: 8–10.

68. Nagayama, K., and Danev, R. (2008) Phase contrast electron microscopy: development of thin-film phase plates and biological applications. *Philos Trans R Soc Lond B Biol Sci* **363**: 2153–62.

69. Natterer, F. (1986), *The Mathematics of Computerized Tomography*. USA: Wiley.

70. Noble, J.M., Lubieniecki, J., Plitzko, J., Engelhardt, H., Baumeister, W., and Kourkoutis, L.F. (2017) Cryo-FIB milling reveals complex vesicular architecture in photosynthetic bacteria. *Microsc Microanal* **23**: 1250–1251.

71. Overwijk, M.H.F., Heuvel, F.C. van den, and Bulle-Lieuwma, C.W.T. (1993) Novel scheme for the preparation of transmission electron microscopy specimens with a focused ion beam. *J Vac Sci Technol B Microelectron Nanom Struct* **11**: 2021-2024.

72. Parmenter, C.D.J., Fay, M.W., Hartfield, C., and Eltaher, H. (2016) Making the partically impossible "merely difficult"—cryogenic FIB lift-out for "damage free" soft matter imaging. *Microsc Res Tech* **79**: 298-303.

73. Patwardhan, A., Ashton, A., Brandt, R., Butcher, S., Carzaniga, R., Chiu, W., *et al.* (2014) A 3D cellular context for the macromolecular world. *Nat Struct Mol Biol* **21**: 841–845.

74. Penczek, P., Marko, M., Buttle, K., and Frank, J. (1995) Double-tilt electron tomography. *Ultramicroscopy* **60**: 393–410.

75. Pfeffer, S., Woellhaf, M.W., Herrmann, J.M., Förster, F., 2015. Organization of the mitochondrial translation machinery studied in situ by cryoelectron tomography. *Nat Commun* **6**:6019.

76. Pierson, J., Vos, M., McIntosh, J.R., and Peters, P.J. (2011) Perspectives on electron cryo-tomography of vitreous cryo-sections. *J Electron Microscopy (Tokyo)* **60**: S93–S100.

77. Radermacher, M. (2006) Weighted back-projection methods. In: J. Frank (Ed.), *Electron Tomography* (pp. 245-274). USA: Springer New York.

78. Rigort, A., Bäuerlein, F.J.B., Leis, A., Gruska, M., Hoffmann, C., Laugks, T., *et al.* (2010) Micromachining tools and correlative approaches for cellular cryo-electron tomography. *J Struct Biol* **172**: 169–179.

79. Rigort, A., Bäuerlein, F.J.B., Villa, E., Eibauer, M., Laugks, T., Baumeister, W., and Plitzko, J.M. (2012) Focused ion beam micromachining of eukaryotic cells for cryoelectron tomography. *Proc Natl Acad Sci U S A* **109**: 4449–54.

80. Rigort, A., and Plitzko, J.M. (2015) Cryo-focused-ion-beam applications in structural biology. *Arch Biochem Biophys* **581**: 122–130.

81. Roberts, P.T.E., Chapman, J.N., and MacLeod, A.M. (1982) A CCD-based image recording system for the CTEM. *Ultramicroscopy* **8**: 385–396.

82. Robinson, C. V., Sali, A., and Baumeister, W. (2007) The molecular sociology of the cell. *Nature* **450**: 973–982.

83. Ruska, E. (1987) The development of the electron microscope and of electron microscopy. *Rev Mod Phys* **59**: 627–638.

84. Sartori, N., Richter, K., and Dubochet, J. (1993) Vitrification depth can be increased more than 10-fold by high-pressure freezing. *J Microsc* **172**: 55–61.

85. Schwartz, C.L., Sarbash, V.I., Ataullakhanov, F.I., McIntosh, J.R., and Nicastro, D. (2007) Cryo-fluorescence microscopy facilitates correlations between light and cryo-electron microscopy and reduces the rate of photobleaching. *J Microsc* **227**: 98–109.

86. Sydor, A.M., Czymmek, K.J., Puchner, E.M., and Mennela, V. (2015) Super-resolution microscopy: from single molecules to supramolecular assemblies. *Trends Cell Biol* **25**: 730-748.

87. Severs, N.J. (2007) Freeze-fracture electron microscopy. *Nat Protoc* **2**: 547–

576.

88. Sleytr, U.B., and Robards, A.W. (1982) Understanding the artefact problem in freeze-fracture replication: a review. *J Microsc* **126**: 101–122.

89. Carlson, D.B., and Evans, J.E. (2012) Low dose imaging techniques for imaging transmission electron microscopy. In: M. Khan (Ed.), *The Transmission Electron Microscope* (pp. 85-98). Croatia: InTech.

90. Tang, X. and Xie, H. (2018). X-ray computed tomography for diagnostic imaging—from single-slice to multi-slice. In: P. Russo (Ed.), *Handbook of X-ray Imaging: Physics and Terminology* (pp. 637-663). USA: CRC Press.

91. Taylor, K.A., and Glaeser, R.M. (1974) Electron diffraction of frozen, hydrated protein crystals. *Science* **186**: 1036–7.

92. Thompson, R.F., Walker, M., Siebert, C.A., Muench, S.P., and Ranson, N.A. (2016) An introduction to sample preparation and imaging by cryo-electron microscopy for structural biology. *Methods* **100**: 3–15.

93. Toyoshima, C., and Unwin, N. (1988) Contrast transfer for frozen-hydrated specimens: Determination from pairs of defocused images. *Ultramicroscopy* **25**: 279–291.

94. Villa, E., Schaffer, M., Plitzko, J.M., and Baumeister, W. (2013) Opening windows into the cell: focused-ion-beam milling for cryo-electron tomography. *Curr Opin Struct Biol* **23**: 771–777.

95. Vinothkumar, K.R., and Henderson, R. (2016) Single particle electron cryomicroscopy: trends, issues and future perspective. *Q Rev Biophys* **49**: e13.

96. Viotti, C. (2014) ER and vacuoles: never been closer. *Front Plant Sci* **5**: 20.

97. Wan, W., and Briggs, J.A.G. (2016) Cryo-electron tomography and subtomogram averaging. *Methods Enzymol* **579**: 329–367.

98. Williams, D.B., and Carter, C.B. (2009) The Transmission Electron Microscope. In: D.B. Willams & C.B. Carter (Eds.), *Transmission Electron Microscopy* (pp. 3-22). USA: Springer US.

99. Wolf, D., Lubk, A., and Lichte, H. (2014) Weighted simultaneous iterative reconstruction technique for single-axis tomography. *Ultramicroscopy* **136**: 15–25.

100. Wu, S., Armache, J.-P., and Cheng, Y. (2016) Single-particle cryo-EM

data acquisition by using direct electron detection camera. *Miroscopy (Oxf)* **65**: 35–41.

101. Zachman, M., Asenath-Smith, E., Estroff, L.A., and Kourkoutis, L.F. (2016). Site-specific preapration of intact solid-liquid interfaces by label-free in situ localizatin and cryo-focused ion beam lift-out. *Micro Microanal* **22**: 1338-1349.

102. Zhang, X., Jin, L., Fang, Q., Hui, W.H., and Zhou, Z.H. (2010) 3.3 Å cryo-EM structure of a nonenveloped virus reveals a priming mechanism for cell entry. *Cell* **141**: 472–482.

103. Ziegler, J.F. (1988) The stopping and range of ions in solids. In: J.F. Ziegler (Ed.) *Ion Implantation Science and Technology, Second Edition* (pp. 3-61). USA: Academic Press.

CHAPTER 2

ULTRASTRUCTURAL CHANGES TO STORED *AEDES AEGYPTI* SPERMATOZOA COINCIDE WITH INCREASED MOTILITY AND FECUNDITY

2.1 Summary

Sperm storage extends the time for fertilization in *Aedes aegypti* mosquitoes from a few hours to several weeks. The corresponding physiological changes to stored sperm however, are largely unknown. In this study, spermatozoa from the male seminal vesicle, the female bursa, and the female spermathecae of *Ae. aegypti* were investigated to identify transformations in sperm ultrastructure and motility as a function of time post-insemination. Spermatozoa harvested from the bursa, the female's organ, were ultrastructurally indistinguishable from sperm obtained from the male seminal vesicle. However, sperm removed from the spermathecae, the female's long-term storage organ, showed morphological changes marked by the removal of the sperm coat and outer membrane. Sperm stored in the spermathecae are quiescent for up to four hours post-storage, after which point motility is gradually restored. Changes in spermatozoa ultrastructure and morphology closely coincide with the onset of fecundity in female *Ae. aegpyti* mosquitoes and may be requisite modifications for successful oviposition or sperm maintenance.

2.2 Introduction

The mosquito *Aedes aegypti* is the primary transmitter of dengue, yellow fever, chikungunya, and Zika viruses. As such, it is responsible for significant morbidity, mortality, and strain on public health infrastructure throughout its global range[1,2]. One life history characteristic that has allowed *Ae. aegypti* to invade and persist in urban areas across the globe is its efficient reproduction. Females are able to lay hundreds of eggs throughout their lifetime, fertilizing each using a cache of sperm from a single mating[3,4]. Because storing and maintaining sperm is critical to mosquito reproduction, processes related to sperm maintenance and nourishment may reveal important targets that can be manipulated to control mosquito populations. However, little is known about how these gametes are nurtured in the female and prepared for fertilization[5].

Post-copulatory, pre-zygotic sperm processing has been best described in mammals, particularly humans and livestock[6–8]. In both cases, sperm are typically stored within the female's reproductive tract only long enough to fertilize an egg, and they usually do not survive more than a few days after copulation[9]. During this time, mammalian sperm undergo a series of molecular and locomotive changes. For example, cholesterol is removed from the sperm plasma membrane, membrane fluidity is adjusted to prepare sperm for exocytosis needed for fertilization, and asymmetric beating of the flagellum results in hypermotility[7,8]. These modifications prepare the sperm for its ultimate objective of fertilizing an egg. Collectively, the modifications required to prepare a mammalian sperm for fertilization are called "capacitation"[10,11].

In arthropods, accounts of capacitation-like processes are limited. *Mytilocypris mytiloides*, a crustacean with gigantic sperm, represents one of the most comprehensive descriptions of sperm modification paired with a likely reproductive

function[12]. In this organism, sperm are initially enveloped in two extracellular coats but shed the outermost coat once stored within the female. Outer coat removal coincides with the onset of sperm motility and oviposition, suggesting that the latter two processes cannot proceed until the outer coat is removed. Similarly, eupyrene sperm (nucleated sperm that take part in fertilization) of the silkworm moth *Bombyx mori* shed an outer sheath while in the female reproductive tract. By contrast, apyrene sperm (sperm without nuclei that do not partake in fertilization) do not shed this covering, suggesting that its removal is only necessary in the fertilizing sperm[13]. Sperm modification also occurs in other insect taxa, such as *Musca*, Lepidoptera, and Orthoptera, among others[14,15].

To date, no such investigations of sperm modification have been conducted on *Ae. aegypti*, despite its medical importance. Two reports in other mosquitoes (*Toxorhynchites brevipalpis* and *Culex quinquefasciatus*) demonstrate the removal of an outer sperm coat in the female[16,17]. However, both reports lack descriptions of the timing of this event, the frequency with which it occurs, and supporting evidence to suggest the potential function(s) of removal of the sperm coat. Using cryo-electron microscopy, we describe the morphology of *Ae. aegypti* spermatozoa stored at various locations in the male and female reproductive tracts, with emphasis on sperm coat removal. By complementing these ultrastructural observations with motility and fertility assays, we describe sperm processing events that take place prior to fertilization. Ultimately, understanding the timing and mechanisms of post-copulatory changes to *Ae. aegypti* spermatozoa may lead to novel methods of population control.

2.3 Results

2.3.1 Ultrastructural characteristics of the spermatozoa in the seminal vesicle (♂) and bursa (♀)

The spermatozoa of 5-7 day post-eclosion, sexually-mature, virgin male *Ae. aegypti* mosquitoes were examined as a control to any post-copulatory phenomenological changes to the sperm. (Fig. 2.1). Mature spermatozoa were about 250 μm long and consisted of three primary regions: the head, which contains the nucleus, the flagellum, which contains the axoneme that drives sperm motility, and the centriole adjunct that unites the two. The head is about 30 μm long and 250 nm wide at the tip. The width of the head gradually increases to a maximum of ~550 nm at the centriole adjunct. The nucleus contains densely-packed chromatin and appears as a homogenous, electron-dense region throughout the entire length of the sperm head.

Sperm harvested from the male seminal vesicles contained intranuclear vesicles, electron-dense, membranous structures that appear to be contained within the sperm nucleus. Vesicles are ~200 nm in diameter (Fig. 2.2). A single sperm head often contains multiple vesicles. These vesicles are considered an artifact of spermatogenesis in mosquitoes and result from the condensation of chromatin in the nucleus[18]. Spermatogenic vesicle formation has been demonstrated in similar species, but has not been reported in *Aedes aegypti* until now[18].

The flagellum begins at the centriole adjunct and comprises the remaining length of the spermatozoon. The width of the sperm is about 550 nm at the centriole adjunct and

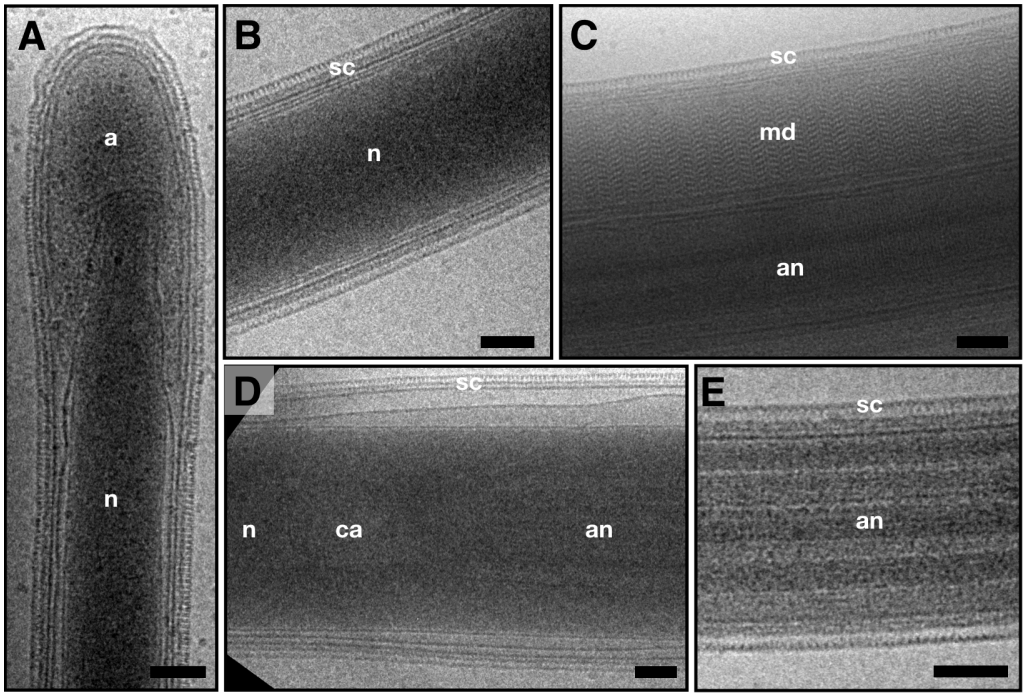

Fig. 2.1. Cryo-TEM images of a spermatozoa harvested from the male seminal vesicle. *Ae. aegypti* spermatozoa consists of a head (A,B), flagellum (C,E), and a centriole adjunct (D). The tip of the head contains an acrosome and a nucleus (A), while the lower part of the head contains just the nucleus (B). The head and flagellum meet at the centriole adjunct (D). The centriole adjunct is where the nucleus from the head ends and the axoneme (responsible for sperm motility) begins. The center part of the tail is comprised of axoneme and two mitochonndrial derivatives (C), while the posterior part of the tail contains only axoneme (E). The entire sperm is surrounded by a sperm coat. *Abbreviations: a = acrosome, n = nucleus, sc = sperm coat, ca = centriole adjunct, an = axoneme, md= mitochondrial derivative. Scale bars: 100 nm*

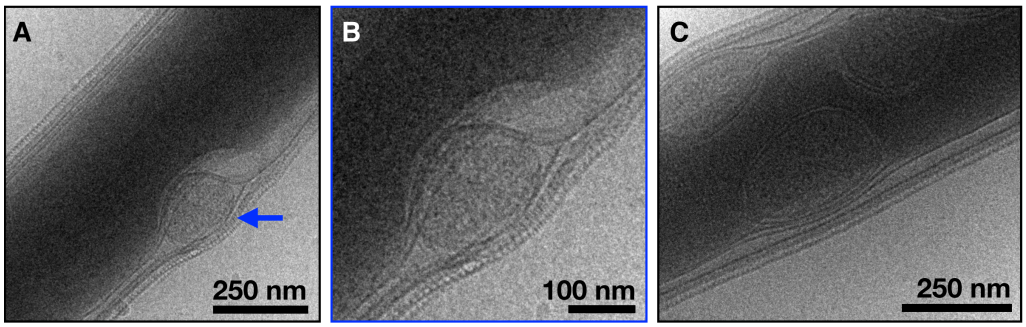

Fig. 2.2. Intranuclear vesicles in *Ae. aegypti*. Intranuclear vesicles are present in the heads of *Ae. aegypti* spermatozoa. Vesicles are electron-dense, membrane-bound structures that are confined within the nucleus by the plasma membrane (A-C). A single head can contain one (A-B) or several (C) of these vesicles.

gradually increases to a maximum thickness of 750 nm midway along the flagellum. The flagellum then tapers to the tip of the tail, which is about 150 nm wide. The sperm tail contains the axoneme, an arrangement of microtubules responsible for sperm motility. *Ae. aegypti* spermatozoa also contain two elongated mitochondrial derivatives (MDs) that originate at the centriole adjunct and perpetuate nearly the entire length of the flagellum. Both MDs contain structurally indentical, membrane-bound, paracrystalline cristae (Appendix A.2). The two MDs are similar in width, about 150 nm, and occupy a large portion of the cytoplasm. In some cases, such as that seen in Fig. 2.3F, the MDs are both clearly visible. In others, such as those seen in Fig. 2.3D, the MDs are not readily visible in projection mode because they overlap either with each other or other structures, such as the axoneme. The entire sperm is bound by a triple-layered membrane that consists of a plasma membrane about 3 nm thick, an outer membrane about 5 nm thick, and a sperm coat about 35 nm thick (Fig. 2.1A-E). At the anterior tip of the sperm head is the acrosome, which is bound by a single-layer

acrosomal membrane situated between the inner and outermost layer of the plasma membrane (Fig. 2.1A).

2.3.2 Post-insemination modifications of the spermatozoa in the bursa and spermathecae (♀)

After insemination, sperm are transferred to a female's bursa, whose sole purpose is to receive the ejaculate. Sperm in this organ become rapidly motile while bathing in seminal fluid. After minutes, sperm ascend narrow ducts to their long-term storage organs, the spermathecae, where they are stored for the rest of a female's life (or until they are used for fertilization). We tested whether morphological changes occur to sperm either in the bursa or in the spermathecae by comparing them to sperm harvested from the seminal vesicles of unmated males. Sperm taken from the bursa were structurally indistinguishable from those removed from the seminal vesicle (Fig 2.3A,E; B,F). Sperm harvested from the spermathecae, however, showed pronounced ultrastructural changes (Fig 2.3C,G). The outer coat and the outer membrane were shed along the entire length of the sperm, leaving the inner membrane behind. Regions of the sloughed sperm coat became caught around the vigorously whiplashing tail, but was removed from the rigid head in once piece (Fig 2.4). The cytoplasm of the sperm does not compress in the absence of the sperm coat. The dimensions of cytoplasmic features, such as the nucleus, MDs, and axoneme, remained unchanged.

Sperm coat removal occurs before 4 hpm, but the earliest time point was difficult to establish due to the difficulty of removing sperm from recently mated females. All

sperm observed from 4 hpm females (n = 14 sperm from 2 females) were either in an active state of sperm coat shedding or the sperm coat had been completely shed. Almost 80% of sperm harvested from 12 hpm females (n= 68 sperm from 3 females) had completely shed their sperm coats. Finally, sperm from 1 day post-mated females (n = 20 sperm from 2 females) had completely shed their sperm coats. A table of the proportion of sperm in active and completed states of sperm coat removal are presented in Appendix A.4.

2.3.4 Sperm motility in the female spermathecae

While harvesting sperm from the spermathecae for ultrastructural studies, it became apparent that sperm that had been stored for only a short time within the spermathecae demonstrated weaker motility than those that had been stored for longer. To better understand this phenomenon, the spermathecae of inseminated females were ruptured at time intervals between 2 and 24 h post-insemination, and their motility was recorded (Fig 2.5). Because individual sperm demonstrated a wide range of flagellar velocity and motility patterns, we recorded the time at which 20 sperm emerged from the ruptured spermathecae as a proxy for the overall motility of the sperm contained within. The spill-out time was defined as the time it took for 20 sperm to emerge from the cracked spermathecae. We found 20 sperm to be sufficient a number, because once more than 20 sperm had emerged from the spermathecae, individual sperm became very difficult to track until they had completely dissociated from the sperm bundle and entered free-swimming mode. Sperm were monitored for a total of 2 minutes, after which time sperm became gradually inactive and died.

Sperm stored in females less than 4 hours post-mated (hpm) exited the cracked spermathecae as part of the sperm mass instead of as individual sperm (Fig 2.5A). Once outside the spermathecae, very few sperm in < 4 hpm females completely dissociated from the sperm mass to enter free-swimming mode; the few sperm that dissociated from the sperm bundle showed compromised motility and sluggish swimming behavior. After minutes of video recording, sperm from < 4 hpm females had not traveled very far from the spermathecae (Fig 2.5A). Most sperm are still trapped within the sperm bundle or inside the spermathecae.

Sperm stored in females 8-24 hpm emerged from the cracked spermathecae and quickly dissociated from the sperm mass to enter free-swimming mode. As sperm dissociated from the bundle, the sperm mass diffused into a "sperm cloud" surrounding the spermathecae. Unlike in earlier hpm females, sperm stored in 8-24 hpm females were very motile and quickly swam away from the spermathecae, often leaving the field-of-view. Spill-out time plateaued at 8 hpm. Additionally, the ability of an individual sperm to dissociate from the sperm bundle and enter free-swimming mode was not noticeably different in females beyond 8 hpm. Sperm harvested from 6 hpm females demonstrate intermediate spill-out characteristics.

2.3.6 Fertilization competence

Given our observed changes to sperm morphology and motility, the question arises whether these changes are associated with a female's ability to fertilize eggs. Thus, we investigated how soon females are able to fertilize eggs after insemination. While

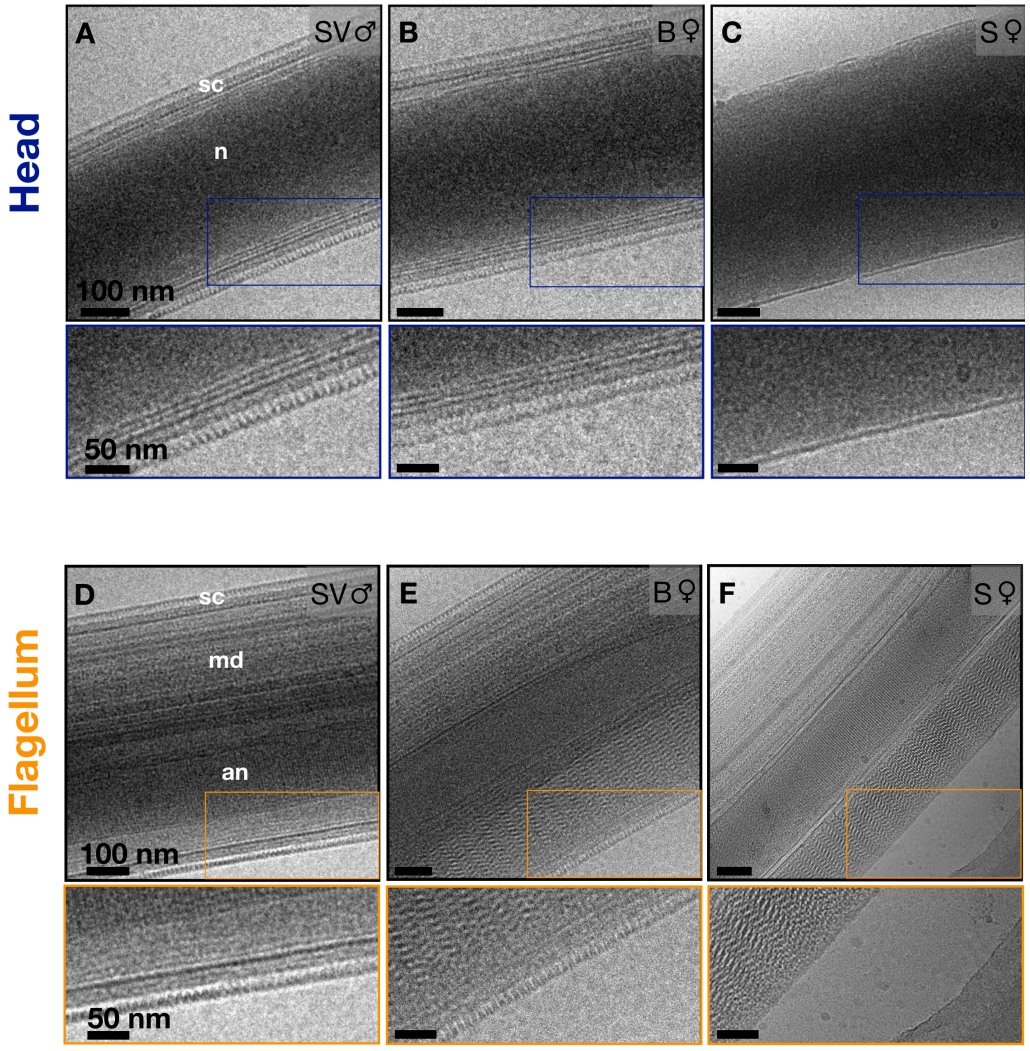

Fig. 2.3. Mature sperm ultrastructure in the male seminal vesicle, female bursa, and female spermathecae. Spermatozoa harvested from the seminal vesicles of sexually-mature, virgin *Ae. aegypti* males were used as a reference to assess morphological changes to sperm stored within the female *Ae. aegypti* mosquitoes. The spermatozoa harvested from the male seminal vesicle and the female bursa were morphologically indistinguishable (A,B; D-E). Spermatozoa harvested from the female spermathecae showed the removal of the sperm coat and the outer membrane. The cytoplasm, as well as its constituents, appear unaltered (A,C; D,G).

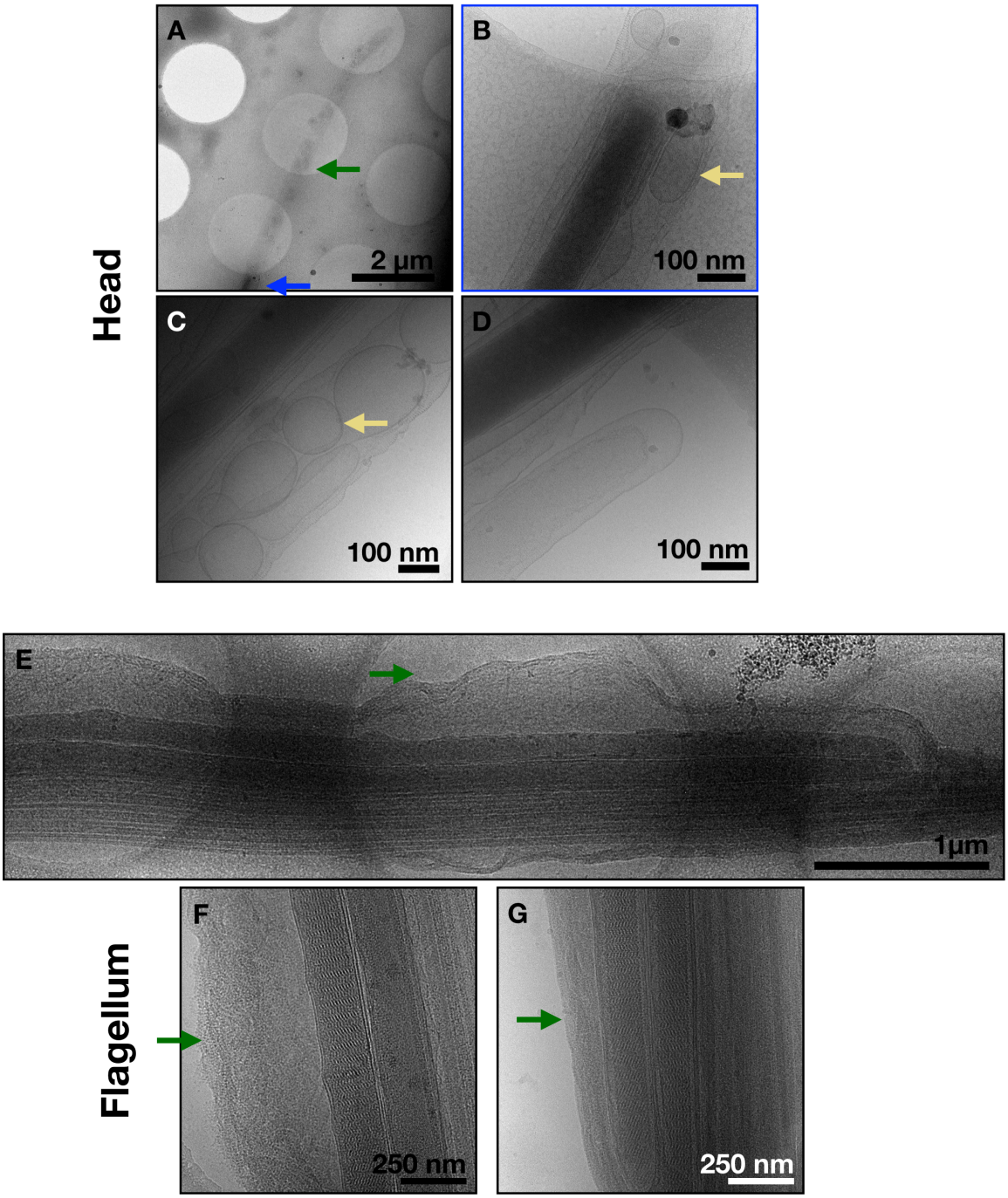

Fig. 2.4. Sperm coat removal in *Aedes aegypti* spermatozoa. The sperm coat (green arrow) is removed from both the head and the flagellum (A-G). The membranous structures removed with the sperm coat are not positively identified, but could be regions of the outer membrane (tan arrows) sperm coat surrounding the head (blue arrow, inset seen in B), is removed intact while regions of the sperm coat surrounding the tail become caught around the tail as it is sloughed (E-G). This is likely due to the tail being responsible for the sperm's motility, while the head is comparatively immobile.

virgin females can produce eggs after a blood meal, mating is typically needed as a stimulus to begin oviposition[19]. However, gravid females, whether virgin or mated, will immediately lay as many eggs as they are able—even if they are unfertilized—if

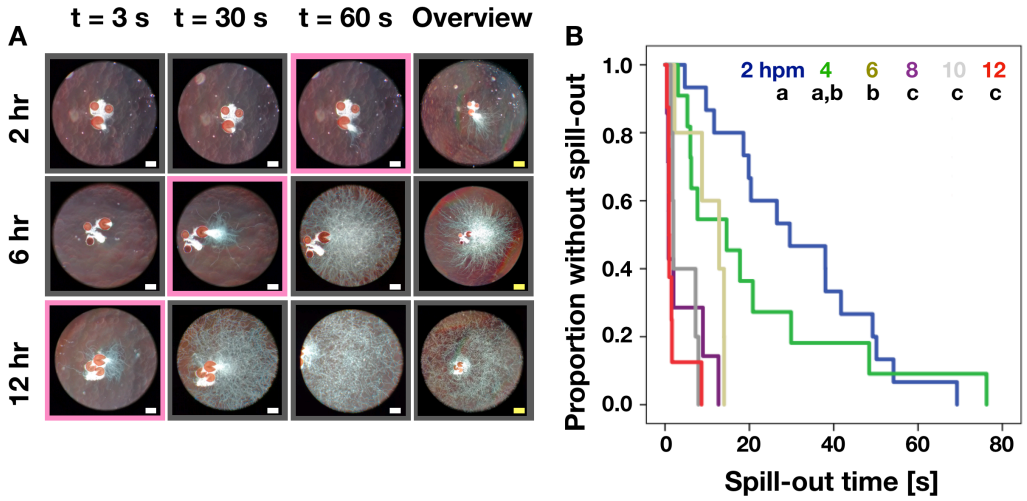

Fig. 2.5. Quiescence in *Ae. aegypti* spermatozoa. *Ae. aegypti* sperm are initially dormant after being stored, but gain rapid motility within 8 h of mating. Females' spermathecae were cracked *in vitro* at different post-mating time intervals, and the time at which 20 sperm had exited the cracked spermathecae (spill-out) was recorded (A-B). Still frames of representative spermathecae at 2 h, 6 h, and 12 h post-mating at 3 s, 30 s, and 60 s post-rupture (A). Frames highlighted in pink show the first time point at which at least 20 sperm have egressed. Fourth frames (Overview) demonstrate differences in the ultimate sperm cloud surrounding spermathecae. A Kaplan-Meier plot of the proportion of females at each post-mating interval for which spill-out has not occurred over time post rupture (B). Lines in figure legend that share at least one letter are not significantly different from each other (Mantel-Cox pairwise comparisons, $p > 0.05$). No significant difference exists between post-mating intervals after 8 hpm. *Scale bars: 100 μm (white), 200 μm (yellow).*

given a death stressor. This response is likely a means of maximizing fitness in the face of imminent death[20]. Thus, we used this feature of female physiology to test the lower limits of when a female could begin to lay fertilized eggs after insemination.

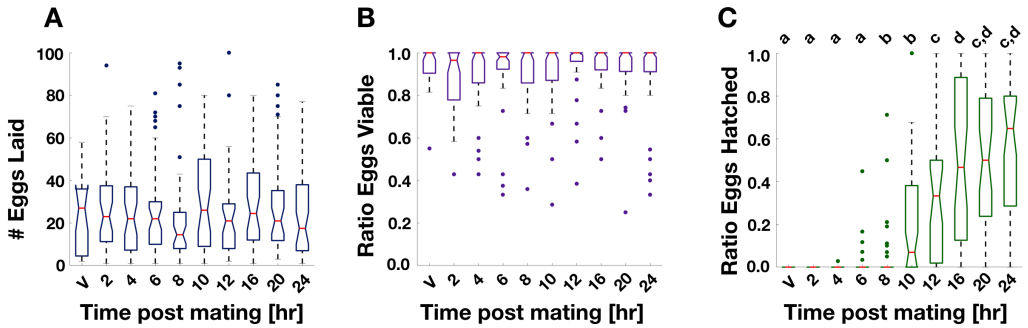

Fig. 2.6. Number of eggs laid (A), proportion of eggs viable (B), and proportion of eggs hatched (C) by individual females in death stress oviposition experiments. n = 34 – 42 for each post-mating interval except virgins (n = 21). Boxes represent inner quartiles, and whiskers and outliers drawn via the Tukey method. (A) Females at all post-mating intervals laid similar numbers of eggs (GLM, df = 394; p > 0.05). (B) Post-mating interval was a significant predictor of whether laid eggs hatched into larvae (GLM, df = 9,357; p = 0.007). However, no significant differences existed in pairwise comparisons after Sidak multiple comparisons ($p > 0.05$). (C) Post-mating interval was significantly correlated with the proportion of eggs that hatched (GLM, df = 7,357; p < 0.001; Figure 1B, Table 1). Post- hoc pairwise comparisons between groups with Sidak multiple comparison correction are indicated with letters, with intervals that share at least one letter not significantly different ($p > 0.05$).

Effect of post-mating interval on fertility

Females forced to oviposit via death stress laid similar numbers of eggs regardless of post-mating interval (Generalized Linear Model, (GLM); $df = 394$; $p > 0.05$ for all tested factors, Table 2.1). Post-mating interval was significantly associated with the number of viable eggs laid by a female (GLM, $df = 9,357$; $p = 0.007$; Table 2.1), with

Model response variable	Variables in model	Likelihood ratio $\chi 2$	*df1*	*df2*	*p*	*F*
Number of eggs						
	Intercept	17.86	1	394	< 0.001	17.86
	Replicate	0.802	1	394	0.371	0.802
	Post-mating interval	4.399	9	394	0.883	0.489
	Striped	0.147	1	394	0.702	0.147
	Replicate*Post-mating interval	7.497	9	394	0.586	0.833
	Replicate*striped	n/a	n/a	n/a	n/a	n/a
	Post-mating interval*striped	0.366	2	394	0.833	0.183
	Replicate*post-mating interval*striped	n/a	n/a	n/a	n/a	n/a
Omnibus test		14.49	23		0.912	
Number of viable eggs						
	Intercept	124.7	1	357	0	124.7
	Post-mating interval	22.63	9	357	0.007	2.514
Omnibus test		22.63	9		0.007	
Number of hatched eggs						
	Intercept	1684	1	357	< 0.001	1684
	Post-mating interval	561.4	7	357	< 0.001	80.2
Omnibus test		561.4	9		< 0.001	

Table 2.1. Results of three generalized linear models testing effects of post-mating interval and replicate. Model for number of eggs includes variables from full factorial design; no variables (except the intercept) were significant after iterative removal of least significant terms. Models for number of viable eggs and number of hatched eggs are final models after iterative removal of non-significant terms.

females at 2 and 4 hpm laying significantly fewer hatched eggs than females at 12, 16, 20, and 24 hours (Sidak, $p < 0.05$; Figure 2.6A, Table 2.1). However, the difference in proportion of viable eggs between post-mating intervals was slight, with the median proportion of viable eggs at all time points falling between 96 and 100%.

Post-mating interval was the only significant predictor of fertility, with females gradually gaining the capacity to fertilize eggs from 4 to 16 hpm (GLM, $df = 7,357$; $p < 0.001$; Figure 2.6B, Table 2.1). The last time point assayed whose proportion of hatched eggs was not significantly different than all later time points was 16 hpm (Sidak, pairwise comparisons, $p < 0.05$).

2.4 Discussion

With these experiments, we have described two previously unreported events in *Aedes aegypti* sperm physiology: the loss of an outer sperm coat in the spermathecae and the quiescence and subsequent recovery of sperm motility in the spermathecae. We have demonstrated that these two processes coincide with the onset of fertility in female *Ae. aegypti*. Thus, we suspect that these modifications to sperm are important steps in the sequence of events required for reproduction in *Ae. aegypti*.

The sperm coat surrounding mosquito spermatozoa has been identified as a glycocalyx through experiments in other insects[21,22]. The sperm glycocalyx is formed in the testis during spermatogenesis[16]. In mosquitoes, the glycocalyx is 10-30 nm thick, and varies in structure. The primary types of insect sperm glycocalyx structure have been identified as the "flea", "fruit fly", and "locust" type[23–26]. The glycocalyx surrounding *Ae. aegypti* spermatozoa is periodic, organized, and most similar to the "locust" glycocalyx type (Appendix A.3).

The proposed functions of the sperm glycocalyx include protecting the sperm from its environment and aiding in transport through the female's reproductive tract. Semen contains enzymes, such as proteases, that could damage sperm[27]. Additionally, the female reproductive tract is known to attack foreign bodies, including sperm, in mammals[28,29]. In insects, including *Ae. aegypti*, the female reproductive tract experiences an upregulation of immune-related transcription after mating, presumably as a defense against potential sexually transmitted infections[30]. To successfully fertilize an egg, sperm would need protection against these potential stressors.

The sperm glycocalyx may also assist in the rapid, mass storage of sperm within the female. Male *Ae. aegypti* can deposit thousands of sperm in a single copulation with a female[31]. These sperm are stored within the female bursa in a matter of seconds, and the spermathecae in a matter of minutes[32]. Just as the glycocalyx is known to aid in sperm transport in mammals, the sperm glycocalyx in *Ae. aegypti* may assist sperm in their ascent up the spermathecal ducts and into the spermathecae. A final proposed role is that the carbohydrate residues that compose the glycocalyx may block the spermathecal duct for a period of time at which females are most likely to take a second mate, preventing the storage of a second male's sperm[33].

The function of the sperm glycocalyx is most clearly elucidated in mammals, and determining an analogous role in insects is challenging. Consequently, the glycocalyx in *Ae. aegypti* spermatozoa may serve one or more of the aforementioned roles, or none at all. No matter its function, the sperm glycocalyx is removed once stored in the

spermathecae. This phenomenon occurs in several other insects. For instance, eupyrene sperm in the silkworm moth *Bombyx mori* shed their sheath prior to fertilization[13]. In the ostracod *Mytilocypris mytiloides*, sperm both dissociate from the sperm sheath and become motile around the time eggs are laid[12].Sperm coat removal during sperm storage has also been documented in other insects while stored in the spermathecae[22,34]. These studies suggest that glycocalyx removal becomes important for some post-storage, pre-fertilization function. Given the timing of glycocalyx removal and fertilization in our experiments, we hypothesize that glycocalyx removal is a prerequisite to fertilizing an egg or is necessary for long term storage and nourishment of the sperm until fertilization can occur.

Prior to these experiments, studying how soon females could fertilize eggs was limited by the fact that females are not stimulated to oviposit until about 16 hours after mating. To overcome this barrier, we took advantage of a natural behavioral response—death stress oviposition—to force females to lay their developed eggs. While it is not a female's normal means of oviposition, the capacity to fertilize eggs in this manner is by no means unnatural. Females sometimes die as they attempt to oviposit, and this behavior is a means of realizing any possible reproductive fitness in the case of imminent death[20]. Forcing females to lay eggs in this way allows us to probe the absolute limits of when females are first able to lay fertilized eggs. Using this technique, we have shown that some females are capable of fertilizing eggs as early as 4 hours post-mating—a time that coincides with the removal of a sperm coat and the onset of sperm motility. To be clear, these concomitant observations alone do

not causally link either coat loss or motility with fertilization capacity. Nonetheless, it has allowed us to show that females, given adequate conditions, can begin to fertilize eggs within 4 hours of mating. This timeline will guide future investigations of the molecular, cellular, and physiological mechanisms that lead to successful fertilization in *Ae. aegypti*.

Definitively identifying relationships—if any—between our observed phenomena will require clever experiments to elucidate the molecular and physiological underpinnings of specific reproductive events. For example, Adlakha and Pillai uncoupled the receipt of sperm and semen by female mosquitoes by surgically removing their source organs in males[35]. In the silkworm *Bombyx mori*, females that only received sperm stored them but were unable to fertilize eggs. In both mosquitoes and *Bombyx mori,* females that received only sperm were at first infertile, but subsequent mating to males with only semen rescued the capacity to fertilize eggs. In *Drosophila,* the effect of spermathecal secretory cells on reproductive function was investigated by genetically ablating these sperm-nourishing organs. Similar experiments in mosquitoes could determine, for example, whether coat removal is triggered by semen or initiated by the female.

2.5 Conclusions

In this study, we described the first instance of post-copulatory changes to stored spermatozoa in *Aedes aegypti* mosquitoes. Using sperm harvested from sexually mature, virgin males as a reference, we determined that sperm undergo no noticeable

morphological changes while stored in the female's bursa. However, sperm stored in the female's spermathecae undergo morphological changes involving the removal of the sperm coat and the outer membrane along the length of the sperm. The morphological changes initiate soon after post-mating, and largely conclude 12 hours post mating. Additionally, sperm stored in the spermathecae are quiescent for 4 h after mating, after which sperm motility is gradually restored. These phenomenological changes coincide with the ability of *Aedes aegypti* to lay fertilized eggs, which also initiates around 4 hours post mating. The proportion of laid eggs that hatch gradually increases until plateauing at 16 hpm. Further experiments are necessary to determine the molecular basis for sperm coat removal as well as its potential functions. A comprehensive understanding of the reproduction biology of this medically important mosquito species may inform future targets for vector control disease prevention.

2.6 Methods

Mosquito rearing

Aedes aegypti mosquitoes were taken from a laboratory strain originally colonized using field collected individuals in Bangkok, Thailand. This colony was initiated in 2011 and supplemented every 2 – 3 years with new field collected individuals from the same location. All mosquitoes were reared using established protocols and environmental conditions[33].

Plunge-freezing vitrification: 3 μL of sperm isolated from either male seminal vesicles, female bursae 3 min after mating, or female spermathecae at various times

after mating suspended in buffer were pipetted onto R2/1 Quantifoil grids with hole sizes of ~2 μm (Quantifoil Micro Tools, Jena, Germany). The grids were blotted from the reverse side and immediately plunged into a liquid ethane/propane mixture at liquid nitrogen temperature using a custom-built vitrification device (MPI, Martinsried, Germany). The plunge-frozen grids were stored in sealed cryo-boxes in liquid nitrogen until used.

Cryo-TEM. Cryo-TEM was performed on a Titan Themis (Thermo Fisher Scientific, Waltham, MA) operated at 300 kV in energy-filtered mode equipped with a high brightness field-emission gun, and either a 2048x2048 Ceta 16M (Thermo Fisher Scientific, Waltham, MA), or a 3838x3710 pixel Gatan K2 Summit direct detector camera (Gatan, Pleasanton, CA) operating in counted, dose-fractionated mode. Images were collected at a defoci of -1 μm and -3 μm. Images were binned by 2, resulting in pixel sizes of 0.51-1.09 nm.

Death Stress Oviposition

Virgin females 2-4 days post-eclosion (dpe) were offered a blood meal from ECD's arm after having been starved of sugar for 24 h. Females that did not feed were given a second opportunity to feed later that day. Females that still did not feed were discarded. After feeding, females were given 10% sucrose *ad libitum* and held in growth chamber conditions for 7 d. After 7 d, females were given 30 min to mate with males at a ratio of 1:1. After removing males, females were held in sexual isolation for 2, 4, 6, 8, 10, 12, 16, 20, or 24 h. After this period, each females' head was removed,

and carcasses were placed individually on top of a wet filter paper disk in the well of a 96-well plate. After decapitation, the well was covered with masking tape and the plate was placed in a plastic bag with a wet paper towel. Females were allowed to death stress oviposit for 1 h. After 1 h, females were removed from the wells, the masking tape was replaced, and eggs were given 3 d to embryonate. Removed females' spermathecae were then dissected to verify that they had mated; females that did not mate were removed from analysis. To avoid excessive mold growth, excess water was wicked away from saturated filter paper from each well 1 d after oviposition.

After embryonation, eggs in each well were counted and scored as either viable (convex, fully melanized, and normally shaped) or unviable (deflated, not melanized, or irregularly shaped). Wells with moldy eggs were noted, as well as wells in which some eggs had an abnormal phenotype characterized by stripes without tubercles. After counting and characterizing each well, wells were flooded with 200 µL deionized water and returned to the environmental chamber for 7 d. After 7 d, wells were vacuum hatched for 30 min, after which the total number of hatched larvae in each well was counted. This entire experiment was conducted twice with different cohorts of mosquitoes.

Motility Assays

Females 5 – 8 dpe were allowed to mate with males for half an hour at a 1:1 ratio. After this mating period, males were removed and females were maintained in growth

chamber conditions until assayed for motility. Females were dissected in saline buffer designed to be isotonic to and of the same pH as mosquito hemolymph[36]. Each female's spermathecal triplet was removed and transferred to a fresh drop with 60 μL of saline. A glass coverslip was gently placed over the spermathecae, and the uncracked spermathecae were placed on a compound microscope with 200x total magnification and dark-field illumination. The largest (medial) spermatheca was cracked by slowly wicking saline from the side of the coverslip with a Kimwipe. Immediately after cracking, the removal of saline ceased to allow sperm space to move and leave the spermathecae. Videos of the spermathecae and the sperm they contained were recorded from crack to 2 min after cracking. Any spermathecae that cracked before video was recorded or that had tissue (oviduct or spermathecal ducts) that covered the location of the crack was removed from analysis. As an estimation of the relative motility of sperm inside the spermathecae, the time taken for 20 sperm heads to leave the medial spermatheca was recorded.

Data Analysis

Motility. Spill out time (the time at which 20 sperm had exited the spermathecae after cracking) was analyzed using Kaplan-Meier survival analysis, with Mantel-Cox post hoc pairwise comparisons. Females were binned into their closest 2 hpm increment (all dissections were conducted within 1 h of each time point).

Oviposition and Fertility:

In our death stress oviposition experiment, each time point initially included between 58 and 63 females. For each well, the number of eggs, the number of viable eggs (as defined by convex shape and proper melanization), and the number of hatched larvae were recorded. At times, females laid many eggs on top of each other, preventing their exact enumeration without damaging the eggs. In such cases, we estimated the total number of eggs by counting those that were visible and estimating how many were not visible. We also recorded whether "striped" eggs were present; we noticed that occasionally an egg would have stripes in which tubercles did not form in the chorion, creating a glassy texture. Each female's spermathecae were checked for sperm, indicating her mating status.

All wells in which mold had grown were removed from analysis (n = 128). Females whose spermathecae did not contain sperm were identified as virgins, and were included in models as females at 0 hpm (n = 23). For analysis of the total number of eggs laid, all females were included (n = 418). For analysis of the proportion of eggs that were viable, all females that laid at least one egg were included (n = 367). For analysis of fertility, only females with at least one viable egg were included (n = 367). Our data showed that 9 out of 346 females had slightly more hatched eggs than the number that were initially counted, due to the need to occasionally estimate egg number. The difference between larvae and egg counts was at most 8, and averaged to 4.3. Because all of these instances were in the 16, 20, or 24 hpm time points, and because similar error may exist in earlier time points but not be apparent due to fewer

larvae hatched, we chose to keep these females in our analysis. In figures, these points are forced to 1 in order to not mis-represent these proportional data.

Forced oviposition data were analyzed using three generalized linear models with a Poisson distribution and log link, modeling: the number of eggs laid, the viability of eggs, and the fertility of a female (defined by the number of eggs hatched). In the number of eggs model, no offset variable was used. In the viability model, the number of viable eggs was offset by the natural log of the number of total eggs. In the fertility model, the number of fertile eggs was offset by the natural log of the number of viable eggs. Hour post mating (hpm) was included as a covariate (with virgins given the value of 0 hpm). Cohort and striped were included as factors. All three models were initially over-dispersed; therefore the Pearson-chi square was used as a scale parameter in final models. Models were constructed iteratively, beginning with all main effects and factorial interactions between predictors. After each iteration, the least significant term (and any interactions that contained it) was removed until all remaining terms were significant ($p < 0.05$).

2.7 Acknowledgements

The authors would like to thank Sylvie Pitcher for their assistance in rearing mosquitoes, and Scott Pitnick, Steve Dorus, and Susan Suarez for their fruitful discussion.

REFERENCES

1. Bhatt, S. *et al.* The global distribution and burden of dengue. *Nature* **496,** 504–507 (2013).

2. Brady, O. J. *et al.* Refining the global spatial limits of dengue virus transmission by evidence-based consensus. *PLoS Negl. Trop. Dis.* **6,** e1760 (2012).

3. Craig, G. B. Mosquitoes: female monogamy induced by male accessory gland substance. *Science* **156,** 1499–501 (1967).

4. Gulia-Nuss, M., Eum, J.-H., Strand, M. R. & Brown, M. R. Ovary ecdysteroidogenic hormone activates egg maturation in the mosquito Georgecraigius atropalpus after adult eclosion or a blood meal. *J. Exp. Biol.* **215,** 3758–3767 (2012).

5. Degner, E. C. & Harrington, L. C. A mosquito sperm's journey from male ejaculate to egg: mechanisms, molecules, and methods for exploration. *Mol. Reprod. Dev.* **83,** 897–911 (2016).

6. Patrat, C., Serres, C. & Jouannet, P. The acrosome reaction in human spermatozoa. *Biol. cell* **92,** 255–66 (2000).

7. Stival, C. *et al.* in *Advances in anatomy, embryology, and cell biology* **220,** 93–106 (Springer, Cham, 2016).

8. Ickowicz, D., Finkelstein, M. & Breitbart, H. Mechanism of sperm capacitation and the acrosome reaction: role of protein kinases. *Asian J. Androl.* **14,** 816–21 (2012).

9. Birkhead, T. R., & Møller, A. P. Sexual selection and the temporal separation of reproductive events: sperm storage data from reptiles, birds and mammals. *Biol. J. Linn. Soc.* **50,** 295–311 (1993).

10. Austin, C. R. The 'Capacitation' of the Mammalian Sperm. *Nature* **170,** 326–326 (1952).

11. Gadella, B. M. & Visconti, P. E. in *The Sperm Cell* (eds. De Jonge, C. J. & Barratt, C.) 134–169 (Cambridge University Press, 2006).

12. Matzke-Karasz, R., Smith, R. J., & Heß, M. Removal of extracellular coat from giant sperm in female receptacle induces sperm motility in *Mytilocypris mytiloides* (Cyprididae, Ostracoda, Crustacea). *Cell Tissue Res.* **368,** 171–186 (2017).

13. Friedländer, M. & Gitay, H. The fate of the normal-anucleated spermatozoa in inseminated females of the silkworm *Bombyx mori*. *J. Morphol.* **138,** 121–129 (1972).

14. Longo, G., Sottile, L., Viscuso, R., Giuffrida, A. & Privitera, R. Ultrastructural changes in sperm of *Eyprepocnemis plorans* (Charpentier) (Orthoptera: Acrididae) during storage of gametes in female genital tract. *Invertebr. Reprod. Dev.* **24,** 1–6 (1993).

15. Chapman, R. F. *The Insects : Structure and Function*. 282-310 (Cambridge University Press, 1998).

16. Ndiaye, M., Mattei, X. & Thiaw, O. T. Maturation of mosquito spermatozoa during their transit throughout the male and female reproductive systems. *Tissue Cell* **29,** 675–8 (1997).

17. Báo, S. N. & de Souza, W. Ultrastructural and cytochemical studies of the spermatid and spermatozoon of Culex quinquefasciatus (Culicidae). *J. Submicrosc. Cytol. Pathol.* **25,** 213–22 (1993).

18. Ndiaye, M. & Matte1, X. Process of nuclear envelope reduction in spermiogenesis of a mosquito, *Culex tigripes*. *Mol. Reprod. Dev.* **34,** 416-419, (1993).

19. Judson, C. L. Feeding and oviposition behavior in the mosquito *Aedes aegypti* (L.). I. preliminary studies of physiciological control mechanisms. *Biol. Bull.* **133,** 369–377 (1967).

20. Chadee, D. D. & Ritchie, S. A. Oviposition behaviour and parity rates of *Aedes aegypti* collected in sticky traps in Trinidad, West Indies. *Acta Trop.* **116,** 212–216 (2010).

21. Baccetti, B., Bigliardi, E. & Rosati, F. The spermatozoon of arthropoda XIII. The cell surface. *J. Ultrastruct. Res.* **35,** 582–605 (1971).

22. Baccetti, B. Insect Sperm Cells. *Adv. In Insect Phys.* **9,** 315–397 (1972).

23. Roth, L. E. The spermatid cell membrane in *Melanoplus differentialis*. *J. Biophys. Biochem. Cytol.* **3,** 816–9 (1957).

24. Baccetti, B., Bigliardi, E. & Rosati, F. The spermatozoon of Arthropoda XIII. The cell surface. *J. Ultrastruct. Res.* **35,** 582–605 (1971).

25. Baccetti, B. & Afzelius, B. A. The biology of the sperm cell. *Monogr. Dev. Biol.* **10,** 1–254 (1976).

26. Kessel, R. G. An electron microscope study of spermiogenesis in the

grasshopper with particular reference to the development of microtubular systems during differentiation. *J. Ultrastruct. Res.* **18,** 677–694 (1967).

27. Sirot, L. K., Wolfner, M. F. & Wigby, S. Protein-specific manipulation of ejaculate composition in response to female mating status in Drosophila melanogaster. *Proc. Natl. Acad. Sci.* **108,** 9922–9926 (2011).

28. Brazdova, A., Senechal, H., Peltre, G. & Poncet, P. Immune aspects of female infertility. *Int. J. Fertil. Steril.* **10,** 1–10 (2016).

29. Naz, R. K. & Menge, A. C. Antisperm antibodies: origin, regulation, and sperm reactivity in human infertility. *Fertil. Steril.* **61,** 1001–13 (1994).

30. Alfonso-Parra, C. *et al.* Mating-induced transcriptome changes in the reproductive tract of female *Aedes aegypti*. *PLoS Negl. Trop. Dis.* **10,** e0004451 (2016).

31. Ponlawat, A. & Harrington, L. C. Factors associated with male mating success of the dengue vector mosquito, *Aedes aegypti*. *Am. J. Trop. Med. Hyg.* **80,** 395–400 (2009).

32. Clements, A. N. & Potter, S. A. The fine structure of the spermathecae and their ducts in the mosquito *Aedes aegypti*. *J. Insect Physiol.* **13,** 1825–1836 (1967).

33. Degner, E. C. & Harrington, L. C. Polyandry depends on postmating time interval in the dengue vector *Aedes aegypti*. *Am. J. Trop. Med. Hyg.* **94,** 780–785 (2016).

34. Riemann, J. G. & Thorson, B. J. Sperm maturation in the male and female genital tracts of *Anagasta kühniella* (Lepidoptera: Pyralididae). *Int. J. Insect Morphol. Embryol.* **1,** 11–19 (1971).

35. Adlakha, V. & Pillai, M. K. Involvement of male accessory gland substance in the fertility of mosquitoes. *J. Insect Physiol.* **21,** 1453–5 (1975).

36. Hayes, R. O. Determination of a physiological saline solution for *Aedes aegypti* (L.). *J. Econ. Entomol.* **46,** 624–627 (1953).

CHAPTER 3

A COMPARATIVE ANALYSIS OF TECHNIQUES USED TO INVESTIGATE EXTRACELLULAR VESICLE SHEDDING

3.1 Summary

Cells secrete extracellular vesicles, which are involved in cell-to-cell communication. Several microscopy and analytical techniques have been used to assess vesicle formation, secretion, and morphology. However, the limitations of each technique prevent comprehensive analysis of these phenomena. Assessing the strengths and limitations of these instruments could inform how to pair techniques in a complimentary way to fully understand the mechanistic pathway of vesicle secretion into the extracellular environment. In this study, we evaluated the capabilities of florescence microscopy, SEM, and cryo-SEM in understanding the formation and shedding of extracellular vesicles from parental and hyaluronan synthase 3-(HAS3) overexpressing MCF10A cells. Cells imaged with conventional and cryo-SEM had different morphologies due to the sample preparation processes for each technique. However, the combination of techniques confirmed the presence of tubular structures protruding from the surfaces of both cell lines. Additionally, the HAS3-MCF10A extensions contained microvesicles along their length. Vesicles that have been shed from these cells were further characterized using nanoparticle tracking analysis (NTA). While both techniques confirmed the presence of extracellular vesicles, the size distributions obtained by each technique were different in the range of vesicles

analyzed and the relative proportion of smaller to larger vesicles. This difference is attributed to the presence of biological debris in the media, which is difficult to differentiate from vesicles in NTA. Our study emphasizes the necessity of pairing several techniques to provide a complete profile of extracellular vesicle characterization.

3.2 Introduction

Cells secrete a variety of membrane-bound structures into the extracellular environment. These structures, collectively called extracellular vesicles (EVs), play a key role in long-range cell-to-cell communication by delivering specific cargos to other cells or the extracellular space (Antonyak et al., 2011; Yuana et al., 2013). Two subtypes of EVs are exosomes (~50-100 nm), and microvesicles (MVs; ~100 nm-1 μm). Exosomes are secreted via exocytosis from endosomal multivesicular bodies, and microvesicles are directly shed from the plasma membrane (Muralidharan-Chari et al., 2010). EVs are shed by cells under both physiological and pathological conditions (Desrochers et al., 2016; Furie and Furie, 2004; György et al., 2011; Kim et al., 2002; Liu et al., 2014; Tannetta et al., 2014; van der Pol et al., 2012), including tumor metastasis (Becker et al., 2016; Le et al., 2014).

Understanding EV biogenesis and secretion requires instrumentation that can accommodate the inherent nature of vesicle-shedding cells. The formation of EVs is associated with structural modifications in the cell's plasma membrane, a nanoscale phenomenon best assessed with high-resolution imaging methodologies (van Niel et

al., 2018). Techniques such as scanning electron microscopy (SEM) provide such resolving power, and are routinely used for cell imaging. Biological samples prepared for conventional SEM are chemically fixed and dehydrated, often introducing artifacts. For soft matter materials with high water content, a viable alternative to SEM is cryo-SEM. In this technique, samples are preserved in a near-native state through vitrification, and imaged with cryo-SEM under cryogenic conditions (Dubochet and McDowall, 1981). Although used extensively to understand plant structure and physiology, cryo-SEM has been recently adopted to examine cancer cell morphology and EV shedding (Charuvi et al., 2016; Cochard et al., 2000; Koifman et al., 2017; McCully et al., 2009; Utsumi et al., 1998).

Analysis of EV size, concentration, and composition is also performed through various analytical techniques. Nanoparticle tracking analysis (NTA) can determine the diameters of EVs by measuring the diffusion constants of suspended particles in Brownian motion and solving the Stokes-Einstein equation to determine their hydrodynamic diameters (Soo et al., 2012). Transmission electron microscopy (TEM) is another technique used to characterize both the size and morphology of secreted vesicles. The “cup-shaped” vesicles reported in previous literature are artifacts of the conventional TEM sample preparation process, and are eliminated by preserving EVs in a near-native state by vitrification (van Niel et al., 2018). Because the structures of frozen vesicles are directly interpretable, cryo-TEM is becoming more commonplace for analyzing EVs. Both NTA and cryo-TEM imaging of EVs typically involve harvesting of vesicles from cell cultures and separate analysis.

In this study, we compared three techniques commonly used for analyzing vesicle-shedding cell lines—florescence microscopy, SEM, and cryo-SEM—in their ability to characterize cell morphology and EV development. Additionally, we compared NTA and cryo-TEM in their ability to characterize EVs that had been secreted into the extracellular environment.

3.3 Materials and Methods

Cell lines and culture. MCF10A cells were obtained from ATCC (Manassas, VA). MCF10A cells were cultured in DMEM/F12 basal media supplemented with 5% horse serum, 20 ng/mL EGF, 10 μg/mL insulin, 500 ng/mL hydrocortisone, 100 ng/mL cholera toxin, and penicillin/streptomycin. MCF10A rtTA cells were produced through lentiviral transfection of a tetracycline-inducible vector. HAS3-MCF10A rtTA cells were produced through lentiviral transfection with a pLV TetOn HAS vector. All cell lines were maintained at 37°C and 5% CO_2.

Cell culture on grids. All grid handling was carried out inside glass-bottom dishes (MatTek, 35-mm dish diameter, 20 mm glass) under sterile conditions. Quantifoil R1/4 holey carbon 200 mesh gold TEM grids (Quantifoil Micro Tools, Jena, Germany) underwent glow discharge for 10 seconds to improve hydrophilicity. Grids were then sterilized in 70% ethanol and washed with DI water three times. For fibronectin coating, grids were incubated in 30 μL/mg DI water, 37°C, for 2 hours. After coating, grids were washed with DI water three times, followed by washing with

culture media and incubation in culture media for 1 hour. HAS3-MCF10A rtTA cells and MCF10A rtTA cells were plated at a density of 300,000 cells/2 mL of media. Cells were induced with 1 μg/mL doxycycline for 48 hours.

Fluorescence labeling and imaging. Grids were washed twice with PBS buffer and fixed with 10% formalin at room temperature for 20 minutes. The formalin was aspirated and grids were washed three times for 2 minutes each with PBSX (0.05% TritonX in PBS). Florescence staining solutions DAPI (1:5000) and Phalloidin Alexa 488 (1:200) in 1% BSA/PBS were prepared and kept covered with aluminum foil. Grids were immersed and incubated in the florescence staining solutions at room temperature for 1 hour, followed by two washes with PBS. Grids were imaged under PBS using a Zeiss LSM 710 Confocal Microscope with 40x water immersion objective, and 405 nm (DAPI) and 488 nm (Alexa Fluor 488) lasers with pinhole of 36.2 μm and emission wavelengths of 452.5 nm and 562.5 nm. Z stacks were acquired with 0.46 μm intervals. The stack was processed using ImageJ.

SEM imaging. Cells were fixed on TEM grids using Trump's fixative (4 mL 10x PBS, 10 mL 16% PFA, 4 mL 10% GA, 22 mL ddH_2O). First, grids were rinsed with Trump's fixative at 37°C, which was aspirated immediately. Fresh Trump's fixative was added at 37°C and grids were stored at 4°C overnight before aspiration. Grids were then immersed in 1% osmium tetroxide in 0.05M cacodylate buffer on ice for 40 minutes. Cacodylate buffer was added in excess for 10 minutes and aspirated. Fresh

buffer was added for another 10 minutes. This process was repeated twice. Grids were washed with 25% and 50% EtOH on ice for 10 minutes, followed by 70% EtOH overnight. Grids were washed with 95%, 100%, 100% EtOH on ice for 10 minutes before undergoing critical point drying. Samples were coated with Au-Pd (at 10 mA for 15 seconds) and imaged in a Mira3 FESEM (Tescan, Czech Republic). High-resolution images were acquired at 5 keV and a 3 mm working distance with the in-beam secondary electron detector. Brightness and contrast were adjusted using Adobe Photoshop.

Extracellular vesicle isolation. All cell lines were grown to high confluency at 10,000 cells/cm^2 in T-150 flasks for 42 hours and induced as described above. Cells were rinsed with PBS twice before being serum starved for 6 hours to avoid contamination of nascent exosomes from serum. Following serum starvation, media was harvested and clarified at 600 relative centrifugal force (rcf) for 5 minutes, then 2 mL of media was collected and spun at 600 rcf for 5 minutes. 1.5 mL of media was collected as the final volume for experiments. Cells were detached and combined with any detached cells due to doxycycline induction and counted to obtain the concentration of cells for calculating the extracellular vesicle production rate (vesicles/cell/6 hours).

Nanoparticle Tracking Analysis. To quantify extracellular vesicles released from the cells, harvested media were analyzed using the Nanosight NS300 (Malvern) nanoparticle tracking analysis instrument. Following particle tracking captures,

samples were recovered from the device post-NTA for correlative analysis by cryo-TEM.

Plunge-freezing vitrification. 3-5 μL of harvested media were pipetted onto holey carbon 200 mesh copper grids (Quantifoil Micro Tools, Jena, Germany) with hole sizes of ~2 μm. The grids were blotted from the reverse side and immediately plunged into a liquid ethane/propane mixture cooled to liquid nitrogen temperature using a custom-built vitrification apparatus (MPI, Martinsried, Germany). The plunge-frozen grids were stored in sealed cryo-boxes in liquid nitrogen until used.

Cryo-SEM. Frozen grids were imaged in an FEI Strata 400 STEM FIB equipped with Quorum PP3010T Cryo-FIB/SEM Preparation System that enables cryogenic experiments. First, grids were heated from -150°C to -100°C for 20 minutes and then -90°C for 1 minute to allow for water sublimation and to expose the cell surface. Grids were then coated with Au-Pd at 10 mA for 10 seconds in the Quorum preparation chamber. High-resolution images were acquired at -165°C, 3 keV and 68 pA and a working distance of 7 mm with a secondary electron Everhart-Thornley Detector (ETD). Brightness and contrast were adjusted using Adobe Photoshop.

Cryo-TEM. Cryo-TEM was performed on a Titan Themis (Thermo Fisher Scientific, Waltham, MA) operated at 300 kV in energy-filtered mode equipped with a high brighteness field-emission gun (XFEG), and a 3838x3710 pixel Gatan K2 Summit direct detector camera (Gatan, Pleasanton, CA) operating in counted, dose-

fractionated mode. Images were collected at defoci between -1 and -3 μm. Images were binned by 2, resulting in pixel sizes of 0.51-1.09 nm.

3.4 Results/Discussion

MCF10A and HAS3-MCF10A cell lines were used in this study. MCF10A (10A) is a non-tumorigenic, human mammary epithelial cell line used here as a well-characterized control cell line. HAS3-10A cells are hyaluronic acid synthase-3 (HAS3)-overexpressing MCF10A cells. HAS3 overexpression is known to induce unique cellular structures, enhance cell invasion and migration, and increase MV shedding in parental cell lines (Koistinen et al., 2015; Rilla et al., 2013; Kuo, 2017).

3.4.1 Culturing cells onto TEM grids

Cells prepared for electron microscopy are traditionally cultured in Petri dishes, trypsanized, pelleted by centrifugation, resuspended, and pipetted onto an EM grid before analysis with electron microscopy. During any step in this process, cells may undergo non-physiological structural modifications. To remove intermediate sample processing steps, 10A and HAS3-10A cells were cultured directly onto fibronectin-coated gold TEM grids for 48 hours. (Fig. 3.1). Cells grew uniformly in areas coated with fibronectin, both on and off the grid (Fig. 3.1A). The concentration of cells cultured onto the electron-transparent grid squares was sufficiently high for imaging (Fig. 3.1B), and the morphology of cells cultured onto TEM grids was similar to those prepared on traditional substrates, such as glass or polystyrene (Fig. 3.1C). Grids were chemically fixed for confocal microscopy and SEM, and vitrified for cryo-SEM.

3.4.2 Morphology of cells observed by RT- and cryo-SEM

Chemically-fixed cells imaged with SEM were flattened with tubular extensions protruding from the cell surfaces of both 10A and HAS3-10A cells (Fig. 3.2A,C). Cells observed with cryo-SEM appeared rounded, and the cells'

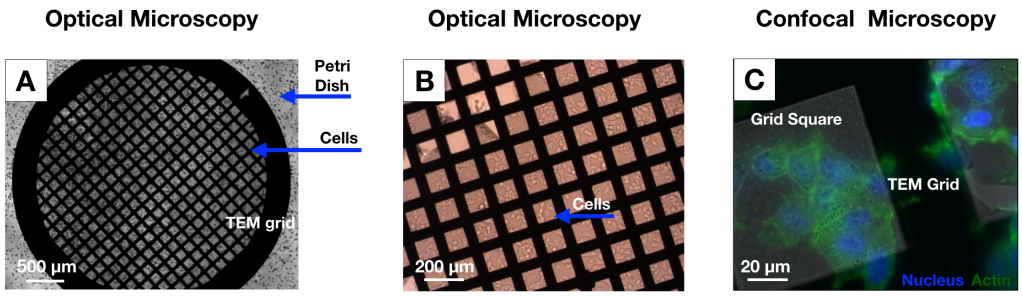

Fig. 3.1. On-grid cell culture. MCF10A and HAS3-MCF10A cells were seeded onto gold TEM grids covered in fibronectin. The cells grew uniformly on the grid, including in the electron-transparent grid squares (A-C). Cells grew in the grid squares at sufficiently high densities for imaging with electron microscopy (B-C). The cells cultured directly onto TEM grids had similar morphologies as those cultured onto traditional substrates, such as glass or polystyrene (C).

top surfaces were smooth (Fig. 3.2B,D). Furthermore, tubular extensions are present in the cryo-SEM images as well, confirming that they are not a fixation artifact. In cryo-SEM however, these extensions on the cell surface lay flat against the grid. Although this is somewhat evident in 10A cells (Fig. 3.2B), recumbent extensions are very prominent in HAS3-10A cells (Fig. 3.2D). The roundedness or flatness of cells cannot be attributed to variation in adhesion between cell types, as both 10A and HAS3-10A are adherent cell lines. Instead, we hypothesize that the morphological differences of cells observed in conventional and cryo-SEM are both the consequences of the sample preparation process for each technique. Cells are dehydrated during the chemical

fixation process, and the lack of water content may cause cells to appear flatter than if they were preserved in a liquid-hydrated state. On the other hand, the force of plunge-freezing due to blotting likely affects the extensions on the cell surface, causing them to lie flat on the TEM grid. Consequently, the appropriate technique depends on the structure of the cell. If imaging cell extensions, such as filopodia or microvilli, then conventional SEM is the method of choice. Cryo-SEM is best used to image cells that lack significant structures protruding from the surface, cells whose native morphologies are unknown, and when morphological differences between cell lines are important. A reasonable approach is to use both techniques, leveraging the strengths of one approach to compensate for the limitations of another.

Combining data obtained from both techniques provided several insights into the endogenous morphological differences between 10A and HAS3-10A cells. Figure 3.3A shows the presence of rounded features on the surfaces of 10A cells. Similar features were present on the surfaces of HAS3-10A cells as well. Although dimensionally consistent with MVs, further investigation with high-resolution imaging techniques are necessary for a positive identification. HAS3-10A cells show a high intensity of actin expression when compared to the control (Fig. 3.3C,D). The higher intensities in HAS3-10A cells are attributed to an increased density of actin microfilaments contained within tubular extensions protruding from the cell surface (Fig. 3.2B,C; D,E). These structures are thin and finger-like, and no wider than 100-200 nm in diameter (Fig. 3.3B-C). Although 10A cells also have tubular extensions, they are both shorter and less numerous than the extensions seen in HAS3-10A cells

(Fig.3.2A). HAS3-10A extensions interact with neighboring cells in a manner not observed in 10A cells (Fig. 3.2C). Finally, the HAS3-10A tubular extensions contain numerous structures that are dimensionally consistent with MVs along their length, suggesting an additional means of trafficking MVs into the extracellular environment (Fig. 3.3B-C,F). MVs were not found on the

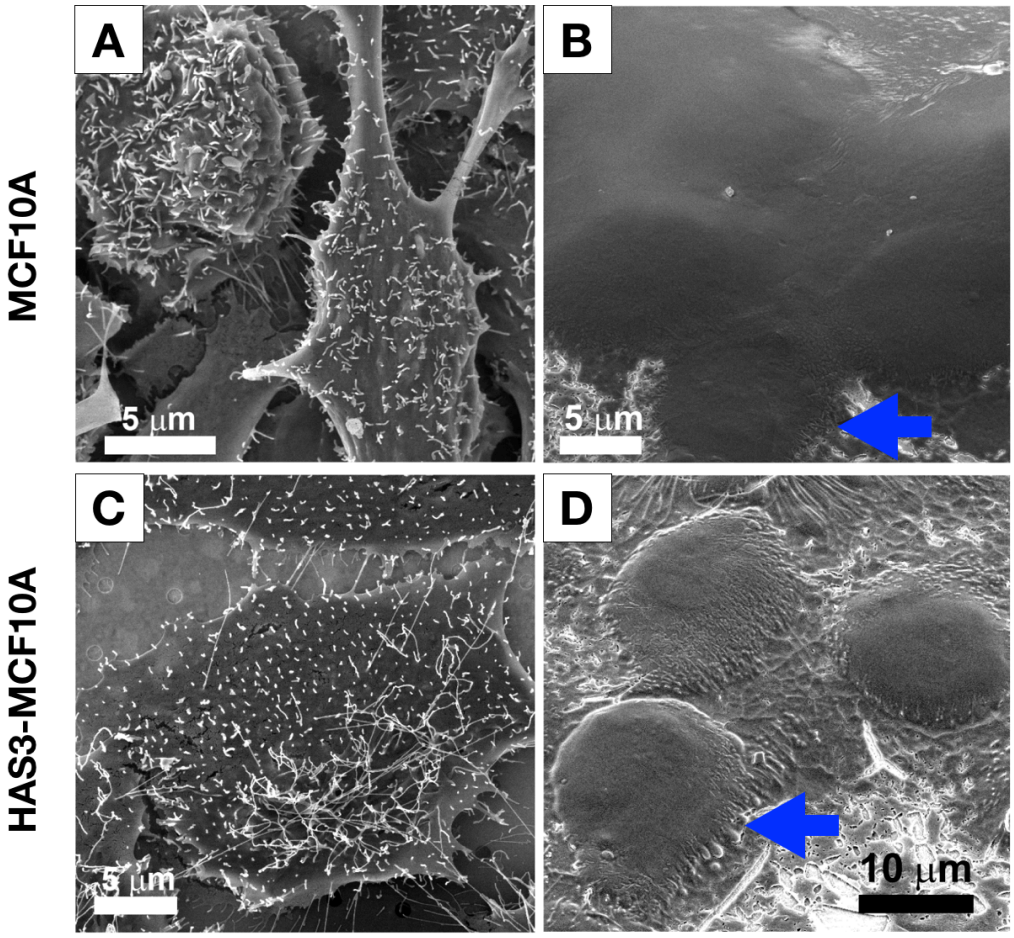

Fig. 3.2. Morphologies of cells prepared for conventional and cryo-SEM. MCF10A cells prepared for conventional SEM (A) appeared flatter than those prepared for cryo-SEM (B). The same phenomenon is seen in HAS3-MCF10A cells (C-D). The tubular extensions of cells prepared for cryo-SEM lay flat against the grid (B,D, blue arrows), while the extensions of those prepared for conventional EM appear to project from the cell surface (A,C).

tubular extensions in 10A cells, and appear only to form from the surface of the plasma membrane in this cell line.

3.4.3 NTA vs. TEM particle diameter distributions

The diameter distributions of EVs secreted from 10A and HAS3-10A cells were analyzed by NTA. HAS3-10A cells secrete a greater concentration of vesicles than 10A cells (Fig. 3.4A). This is consistent with prior literature reporting that non-tumorigenic cells do not shed EVs in high proportions (D'Souza-Schorey and Clancy, 2012). When preparing samples for analysis with cryo-TEM, we discovered that 10A vesicles did not always adhere uniformly and densely onto the TEM grid. The comparatively lower EV concentration secreted from 10A cells combined with lower adhesion to the TEM grid translated into sparse populations of 10A vesicles on the grids and lower sample statistics. As a result, cryo-TEM analysis of vesicle diameters was performed only on HAS3-10A EVs.

Cryo-TEM revealed that the secreted EVs of HAS3-10A cells were heterogeneous in both shape and diameter (Fig. 3.4B-D). Vesicles historically designated as MVs contained surface structure, while those historically designated as exosomes did not (Fig. 3.4B-D). The differences in surface structure might be attributed to the differences in the biogeneic pathways of exosomes and MVs. MVs might adopt the cell's glycocalyx while shedding from the cell's plasma membrane, while exosomes, which are endosomally trafficked and released from the cell through exocytosis, may

not contain a glycocalyx. In the future, such information could be used in conjunction with particle size measurements to differentiate between subpopulations of EVs. Because the native structure remains unaltered, we expect cryo-TEM to provide an accurate analysis of vesicle diameter, which can be used for a more faithful comparison to NTA data.

The particle distributions of secreted HAS3-10A EVs collected by NTA and cryo-TEM have few points of commonality (Fig. 3.5). The concentration of vesicles decreases with size in both distributions. Besides this, the distributions are not the same. The NTA data tracked particles ranging from 20-1000 nm in diameter with peaks around 50 nm (Fig. 3.5A). The distribution of vesicles identified with cryo-TEM is broader, ranging from 20-1275 nm in diameter. The strongest peak in the cryo-TEM

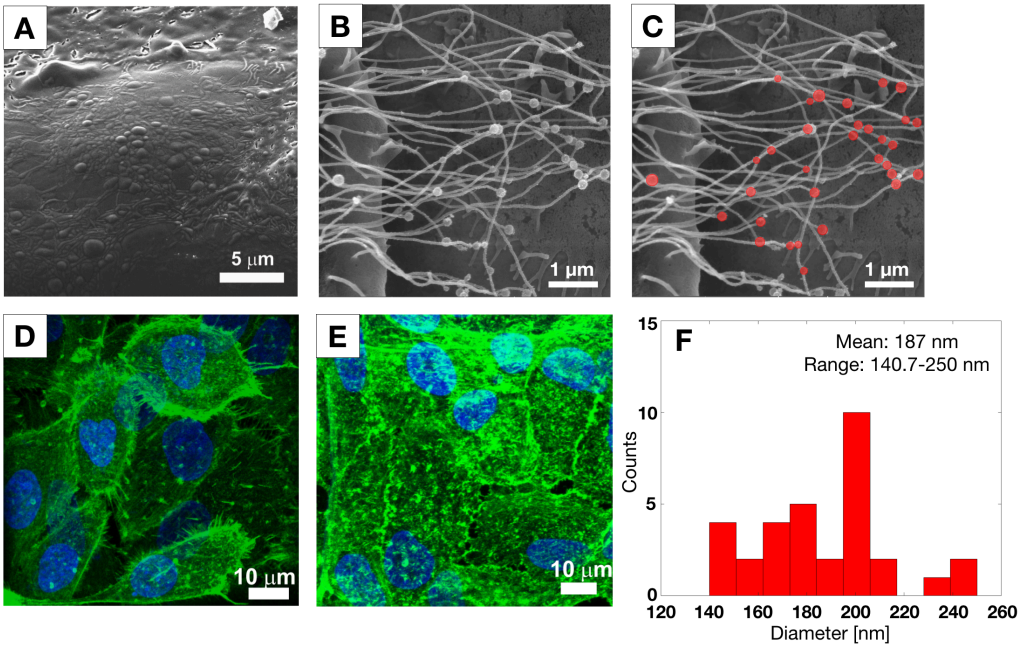

Fig. 3.3. Combining techniques provides insight into differences in cell morphology. Cryo-SEM shows rounded surface features protruding from the plasma membrane of MCF10A cells (A). Confocal microscopy shows a high intensity of actin expression in HAS3-10A (E) relative to the MCF10A control (D). This high actin expression is attributed to the presence of long, numerous tubular extensions from HAS3-MCF10A cells (Fig. 3.3B,C). Extensions in HAS3-MCF10A cells contain pearled structures along their lengths (C). These structures, highlighted in red in (C), are dimensionally consistent with MVs (F). *MCF10A cells: 3.3A,D; HAS3 cells: 3.3B-C, E-F*.

distribution is around 75, but a sufficient fraction of vesicles are also observed at larger sizes (Fig.3.5B).

Larger MVs comprised a greater proportion of vesicles in the cryo-TEM data, resulting in a broader tail in the size distribution (Fig. 3.5B). Vesicles less than 100 nm accounted for 45% of all vesicles tracked by NTA, but only 32% of vesicles detected with cryo-TEM. The NTA diameter distribution is artificially truncated due to the detectable diameter range of the instrument. Brownian motion limits the maximum size of detectable particles. As vesicles become too large, their Brownian motion becomes difficult to track over reasonable acquisition times. The software either fails to detect these particles or measures them with high inaccuracy (Yang et al, 2014). The upper range of accurately detectable particles is ~1000 nm, and particles larger than this are usually excluded from analysis. Cryo-TEM does not exclude vesicles with larger diameters, but confirms that the proportion of HAS3-secreted vesicles greater than 1000 nm is negligible. For instance, the largest particles tracked by NTA in this study were 997.5-1000 nm in diameter and comprised only 3% of all vesicles analyzed. Similarly, vesicles larger than 1000 nm accounted for only 4% of all vesicles observed with cryo-TEM.

The origin of the discrepancies between the NTA and cryo-TEM data could be attributed to several factors, necessitating the need to complement the techniques when possible. The cryo-TEM size distribution exhibits a lower SNR due to lower sample statistics. Despite the low-throughput nature of the technique, we believe the number of vesicles collected by cryo-TEM (n = 642) was sufficiently high to use as a comparison to NTA data. However, a larger dataset would undoubtedly provide a more refined result. Debris in the cell media likely influences the distribution of particle diameters in the NTA data. Post-NTA cell media examined with cryo-TEM shows the presence of a large amount of debris of varying sizes (Fig. 3.6). NTA tracks any material that diffuses and has a refractive index (Filipe et al., 2010). The software assumes that the particles are spherical and derives a hydrodynamic diameter for both vesicular and non-vesicular material. This means that in NTA it is difficult to reliably

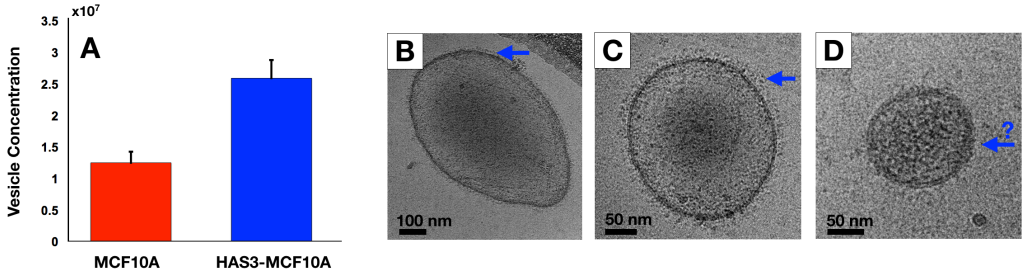

Fig. 3.4. EV secretion and morphology. MCF10A cells secrete less vesicles than HAS3-MCF10A cells (A). Vesicles secreted from HAS3-MCF10A cells do not have the characteristic cup-shaped structure when preserved in its native state and imaged with cryo-TEM (B-D). Vesicles are heterogeneous in size and shape (B-D). Additionally, the larger HAS3-MCF10A vesicles have prominent surface structure (B-C, blue arrows), while smaller vesicles have either less or no such surface structure (D, blue arrows). *Figure A scale bars represent SEM.*

differentiate between vesicles and debris within a solution, and the diameters of any particle that moves within the solution is recorded. This could explain the difference in the relative proportions of smaller to larger vesicles in the NTA and cryo-TEM data. Superficially, most of the post-NTA debris appears larger than the sizes of exosomes, but the debris appears to contain aggregates of smaller structures that are about the size of exosomes (Fig. 3.6). These structures could have aggregated after NTA and before vitrification. Because NTA cannot differentiate between vesicles and contaminants, dissociated debris could have been tracked as vesicles by NTA and recorded accordingly.

The choice of whether to use NTA or cryo-TEM to profile secreted EVs depends on the question under examination. NTA is the more suitable technique when one wants to compare the relative concentrations of vesicles secreted by different cell lines. NTA

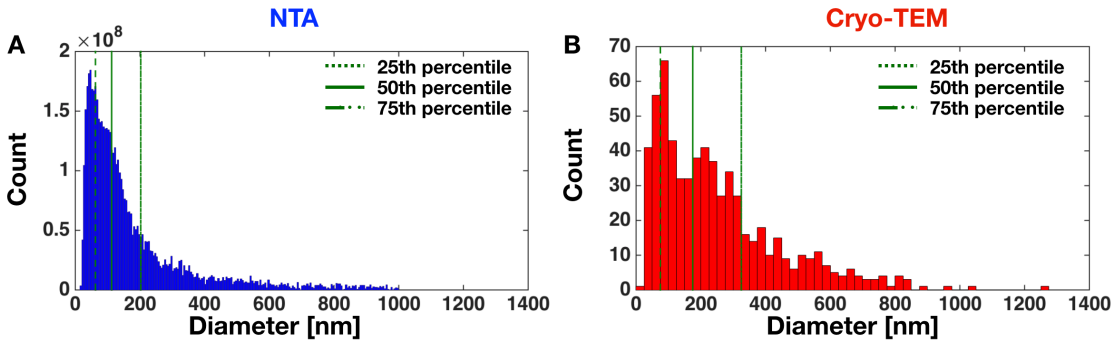

Fig. 3.5. HAS3-MCF10A vesicle size distribution measured by NTA and cryo-TEM. The size distribution of vesicles tracked with NTA (A) is noticeably different than the distribution of vesicles observed with cryo-TEM (B). Most notably, larger vesicles comprise a greater proportion of vesicles captured by cryo-TEM than NTA. The percentiles of vesicle sizes are denoted by green lines in each figure.

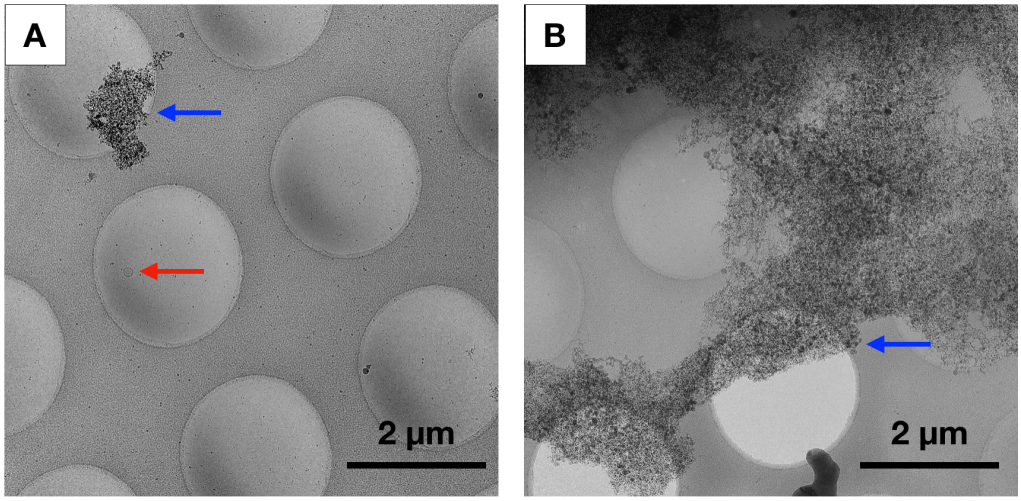

Fig. 3.6. Presence of debris in HAS3-MCF10A cell media. Cell media contained both vesicles (A, red arrow) and debris (A,B, blue arrows). Debris varied in size (A,B). There is also the possibility that the debri imaged in cryo-TEM were once smaller particles that aggregated after NTA analysis.

is also useful when high-throughput information of a high concentration of vesicles is desired. Finally, NTA is useful when the majority of particles are less than 1000 nm in diameter, especially in polydisperse samples. Cryo-TEM is the more useful technique when imaging either very small or very large populations of vesicles, particularly those near the detection range of NTA instruments. Cryo-TEM can visualize surface morphology, making it the method of choice for distinguishing between subpopulations of vesicles. Finally, cryo-TEM is more useful when examining media that is contaminated with other non-vesicular components, such as those produced during the isolation process. However, combining the techniques can help experimentalists understand the effect of protein upregulation on EV shedding, size and morphology in a way that the techniques could not do individually.

3.6 Conclusions

This study compared the use of confocal microscopy, RT-SEM, and cryo-SEM in analyzing cell morphology and the formation of EVs from human cell lines. Additionally, we used NTA and cryo-TEM to characterize secreted EVs. Our results highlight that there is no workhorse technology that can provide a comprehensive analysis of cell morphology, EV biogenesis, and EV secretion. However, the limitations of one technique can be compensated by the merits of additional techniques. SEM captures 3D projections from the cell surface, but the cells are desiccated during the sample preparation process. Cryo-SEM preserves the water content of these cells, but can affect the structure of projecting features. Composite data from the two techniques reveals that 10A and HAS3-10A cells are rounded, adherent cells with 3D tubular extensions. Similarly, NTA provides a general idea of the distributions of vesicles in a given suspension, but cryo-TEM can differentiate between vesicles and debris, as well as probe vesicle morphology. Together, the two techniques reveal both the relative size distribution and concentration of MCF10A and HAS3-MCF10A cells and the morphology of secreted vesicles. Such information is bound to be useful in the future, when differentiating between exosome and microvesicle populations becomes of scientific interest. Our study reaffirms the necessity of a multiplatform approach for assessing vesicle-secreting parental cell lines.

3.7 Acknowledgements

The authors would like to thank Mick Thomas and John Grazul for microscopy support. We thank Brian Kirby, Siyoung Choi, Michael Zachman and Jennie A.M.R. Kunitake for helpful discussions. This work was supported by the National Institute of Health/National Cancer Institute (Grant U54 CA210184), and the Packard Foundation. This work made use of the Cornell Center for Materials Research Shared Facilities which are supported through the NSF MRSEC program (DMR-1719875).Cornell Nanoscale Science and Technology Facility supported through the NSF Grant (ECCS-1542081), Biotechnology Resource Center (BRC) Imaging Facility (NIH S10OD018516).

REFERENCES

1. Antonyak, M.A., Li, B., Boroughs, L.K., Johnson, J.L., Druso, J.E., Bryant, K.L., Holowka, D.A., Cerione, R.A., 2011. Cancer cell-derived microvesicles induce transformation by transferring tissue transglutaminase and fibronectin to recipient cells. Proc. Natl. Acad. Sci. 108, 4852–4857.

2. Becker, A., Thakur, B.K., Weiss, J.M., Kim, H.S., Peinado, H., Lyden, D., 2016. Extracellular vesicles in cancer: cell-to-cell mediators of metastasis. Cancer Cell 30, 836–848.

3. Charuvi, D., Nevo, R., Kaplan-Ashiri, I., Shimoni, E., Reich, Z., 2016. Studying the supramolecular organization of photosynthetic membranes within freeze-fractured leaf tissues by cryo-scanning electron microscopy. J. Vis. Exp.

4. Cochard, H., Bodet, C., Améglio, T., Cruiziat, P., 2000. Cryo-scanning electron microscopy observations of vessel content during transpiration in walnut petioles. Facts or artifacts? Plant Physiol. 124, 1191–202.

5. D'Souza-Schorey, C., Clancy, J.W., 2012. Tumor-derived microvesicles: shedding light on novel microenvironment modulators and prospective cancer biomarkers. Genes Dev. 26, 1287–99.

6. Desrochers, L.M., Bordeleau, F., Reinhart-King, C.A., Cerione, R.A., Antonyak, M.A., 2016. Microvesicles provide a mechanism for intercellular communication by embryonic stem cells during embryo implantation. Nat. Commun. 7, 11958.

7. Dubochet, J., McDowall, A.W., 1981. Vitrification of pure water for electron microscopy. J. Microsc. 124, 3–4.

8. Filipe, V., Hawe, A., Jiskoot, W., 2010. Critical evaluation of Nanoparticle Tracking Analysis (NTA) by NanoSight for the measurement of nanoparticles and protein aggregates. Pharm. Res. 27, 796–810.

9. Furie, B.C.B., Furie, B.C.B., 2004. Role of platelet P-selectin and microparticle PSGL-1 in thrombus formation. Trends Mol. Med. 10, 171–178.

10. György, B., Szabó, T.G., Pásztói, M., Pál, Z., Misják, P., Aradi, B., László, V., Pállinger, É., Pap, E., Kittel, Á., Nagy, G., Falus, A., Buzás, E.I., 2011. Membrane vesicles, current state-of-the-art: emerging role of extracellular vesicles. Cell. Mol. Life Sci. 68, 2667–2688.

11. Kim, C.W., Lee, H.M., Lee, T.H., Kang, C., Kleinman, H.K., Gho, Y.S., 2002.

Extracellular membrane vesicles from tumor cells promote angiogenesis via sphingomyelin. Cancer Res. 62, 6312–7.

12. Koifman, N., Biran, I., Aharon, A., Brenner, B., Talmon, Y., 2017. A direct-imaging cryo-EM study of shedding extracellular vesicles from leukemic monocytes. J. Struct. Biol. 198, 177–185.

13. Koistinen, V., Kärnä, R., Koistinen, A., Arjonen, A., Tammi, M., Rilla, K., 2015. Cell protrusions induced by hyaluronan synthase 3 (HAS3) resemble mesothelial microvilli and share cytoskeletal features of filopodia. Exp. Cell Res. 337, 179–191.

14. Le, M.T.N., Hamar, P., Guo, C., Basar, E., Perdigão-Henriques, R., Balaj, L., Lieberman, J., 2014. miR-200–containing extracellular vesicles promote breast cancer cell metastasis 124, 5109–5128.

15. Liu, Y., Zhu, X., Zeng, C., Wu, P., Wang, H., Chen, Z., Li, Q., 2014. Microvesicles secreted from human multiple myeloma cells promote angiogenesis. Acta Pharmacol. Sin. 35, 230–238.

16. McCully, M.E., Canny, M.J., Huang, C.X., 2009. Cryo-scanning electron microscopy (CSEM) in the advancement of functional plant biology. Morphological and anatomical applications. Funct. Plant Biol. 36, 97.

17. Muralidharan-Chari, V., Clancy, J.W., Sedgwick, A., D'Souza-Schorey, C., 2010. Microvesicles: mediators of extracellular communication during cancer progression. J. Cell Sci. 123, 1603–1611.

18. Rilla, K., Pasonen-Seppänen, S., Deen, A.J., Koistinen, V.V.T., Wojciechowski, S., Oikari, S., Kärnä, R., Bart, G., Törrönen, K., Tammi, R.H., Tammi, M.I., 2013. Hyaluronan production enhances shedding of plasma membrane-derived microvesicles. Exp. Cell Res. 319, 2006–2018.

19. Soo, C.Y., Song, Y., Zheng, Y., Campbell, E.C., Riches, A.C., Gunn-Moore, F., Powis, S.J., 2012. Nanoparticle tracking analysis monitors microvesicle and exosome secretion from immune cells. Immunology 136, 192–7.

20. Tannetta, D., Dragovic, R., Alyahyaei, Z., Southcombe, J., 2014. Extracellular vesicles and reproduction–promotion of successful pregnancy. Cell. Mol. Immunol. 11, 548–563.

21. Utsumi, Y., Sano, Y., Fujikawa, S., Funada, R., Ohtani, J., 1998. Visualization of cavitated vessels in winter and refilled vessels in spring in diffuse-porous trees by cryo-scanning electron microscopy. Plant Physiol. 117, 1463–71.

22. van der Pol, E., Boing, A.N., Harrison, P., Sturk, A., Nieuwland, R., 2012. Classification, functions, and clinical relevance of extracellular vesicles. Pharmacol. Rev. 64, 676–705.

23. van Niel, G., D'Angelo, G., Raposo, G., 2018. Shedding light on the cell biology of extracellular vesicles. Nat. Rev. Mol. Cell Biol. 19, 213–228.

24. Yang, D.T., Lu, X., Fan, Y., Murphy, R.M., 2014. Evaluation of Nanoparticle Tracking for Characterization of Fibrillar Protein Aggregates. AIChE J. 60, 1236–1244.

25. Yuana, Y., Sturk, A., Nieuwland, R., 2013. Extracellular vesicles in physiological and pathological conditions. Blood Rev. 27, 31–39.

CHAPTER 4

CONNECTIVITY OF CENTERMOST CHROMATOPHORES IN *RHODOBACTER SPHAEROIDES* BACTERIA

4.1 Summary

The size of whole *Rhodobacter sphaeroides* has prevented 3D visualization of centermost chromatophores in their native environment. This study combines cryo-focused ion beam milling with cryo-electron tomography to probe vesicle architecture both *in situ* and in 3D. Developing chromatophores are membrane-bound buds that remain in topological continuity with the cytoplasmic membrane and detach into vesicles when mature. Mature chromatophores closest to the cell wall are typically isolated vesicles, whereas centermost chromatophores are either linked to neighboring chromatophores or contain smaller, budding structures. Isolated chromatophores comprised a minority of centermost chromatophores. Connections between vesicles in growing bacteria are through ~10 nm-long, ~5 nm-wide linkers, and are thus physical rather than functional in terms of converting photons to ATP. In cells from the stationary phase, chromatophores fuse with neighboring vesicles, lose their spherical structure and greatly increase in volume. The fusion and morphological changes seen in older bacteria are likely a consequence of the aging process, and are not representative of connectivity in healthy *Rba.sphaeroides*. Our results suggest that chromatophores can adopt either isolated or connected morphologies within a single bacterium. Revealing the organization of chromatophore vesicles throughout the cell is

an important step in understanding the photosynthetic mechanisms in *Rba. sphaeroides*.

4.2 Introduction

Photosynthesis by plants, algae, and photosynthetic bacteria is a significant source of the global energy supply. Among phototrophic organisms, *Rba. sphaeroides* is a purple bacterium widely explored as a model organism for anoxygenic photosynthesis via intracytoplasmic membrane vesicles called chromatophores. Each chromatophore is capable of photosynthesis by absorbing sunlight through an electronic excitation and converting it into chemical energy in form of ATP (Verméglio and Joliot, 1999; Hu *et al.*, 2002). Both the diverse metabolic strategies and the genes encoding the photosynthetic machinery in *Rba. sphaeroides* are well described, and recent interest in the bacterium lies in its promising potential in biorenewable technologies (Yilmaz *et al.*, 2010; Mahmoudzadeh *et al.*, 2011; Harris *et al.*, 2013; Yaghoubi *et al.*, 2014). Previous experimental and computational approaches prioritized providing a molecular-scale description of the architecture on a chromatophore surface and its light-harvesting mechanisms (Bahatyrova *et al.*, 2004; Geyer and Helms, 2006; Sener *et al.*, 2007; Olsen *et al.*, 2008; Cartron *et al.*, 2014; Sener *et al.*, 2016). Despite significant advances in understanding how proteins interact on the surface of a single vesicle, comparatively little research has focused on understanding how and to what extent chromatophores in *Rba. sphaeroides* interact with each other. As the reticulated nature of chromatophores may have a significant impact on the photosynthetic underpinnings in *Rba. sphaeroides* and biorenewable technologies, it is imperative to

investigate the extent of connectivity between vesicles throughout the bacterium both *in situ* and in 3D.

Decades of experimental effort have offered two models concerning chromatophore continuity in *Rba. sphaeroides.* The continuous model asserts that chromatophores in photosynthetic bacteria form a membrane continuum with both the cytoplasmic membrane (CM) and neighboring vesicles (Cohen-Bazire and Kunisawa, 1963; Boatman, 1964; Holt and Marr, 1965; Tauschel and Drews, 1967; Prince *et al.*, 1975; Holmqvist, 1979; Scheuring *et al.*, 2014; Verméglio *et al.*, 2016). However, there is also ultrastructural evidence to support the claim that chromatophores in phototrophic bacteria manifest as naturally discrete structures in the cytoplasmic space (Vatter and Wolfe, 1958; Geyer and Helms, 2006a; Tucker *et al.*, 2010). This is the discontinuity model. The discontinuity model has been significant to recent computational approaches, as most molecular modeling and simulation experiments of *Rba. sphaeroides* use an isolated vesicle as a template (Geyer and Helms, 2006; Sener *et al.*, 2007; Stone *et al.*, 2015; Sener *et al.*, 2016).

Investigating chromatophore connectivity in *Rba. sphaeroides* has been hampered by the limitations of experimental techniques used to assess their structure. Many reported results are based on *ex-situ* studies or on the interpretation of projection images, which can alter native structures or discard important 3D information about vesicle connectivity (Cohen-Bazire and Kunisawa, 1963; Boatman, 1964; Holt and Marr, 1965; Tauschel and Drews, 1967; Prince *et al.*, 1975; Holmqvist, 1979; Scheuring *et al.*, 2014; Verméglio *et al.*, 2016). Electron tomography (ET) provides

3D visualization of peripheral architecture in whole *Rba. sphaeroides* bacteria with nanoscale detail, however, resolving centermost structures is limited by cell thickness (Tucker *et al.*, 2010; Scheuring *et al.*, 2014). Cryo-ultramicrotomy is the conventional thinning technique, but it can introduce knife marks, crevasses and compression artifacts, especially for sections thicker than 100 nm (Al-Amoudi *et al.*, 2005; Han *et al.*, 2008; Pierson *et al.*, 2011). Most of these experimental limitations can be avoided by combining cryo-focused ion beam milling (cryo-FIB) with cryo-electron tomography (cryo-ET). Sample fixation by vitrification preserves the sample in a near-native, hydrated state, avoiding artifacts associated with the chemical fixation, dehydration and staining processes (Dubochet *et al.*, 1988). Cryo-FIB milling thins a specimen with a collimated beam of Ga^{+} ions, providing site-specific, ultra-thin sections without the artifacts associated with cryo-ultramicrotomy (Richter, 1994; Al-Amoudi *et al.*, 2005; Marko *et al.*, 2006; Rigort and Plitzko, 2015). Furthermore, thinning of frozen-hydrated prokaryotic cells or isolated eukaryotic cells can be performed directly on the TEM grid where specimens have been previously vitrified (Rigort, Bäuerlein, *et al.*, 2012). Cryo-FIB is a robust technique that has been used with cryo-ET to visualize both prokaryotic bacteria and photosynthetic organelles in 3D (Marko *et al.*, 2006; Engel *et al.*, 2015).

In this study, we use an on-grid cryo-FIB preparation of fully-hydrated *Rba. sphaeroides* to gain an *in-situ* view of the internal structure of the bacteria in their native state. We describe the 3D macromolecular landscape of *Rba. sphaeroides* both near the cell wall and deeper within the cytoplasm, including vesicle biogenesis, development, organization, and connectivity. This study provides an assessment of the

diversity of chromatophore architecture that was inaccessible using previous experimental techniques, as well as the biophysical motivation for connectivity between vesicles.

4.3 Results/Discussion

4.3.1 Cryo-focused ion beam milling reveals entire cytoplasmic space of R. sphaeroides bacteria

Cryo-electron microscopy (cryo-EM) and cryo-ET of whole, vitrified *Rba. sphaeroides* reveal the substructure of electron-transparent regions. However, a single cryo-EM projection image is limited by sample thickness, and therefore preferentially provides information about the areas closest to the membranes. A tomographic slice of a representative whole vitrified bacterium is presented in Fig. 1A. Clearly distinguishable structures are indicated by the green line and include the CM, the cell wall (CW), i.e., the outer membrane (OM) and the peptidoglycan (PG) layer, the periplasmic space (PS), and the photosynthetic apparatus or chromatophore (PSA) closest to the membranes. Vesicles towards the bacterial center are gradually less visible as a function of distance from the CW due to the bacteria's thickness, indicated by the yellow and red lines in Fig. 1A. High-resolution imaging of the interior structure of whole *Rba. sphaeroides* bacteria is challenging since the specimen thickness is greater than the inelastic mean free path of electrons in the specimen, about ~350 nm for a 300 kV source (Grimm *et al.*, 1996b). Electrons incident on a thick sample undergo multiple inelastic scattering events through the specimen volume, resulting in loss of coherence and compromised resolution in these regions.

Inelastically scattered electrons can be removed using an energy filter, however, the usable electron dose is reduced in the process. Consequently, features in the central regions of *Rba. sphaeroides* which fall below the detection limit—such as chromatophore vesicles—are unresolved, making statistical analysis of their organization challenging.

To access internal structure, cryo-FIB milling was performed on whole *Rba. sphaeroides* cells (Fig. 2). Each thinned lamella contained several specimens, which allowed us to record multiple tomograms on a single lamella. Thinned samples were typically ~300 nm thick and were sufficiently thin for analysis in the TEM, but sufficiently thick to probe the extent of connectivity between several chromatophores (diameters 50-70 nm) in 3D space. A total of 1031 vesicles obtained from 10 tomograms of thinned specimen were used for analysis.

Cryo-ET revealed a crowded intracellular landscape of diverse structures encompassing several length scales. A tomographic slice of a thinned bacterium and its corresponding 3D segmentation are presented in Fig. 2A-B. Energy storage polymers, such as polyhydroxybutyric acid and polyphosphates, often accumulate in bacteria in granules called inclusion bodies. Inclusion bodies are identified by their localization to the bacterium's center, comparatively large (>100 nm) size and higher electron density. The numerous, high-intensity, macromolecules distributed throughout the cytoplasm have an average diameter of ~20 nm and are dimensionally

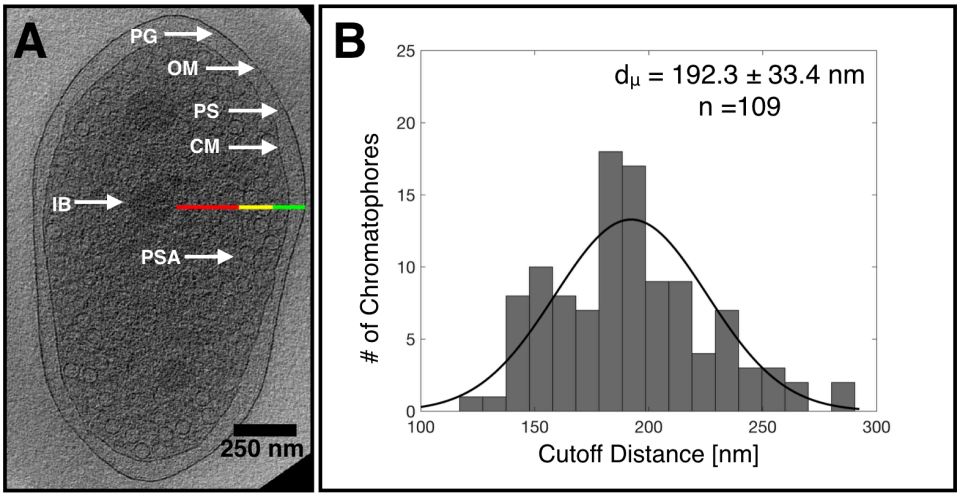

Fig. 4.1. Thickness-dependent cutoff distances for identification and characterization of chromatophores in whole *R. sphaeroides*. A tomographic orthoslice of whole *R. sphaeroides* shows that cellular structure closer to the cell wall is clearly resolved with cryo-EM. Resolved structures include the outer membrane (OM), peptidoglycan layer (PG), periplasmic space (PS), cytoplasmic membrane (CM), photosynthetic apparatus (chromatophore, PSA), and inclusion bodies (IB) (A). The multicolored line indicates regions where PSAs are clearly visible (green), somewhat visible (yellow), and difficult to resolve (red) based on the characterization cutoff distance. Similar measurements (n = 109) were taken on other bacteria (N = 8), and a histogram of the cutoff distance measurements with the mean and standard deviation is shown in B. The average of these measurements is the characteristic cutoff distance used to determine the efficacy of cryo-FIB thinning for imaging PSAs in *R. sphaeroides*.

consistent with prokaryotic ribosomes (for additional visualization of ribosomes, see Fig. 7A). Mature chromatophores are found throughout the cytoplasm, are approximately spherical, and have a tightly distributed diameter of 57.7 ± 2.5 nm (Fig. 2A-B, Fig. 6A).

Because the entire cytoplasm of the bacterial lamella is revealed in 3D, the number of chromatophores in a whole *Rba. sphaeroides* bacterium can be reasonably estimated. We approximate the whole bacterium as a prolate spheroid with short axes lengths of

~900 nm and a long axis length of ~1700 nm as estimated from the tomographic reconstruction of the FIB lamella in Fig. 2. The ~270 nm thick lamella contained 306 chromatophores. Comparing volumes, the whole bacterium should have about 700 chromatophores.

Visual comparison of tomographic slices from the whole bacterium in Fig. 1A and the thinned bacterium in Fig. 2A demonstrates that access to many centermost chromatophores—and hence the scope of this experiment—would be limited due to sample thickness using traditional approaches. To estimate the amount of cytoplasmic content that would have been lost in Fig. 2A had the bacterium not been thinned, we analyzed projection slices and orthoslices of whole *Rba. sphaeroides* (N = 7 whole bacteria, including the bacterium in Fig. 1A) and measured the distance from the outer membrane at which chromatophore vesicles became inaccessible or difficult to resolve. The average of these measurements (n = 109) was deemed the characterization cutoff distance (Fig. 1B). The characteristic cutoff distance is a robust measurement for bacteria of comparable sizes, such as those in this study. However, natural thickness variations would affect the fraction of vesicles that are visible without sample thinning. These variations are accounted for by the standard deviations of the cutoff distances.

The mean and standard deviation of the cutoff distances from Fig. 1B were used to analyze the improvement of accessibility of the cytoplasmic space due to cryo-FIB milling in the thinned bacterium in Fig. 2A. The results are summarized in Fig. 2C-D.

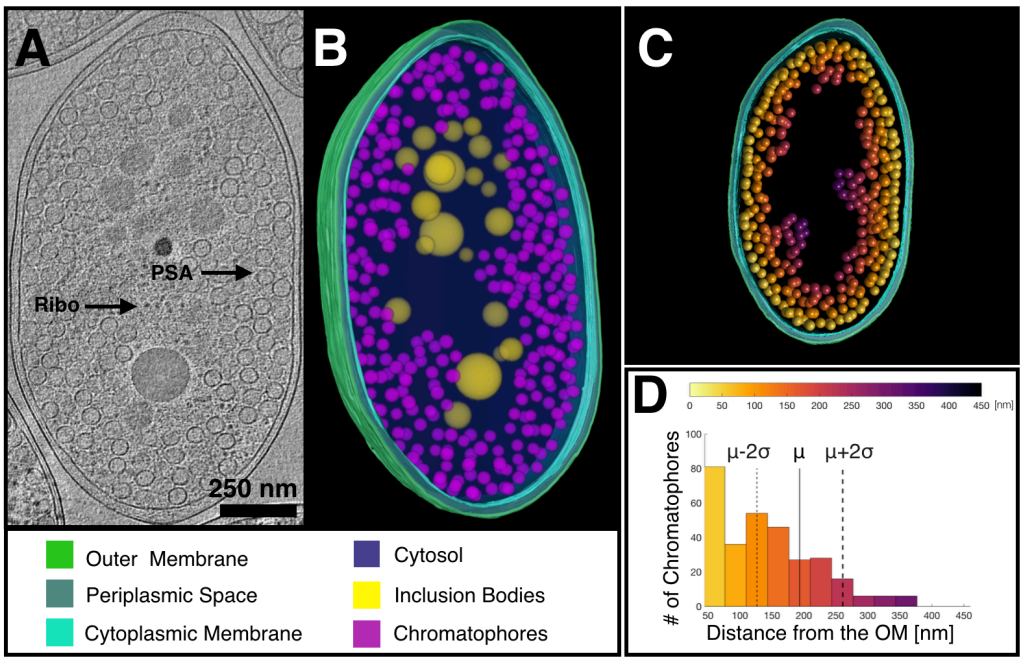

Fig. 4.2. Efficacy of the cryo-FIB process. A tomographic orthoslice (A) and its corresponding segmentation (B) of an *R. sphaeroides* bacterium thinned by cryo-FIB. Features such as ribosomes (ribo), which could not be elucidated in whole bacteria are visualized in sectioned specimen (A). The chromatophores from 2A-B were mapped to a color map, where the coloration is a function of the vesicles' distances from the nearest point on the OM in nm (C). (D) Histogram of those distances with the same color map applied. The mean of the cutoff distances from 2B is represented by μ and a solid line, and two standard deviations from the mean are represented by a dotted line (μ-2σ) and a dashed line (μ+2σ). Chromatophores closer than -2σ from the mean do not require thinning for visualization. Chromatophores beyond this distance are gradually inaccessible in unthinned bacteria. Features -1σ to +1σ from the mean may or may not be accessible without thinning, depending on the natural thickness of the whole bacterium. Features greater than μ+2σ from the OM are difficult to resolve without sample thinning.

In the histogram of the number of chromatophores as a function of distance from the OM (Fig. 2D), vesicles that would be difficult to visualize without cryo-FIB are indicated by the characterization cutoff distance mean (*solid line*) and ± two standard deviations from the mean (*dashed lines*). Features closer than -2σ from the mean can easily be resolved, while features beyond -2σ are increasingly unlikely to be seen. All

inclusion bodies (n = 22) lie beyond the cutoff distance from the OM. They are visible in whole *Rba. sphaeroides* only because of their large size and electron density, but resolution is compromised. Most ribosomes also lie beyond the cutoff distance, and due to their smaller dimensions, would be unresolvable in whole bacteria. 152 (49.7%) of the chromatophores in Fig. 2A are closer than -2σ from the mean, and the remaining 154 (50.3%), of the chromatophores in the bacterium become increasingly inaccessible. The bacterium in Fig. 2A lacks centermost chromatophores. For bacteria with more central chromatophores, such as those seen in Fig. 7, the percentage of occluded chromatophores would be greater.

4.3.2 Vesicular architecture on bacterial peripheries reveals isolated chromatophores and vesicles budding from the CM

Chromatophores in *Rba. sphaeroides* originate from single budding events on the CM (Oelze and Drews, 1972). Tomographic orthoslices and segmentations from thinned *Rba. sphaeroides* capture a montage of the intermediate developmental stages of vesicular biogenesis, which are characterized by different morphologies (Fig. 3A-B). In the earliest nascent stages, chromatophores appear as small indentations in the CM as discussed in previous work (Tucker *et al.*, 2010). During the early budding stage, these indentations develop into irregularly shaped invaginations of the CM. Invaginated membranes remain continuous with the CM and have access to the periplasmic space through an opening at their bases (Fig. 3A). Late budding chromatophores adopt an approximately spherical configuration and minimize their continuity with the CM by forming a "neck" from which they will bud (Fig. 3B). In

the pre-detachment stage, the neck disappears, but the chromatophore remains contiguous with the CM by a point of contact of minimized surface area (Fig. 3A). Once detached from the CM, the vesicle is liberated into the cytoplasm as a membrane-bound, differentiated structure that is released into the cytoplasm (Fig. 3B).

Vesicle biogenesis from the CM has been observed in previous research (Tucker *et al.*, 2010) with comparatively more budding vesicles. Our electron microscopy data captured very few budding events (n = 6; 0.6% of all chromatophores examined) and, therefore, no further analysis on these early stages of development were performed. Biogenesis events are more prevalent in developing bacteria or bacteria that have been recently exposed to the proper light or anoxygenic conditions. The bacteria cultured in this study were likely nearly or fully developed, decreasing the likelihood of seeing biogenic events along the CM. The more prevalent structures were mature chromatophores that remained in close proximity to the membranes (Fig. 3B). These chromatophores were largely isolated from neighboring vesicles. Peripheral chromatophores are physically connected to the CM for the duration of their morphogenesis, but form independent structures once separated from the CM.

4.3.3 Centermost structure in R. sphaeroides

Conflicting observations of connectivity between chromatophores in *Rba. sphaeroides* is in part due to the inability to access the majority of the vesicles in the bacteria. The architecture of chromatophores far from the bacterial membranes has yet to be explored in depth. To provide a more complete description of vesicular architecture in

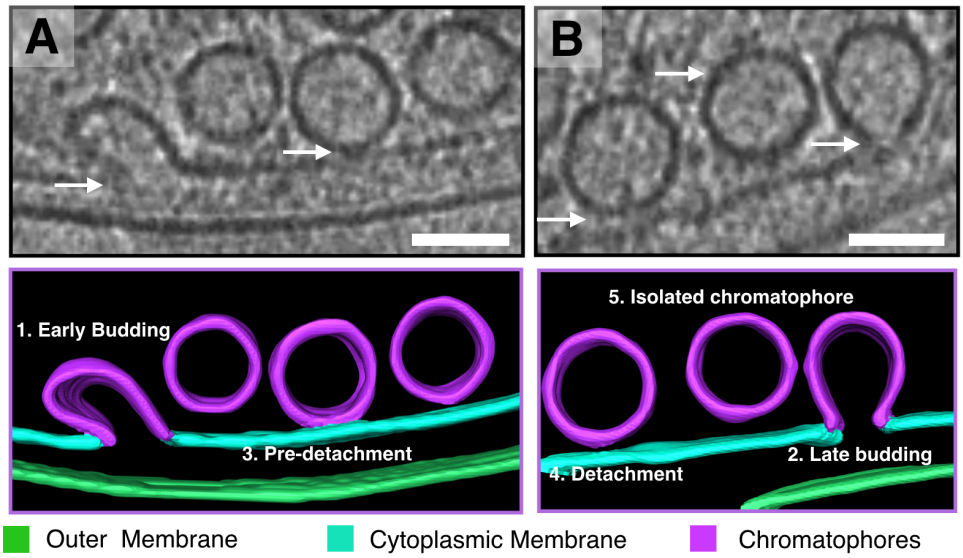

Fig. 4.3. Chromatophore structure at the bacterial peripheries. Tomographic orthoslices *(top row)* and their corresponding 3D segmentations (*bottom row*) capture the different stages of vesicle biogenesis from the cytoplasmic membrane: the (1) early budding, (2) late budding, (3) pre-detachment, and (4) detachment stages of developing chromatophores (white arrows). Although mature chromatophores eventually diffuse into the cytoplasm, recently detached chromatophores are closer to the cytoplasmic membrane than older chromatophores, and are more often isolated from proximate structures than centermost vesicles (5). *Scale bars: 50 nm*

Rba. sphaeroides, we capitalize on the ability to view centermost chromatophores and classify them based on their morphological differences. Each chromatophore is examined in 3D from the slice along the Z-axis where it emerges in the tomogram to the slice where it disappears. Chromatophores are designated as either "isolated" or "connected." Connected chromatophores are subcategorized based on their morphology as either "clustered" or "linked" chromatophores (Fig. 4 A-D). Statistical information on the morphologies of all chromatophores is presented in Fig. 6 A-C.

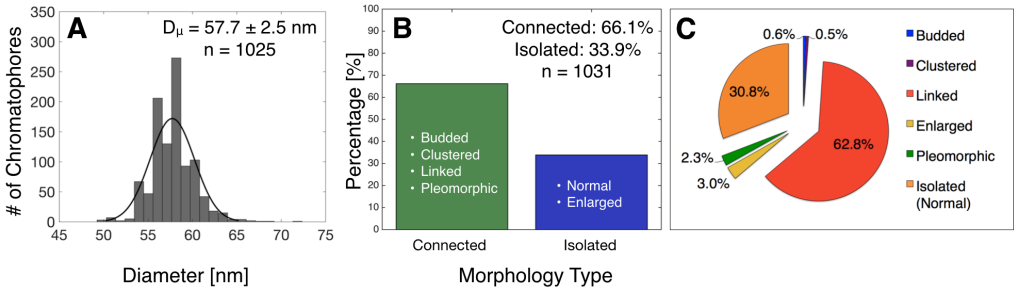

Fig. 4.4. Statistical representation of diverse morphologies of chromatophores in *R. sphaeroides*. Mature chromatophores in growing *R. sphaeroides* bacteria had a tightly distributed diameter of 57.7 ± 2.5 nm (mean, standard deviation), n = 1025 (A). The diameters of budded chromatophores (n = 6) are not included in this histogram because their irregular shape and small diameters are not representative of mature chromatophores. Chromatophores can display either connected (n = 682; 66.1%) or isolated (n = 349; 33.9%) morphologies. Connected morphologies include budded (n = 6; 0.6%), clustered (n = 5; 0.5%), linked (n = 647; 62.8%), and pleomorphic (n = 24, 2.3%) vesicles (B-C). Isolated chromatophores were of either normal (n = 318; 30.8%) or enlarged diameters (n = 31; 3.0%). The statistics in B and C include budded chromatophores, n = 1031.

Clustered vesicles: Clustered vesicles consist of two components: a mature chromatophore, and a smaller structure budding from the chromatophore's lipid bilayer membrane (Fig. 4B). The budded structures are distinguished from other connected structures by the presence of a neck. We designate these structures as "buds" because of their structural similarity to underdeveloped vesicles budding from the CM. The buds in clustered vesicles remain in topological continuity with the chromatophore via the neck, and have access to the chromatophore's interior through an opening at the base of the neck. The membranes of the budded structures are dimensionally and visually consistent with the chromatophore membrane, but could be either an extension of the chromatophore membrane or an independent structure. Each clustered vesicle unit contained one mature vesicle and one budded structure. Buds were approximately spherical, and smaller than their "host" vesicle.

The presence of clustered vesicles may challenge the idea that all vesicle biogenesis occurs from the CM. The prevailing thought is that vesicle initiation and budding in photosynthetic bacteria occur exclusively on the CM. However, there is evidence that vesicles in photosynthetic bacteria are formed both through the invagination of the CM and through budding on preexisting chromatophores (Niederman *et al.*, 1979; Tucker *et al.*, 2010). In chromatophore biogenesis from the CM, there is a mechanism that turns the CM into the specialized proteins on the chromatophore surface (Drews and Golecki, 1995). If budding were to occur from a mature chromatophore, similar differentiation mechanisms would have to exist.

Previous experiments on the biogenesis of chromatophores from *Rba. sphaeroides* demonstrated cell cycle-dependent changes in chromatophore biosynthesis (Yen et al., 1984; Kiley and Kaplan, 1988). Right before cell division, there is an increase in phospholipid production by the cell, which is incorporated into existing chromatophores just before the bacterium partitions into daughter cells. Both phospholipid production and incorporation into chromatophores are suspended at the initiation of cell division. Following cell division, proteins (such as the LH and RC complexes, among others), pigments, and other membrane constituents are incorporated into preexisting chromatophores after cell division. The incorporation of additional membrane constituents into existing chromatophores may explain the apparent presence of additional components—such as the budded structures.

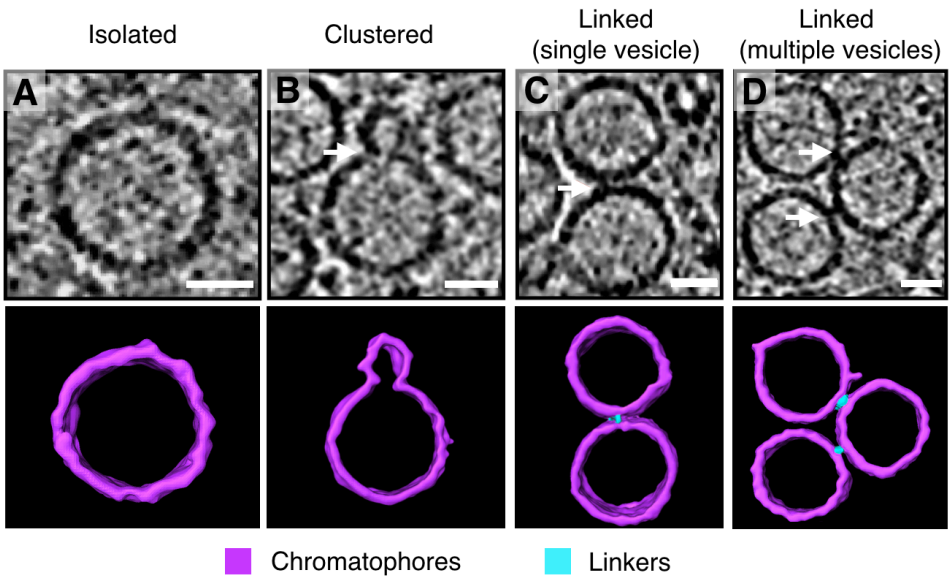

Fig. 4.5. Diversity of centermost vesicles. Centermost chromatophores can display either isolated (A) or connected (C-D) morphologies. Orthoslices (*top row*) and their corresponding segmentations (*bottom row*) are representative images of centermost chromatophore morphologies. Centermost chromatophores appear to be entirely isolated from neighboring structures (A), while clustered structures are denoted by the presence of a budded structure protruding from the surface of a mature chromatophore (B). Small linkers connect one (C) or more (D) neighboring vesicles to each other. White arrows are present to guide the reader to the budded structure (B) and linkers (C,D). *Scale bars = 25 nm*

Another explanation comes from data presented by Tucker and collaborators (see Tucker *et al.*, 2010). The authors describe the formation of a "double" vesicle structure consisting of two interconnected chromatophores. These twinned structures are a byproduct of a secondary budding event initiated at the CM. The double budded structures near the CM in Tucker's data are very similar in size to the clustered structures observed in our data, although our clustered structures were found exclusively in the centermost regions of the bacteria. The clustered vesicles do not appear to dissociate after detachment from the CM, and are likely separated only in case of cell disruption (Tucker *et al.*, 2010). Our data did not capture these budded

structures in later stages of development, so it is not possible to determine if they eventually detach to form independent chromatophores. Even if the buds separated into apparent vesicles, further experiments would be required to determine if the buds were indeed chromatophores, and if they are photosynthetically active. The evidence discussed so far supports the theory that the budded structures never fully develop and never dissociate.

Linked Vesicles: The majority of vesicles in the cytoplasm (n = 647, 62.8%) were connected to neighboring chromatophores via "linkers," or extensions of the chromatophore surface (Fig. 4C-D). These linkers were differentiated from noise or other electron-dense cytoplasmic material by examining their persistence through the tomogram in the Z direction. Whereas most features were present only in one or two consecutive slices, the linkers persisted over several slices and presented as cylindrical structures that aligned with the axis connecting the two vesicle centers and minimized the distance between them. Linkers were 8-10 nm long and 4-5 nm in diameter. Linkers were connected to the chromatophore surface, but did not appear to have access to the vesicle's interior. The linkers are visually and dimensionally consistent with the chromatophore lipid membrane and could be extrinsic extensions of the vesicle membrane. Linked chromatophores had one or two linkers, connecting vesicles in either pairs (Fig. 4C) or in multiples (Fig. 4D). Linked vesicles were almost exclusively localized to areas beyond the cutoff distance, closer to the bacterial center. In some instances, several linked chromatophores formed a network of vesicles that extended over several hundreds of nanometers into the cytoplasm. The network of

chromatophores in our data did not persist through the entire cytoplasmic volume. However, a fraction of connections may have been lost at the top and the bottom of the bacteria due to sample thinning, limiting the accessible range of potentially larger reticula.

Membrane continuity between photosynthetic organelles is common in other photosynthetic bacteria, such as *Rhodospirillum rubrum, Rhodopseudomonas palustris*, (Drews and Golecki, 1995), *Rba. capsulatus* (Oelze and Drews, 1972), and eukaryotic photosynthetic organelles such as chloroplasts (Shimoni *et al.*, 2005). In *Rba. sphaeroides* it was suggested that the bc_1 complexes localize to interconnecting regions between chromatophores and that a membrane continuum forms that extends throughout the entire cytoplasm (Scheuring *et al.*, 2014). Inspection of tomographic segmentations from (Scheuring *et al.*, 2014) show that these interconnecting regions are convex, tubular, and seem to connect chromatophores at a minimized distance from each other. Moreover, these interconnecting regions fused chromatophores into a continuous membrane, potentially providing a mechanism for the flow of constituents between vesicles.

In contrast, our data shows that the linked vesicles are discrete but connected structures, consisting of single vesicles attached to each other via an extrinsic component. Although chromatophores are physically connected, it is unlikely that energy transfer between vesicles occurs through these linkers. Förster resonance energy transfer (FRET) describes the energy transfer between two photosensitive

molecules, such as the pigment-protein complexes on a chromatophore's surface (Förster, 1946). The energy transfer between donor and acceptor molecules is inversely proportional to sixth power of the distance between the donor-acceptor pair, making FRET sharply distance-dependent (Förster, 1946; Förster, 1948; Şener *et al.*, 2011). Therefore, it is unlikely that energy transfer across a linker of ~10 nm would occur. Each vesicle within a linked cluster is also a closed compartment. Previous experimental and computational work has demonstrated that they act as autonomous photon-to-ATP converters (Cartron *et al.*, 2014; Sener *et al.*, 2016; Dahlberg *et al.*, 2017) despite any linked connections to neighboring vesicles. This fact is further supported by structural and functional models of individual vesicles, which have been shown to account for the energetics and physiology of the whole cell (Hitchcock *et al.*, 2017; Dahlberg *et al.*, 2017).

Isolated Vesicles: Some centermost chromatophores in *Rba. sphaeroides* do not appear to form connections with proximate cytoplasmic structures. Regularly-shaped, isolated chromatophores comprise 30.8% (n = 318) of all chromatophores examined and had a weak spatial dependence toward the membranes. In contrast to the reports supporting the discontinuous model of vesicle connectivity, isolated chromatophores were not the predominant structure in *Rba. sphaeroides*, especially among chromatophores beyond the cutoff distance. Some connections could have been overlooked due to the missing wedge effect, in which the finite tilt-range of the tomographic tilt series results in unsampled information in Fourier space. A single-axis tilt series acquired over a range of ± 60° samples only 67% of Fourier space

information (Lučić *et al.*, 2005). There is a possibility that the unsampled information could contain additional connections. Our ability to detect the presence of connections between apparently isolated vesicles may be enhanced by increasing the angular range of our tilt series, but only as far as would comply with limitations in instrumental design.

Alternatively, we can estimate the percentage of connected vesicles under the assumption that some fraction of connections has been missed due to the missing wedge. A lower bound for this estimate is the directly observed percentage of connected chromatophores. An estimate for the higher bound is provided by estimating the number of connections which are present but have been missed due to the missing wedge effect. The fraction of missed bonds may be estimated by:

$$\frac{n_{mw}}{n} = \frac{4\theta_0}{2\pi}$$

where n is the total number of bonds, n_{mw} is the number of bonds that have been missed due to missing wedge effects, and θ_0 is the missing wedge semi-angle (taken to be 30°). Here, we assume that the connections are well-resolved and identifiable when oriented outside of the missing wedge (i.e., when the connections are approximately perpendicular to the beam direction for some tilt-angle within the tilt series), but are not identifiable when oriented within the missing wedge, where resolution is degraded. We assume that the connections between isotropically-oriented chromatophores are

themselves isotropically-oriented. The total number of bonds is the sum of the observed and unobserved bonds, thus, we can instead express n_{mw} in terms of the observed number of bonds, n_{ob}, as:

$$n_{mw} = \frac{\theta_0}{\frac{\pi}{2}-\theta_0} n_{ob}$$

Because a single chromatophore may have multiple connections, a missed bond may connect to chromatophores with no observed connections or to chromatophores with other connections that have already been observed. Thus, it is necessary to make a further assumption about the distribution of missed connections among the chromatophores. Let $d = 2n_{mw}$ be the number of connection points between chromatophores and unobserved bonds lying inside the missing wedge. We make the simplifying assumption that an unobserved bond is equally likely to be connected to a chromatophore with or without an experimentally observed bond. Thus, letting N be the total number of chromatophores, letting N_{ob}^0 be the number of chromatophores with no observed connections, and letting d_0 be the number of missed connections attaching to apparently unconnected chromatophores, we assume

$$\frac{\delta_0}{\delta} = \frac{N_{ob}^0}{N}$$

Finally, the total number of unconnected chromatophores, accounting for the missing wedge, is $N_u^0 = N_{ob}^0 - \delta_0$. Substituting in for d_0 and dividing by N yields an estimate of

the fraction of unconnected chromatophores, f_u, in terms of the observed fraction of unconnected chromatophores, *f*:

$$f_u = \left(1 - \frac{2n_{mw}}{N}\right) f = \left(1 - \frac{\theta_0}{\frac{\pi}{2} - \theta_0} \frac{2n_{ob}}{N}\right) f$$

Setting the percentage of unconnected chromatophores seen in our data f to 33.9%, we estimate that the total percentage of isolated chromatophores f_u is about 22%, taking into account the missing wedge. Therefore, we estimate that up to 78% of the chromatophores in our data are connected.

The key assumptions in this approximation are that the orientations of the connections are isotropically distributed, that an unobserved bond is equally likely to be connected to a chromatophore with or without an observed bond, and that all connections within the missing wedge are not observed in the reconstruction. These are imperfect assumptions, as they do not include, e.g., spatial variations and steric hindrance between chromatophores, or the possibility of resolving some fraction of bonds oriented within the missing wedge. However, we believe this approach provides a reasonable first-order estimate of the appropriate correction to the number of connected chromatophores.

Our data provides new insight into the debate over chromatophore continuity. A bacterium with isolated chromatophores seems intuitive: if each chromatophore contains the requisite infrastructure to undergo photosynthesis, it is not apparent why

chromatophores would need to network with other cytoplasmic structures. Physiochemically, the discontinuous model is intuitive: chromatophores generate proton gradients across their membranes, which are coupled to ATP synthesis. This proticity would be easier to achieve if the vesicles were closed and discontinuous. This argument is supported by many reports, most of which present evidence of isolated chromatophores in the thinner, peripheral regions of whole *Rba. sphaeroides*, or those closest to the membranes. The fact that these chromatophores are the only ones that can be observed without thinning techniques may explain why many microscopy studies concluded that all chromatophores exist as discrete vesicles. The results presented here suggest that centermost chromatophores are predominantly connected, while chromatophores closest to the peripheries are isolated.

One should note that the number of vesicles in an *Rba. sphaeroides* cell can vary greatly with growth conditions. Adams and Hunter reported that chromatophore occupancy in *Rba. sphaeroides* varied from ~270 to ~1400 chromatophores/cell, depending on the light intensity used. Bacteria grown in low-light conditions could have over five times more chromatophores than those grown in a high-light intensity environment (Adams and Hunter, 2012). Our estimation of the number of chromatophores per cell is in agreement with cells cultured in moderately low intensity light conditions. The connectivity of vesicles may also vary as a function of light intensity. The linked vesicles present in our data (Fig. 4C-D) are not seen in the electron micrographs of cells cultured in high-light intensity conditions in other

reports (Adams and Hunter, Tucker et al). This suggests that the proportion of isolated chromatophores varies depending on the light conditions.

4.3.4 Other architectures in growing R. sphaeroides

Most chromatophores in growing *Rba. sphaeroides* were easily classified into one of the aforementioned categories. There were a few cases where chromatophores were difficult to categorize (Fig. 5). These architectures include enlarged vesicles and pleomorphic vesicles that did not display distinctly clustered or linked topologies. Enlarged chromatophores are vesicles with diameters greater than 62.7 nm, or two standard deviations greater than the mean diameter. Our data records a small percentage (n = 31, 3.0%) of chromatophores with diameters larger than 62.7 nm. The largest chromatophore, seen in Fig. 5A, was 72.1 nm in diameter, about 25% larger than an average chromatophore. Finally, some chromatophores (n = 24, 2.3%) formed unusual connected structures with neighboring matured and presumably malformed vesicles (Fig. 5B-C).

Cell breakage could disrupt chromatophores, but because this was an *in-situ* study of chromatophores in their near native environment, the observed structures are unlikely to have been created during the experiment. Instead, it is possible that some chromatophores in *Rba. sphaeroides* do not develop normally. Alternatively, it is possible that these chromatophores are deviant structures but are photosynthetically viable. Kinetics and energetics experiments would be required to confirm either

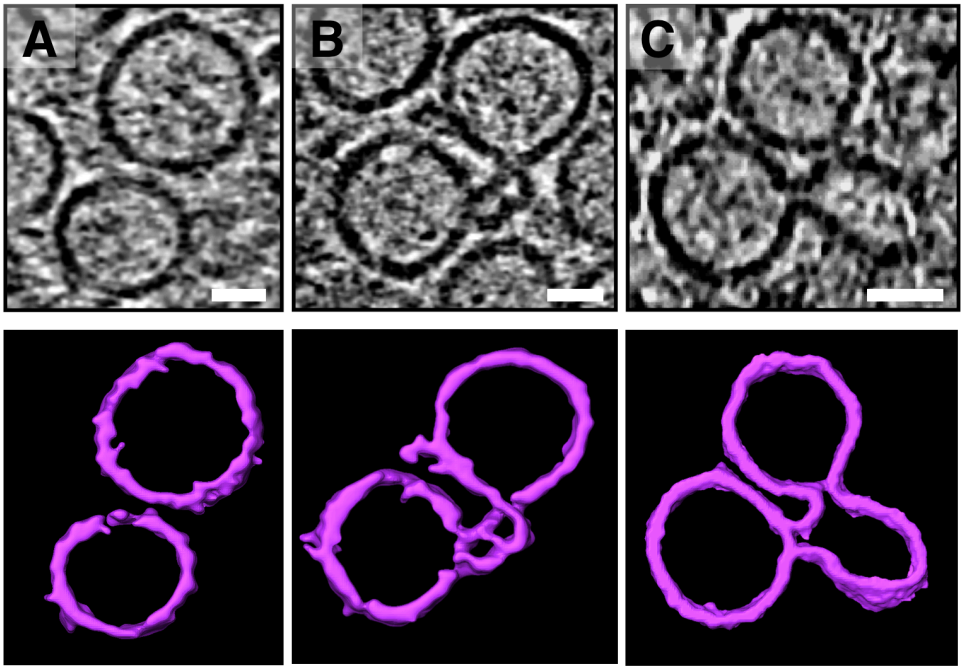

Fig. 4.6. Pleomorphic vesicular architectures. Some chromatophores could not be satisfactorily categorized as isolated, budded, or linked. Chromatophores that display pleomorphic architectures can be either isolated (A) or connected (B-C). Orthoslices (*top row*) and their corresponding segmentations (*bottom row*) display examples of chromatophores with pleomorphic morphologies. Some chromatophores were enlarged vesicles with diameters at least two standard deviations greater than the mean diameter. The top chromatophore in A has a diameter of 72.1 nm. A chromatophore of normal diameter (54 nm) is presented in the same image for comparison. Other chromatophores appeared connected with other vesicles in abnormal geometries. In some cases, mature chromatophores appeared to be connected by either tiny vesicles (B) or other membrane structures (C). These membrane structures can often be enlarged, appearing as deformed vesicles. *Scale bars: 25 nm.*

hypothesis. Although tuning growth conditions could affect the presence of the irregular structures, it is likely that, as with most biological systems, chromatophores in *Rba. sphaeroides* display some degree of structural variation.

4.3.5 Chromatophores in aged R. sphaeroides

Chromatophores in aged, i.e., stationary phase, bacteria are connected differently than those in growing cells (Fig. 7 A-B). Fig. 7 A shows a tomographic orthoslice and its corresponding segmentation in a representative, growth phase bacterium. Most of the bacterium's 87 chromatophores are approximately spherical with diameters (D_μ = 57.4 ± 1.8 nm; Fig. 7A, *right panel*) similar to the mean diameter of chromatophores in this experiment. Fig. 7B shows a tomographic orthoslice and its corresponding segmentation in a representative, aged bacterium. Although some chromatophores in the aged bacterium remain spherical with diameters similar to the chromatophores in healthy cells, most chromatophores undergo drastic structural changes as a consequence of the aging process. Most of the bacterium's 80 chromatophores were connected through fusion with one, often several neighboring vesicles with multiple points of attachment between them. The fused structures form a continuous membrane with sizes, as estimated by the average of the major and minor axes of the structure, much larger than a typical chromatophore in growing bacteria (D_μ = 94.1 ± 53.4 nm). Fused chromatophores lose their sphericity and rigidity, ultimately becoming irregular structures dispersed throughout the cytoplasm. The hallmark traits of connectivity between vesicles in growth phase bacteria, namely the presence of vesicles budding from the CM, clustered vesicles, and linked vesicles, were not present in stationary phase cells. Isolated vesicles were relatively infrequent in aged bacteria as well.

Many reports in support of the continuous model describe vesicle connectivity in *Rba. sphaeroides* as forming a membrane continuum by sharing large regions of their

surface areas with neighboring chromatophores. In our study, connectivity through fused vesicles was very rare in growing bacteria, but quite common in aged bacteria. From our data, it appears that spherical chromatophores fuse with neighboring vesicles before losing their rigidity and transforming into amorphous, enlarged structures. With a few exceptions, chromatophore fusion in the *Rba. sphaeroides* used in this study appears to be

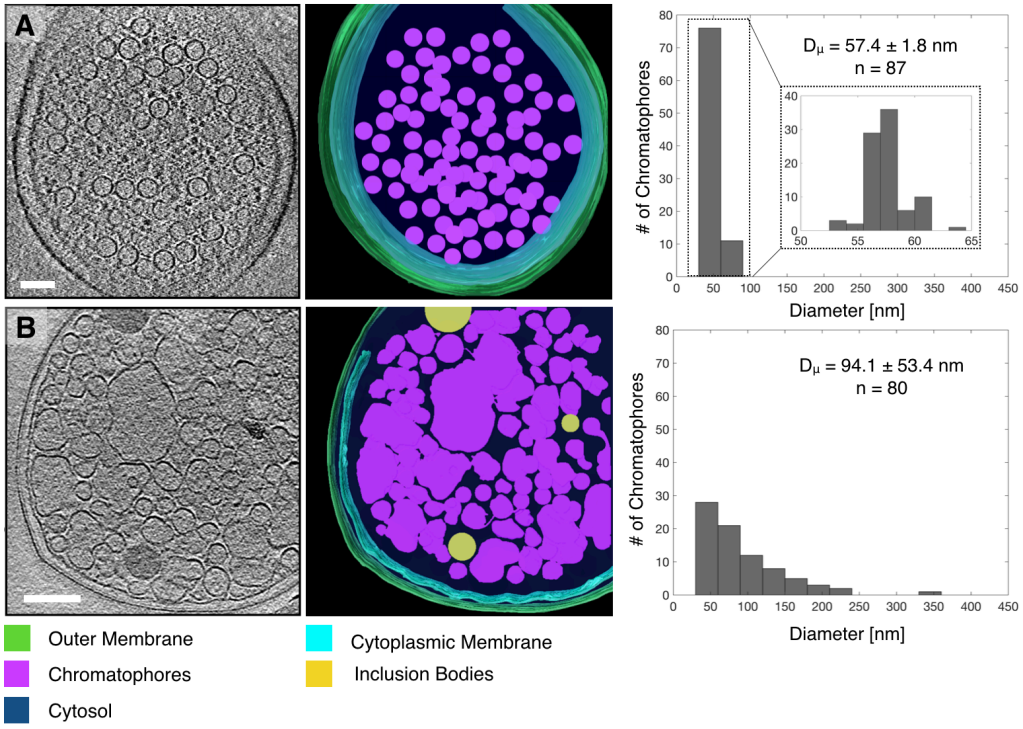

Fig. 4.7. Growing versus stationary phase bacteria. Orthographic slices (*lefmost column*) and corresponding segmentations (middle *column*) of representative cells in the growing (A) and stationary (B) phases show that the morphologies of chromatophores change with bacterial age. (A) Growing bacteria had approximately spherical chromatophores (PSA) with a tightly distributed diameter of 57.4 ± 1.8 nm (mean, standard deviation), n = 87. (B) Although some chromatophores in aged bacteria appear spherical and with normal diameters most chromatophores are irregularly-shaped, enlarged and have a large range of sizes (94.1± 53.4 nm; mean, standard deviation; n = 80). Degradation of chromatophores accompanies the loosening of the cytoplasmic membrane. *Scale bars: A: 100 nm, B: 250 nm.*

a consequence of the aging process and is concurrent with the increasing flexibility and degradation of the CM, and deterioration of the bacteria.

4.4 Conclusions

Cryo-EM of cells is often challenging due to specimen thickness. Many chromatophores in whole *Rba. sphaeroides* lie beyond a certain cutoff distance from the OM and are difficult to visualize without sample thinning. Thinning by cryo-FIB allowed access to the entire cytoplasm and cryo-ET revealed diversity in chromatophore architecture. Immature chromatophores remain in topological continuity with the cytoplasmic membrane and detach when mature. Recently detached chromatophores remain close to the cytoplasmic membrane and are largely discrete units. Centermost chromatophores in healthy bacteria can be either isolated or connected. Only about 22% of chromatophores in this study appeared isolated. Connected vesicles are either linked to one or more neighboring chromatophores or contain smaller, budding structures. Some chromatophores were either enlarged or displayed unusual morphologies. Further experiments are required to determine if connected vesicles, particularly the clustered and pleomorphic chromatophores, are photosynthetically active.

We also differentiate between chromatophores in growing and aged *Rba. sphaeroides*. Connections between vesicles in growth phase bacteria are limited to either linked or clustered morphologies. In aged cells, chromatophores fuse with several neighboring vesicles. The chromatophores in aged bacteria lose their rigidity, sphericity, and

greatly increase in volume. The structural changes seen in older bacteria are likely a consequence of the aging process, and are not representative of connectivity in healthy *Rba. sphaeroides*.

Our results address the question of connectivity between chromatophores in *Rba. sphaeroides*. The chromatophores in this study did not rigidly follow either the continuous or discontinuous models provided in previous research. Our study confirms that although some chromatophores are isolated, many more are connected to neighboring chromatophores. Furthermore, the diversity of chromatophore architecture in a single *Rba. sphaeroides* bacterium is remarkably complex for a prokaryotic cell, and each structure may have an implication on the bioenergetic processes of the cell. This information could lead to better fundamental understanding of photosynthesis in *Rba. sphaeroides* and aid in its incorporation into next-generation biorenewable energy devices.

4.5 Experimental Procedures

Cell culture: *Rba. sphaeroides* type strain (DSM 158) was used throughout this study. Liquid cultures were grown photoheterotrophically at 30°C in closed, filled 50 mL bottles placed under a halogen lamp (300-320 lux at the bottle surface). The growth medium containing malate and ammonium as C- and N-sources was based on the minimal medium of Ormerod *et al.* (1961) and supplemented with trace elements according to (Pfennig and Lippert, 1966). The optical density after a 3-day growth measured using a spectrophotometer at 600 nm (PerkinElmer, Inc. Waltham, MA)

against water was ~1.17. Cells from a 3-days culture, i.e. close to the end of the growth phase (indicated as growing cells), and from a 10-days culture, i.e. cells in the stationary phase (indicated as aged bacteria) were used for tomographic analyses. The cultures grew and remained under anaerobic conditions until preparation for electron microscopy. To increase the cell counts in preparation for cryo-FIB, 30 mL of cells in growth medium were centrifuged at 5,000 rpm for 10 minutes and 28.5 ml of the supernatant removed.

Plunge-freezing vitrification: 4 μL of bacterial cells in growth medium were pipetted onto holey carbon-coated 200 mesh copper grids (Quantifoil Micro Tools, Jena, Germany). R0.6/1 Quantifoil grids with hole sizes of ~0.5 μm were chosen to increase cell coverage. The grids were blotted from the reverse side and immediately plunged into a liquid ethane/propane mixture at liquid nitrogen temperature using a custom-built vitrification device (MPI, Martinsried, Germany). The plunge-frozen grids were stored in sealed cryo-boxes in liquid nitrogen until used.

Cryo-FIB: Plunge-frozen grids were mounted under liquid nitrogen into autogrids that were modified for FIB milling (Autogrid sample holder, FEI), providing stability to the EM grids during sample preparation and transfers. These autogrids were loaded into a dual-beam (FIB/SEM) microscope (Quanta 3D FEG, FEI) using a cryo-transfer system (PP3000T, Quorum) with a custom-built transfer shuttle. During FIB operation, samples were kept at a temperature of −180 °C using a custom-built rotatable cryostage (Rigort, Villa, *et al.*, 2012). Lamellas were prepared using a 30 kV

Ga+ ion beam at an angle of 8°–10° with respect to the grid plane. Rough milling was performed with rectangular patterns and 0.1 nA beam current, followed by lower beam current (50 pA) thinning and cleaning steps. To monitor the milling progress, the specimen was periodically imaged with the scanning electron beam operated at 10 kV and 50–90 pA.

Cryo-TEM and cryo-ET: A total of 10 thinned bacteria, 2 whole growth phase bacteria, and 2 whole stationary phase cells were selected for tomographic analysis. For whole bacteria, the characteristic cutoff length extracted from tomographic orthoslices was comparable to that from the 0º projection image. Further information about the cutoff length was, therefore, obtained from projection images from an additional 5 whole, growth phase bacteria. Cryo-TEM and cryo-ET were performed primarily on a Titan Krios operated at 300 kV (FEI, Eindhoven, Netherlands) equipped with a field-emission gun, and 4096 × 4096 FEI Falcon II direct detector camera. Data for Fig. 1(a) and Fig. 7(d) were recorded on an FEI Tecnai G2 Polara TEM equipped with a field emission gun operated at 300 kV, a GIF 2002 post-column energy filter (Gatan, Pleasanton, CA), and a 2048 × 2048 Gatan slow scan CCD camera. Single-axis tilt series were collected using the FEI tomography software with defocii between -8μm and -5μm and a total dose of 70-90 e/Å^2. Tilt series of both whole and thinned bacteria were acquired from -60° to 60° in 2-3° increments, for a total of 41-61 projection slices per tilt series. Images were binned by 2, or 4, resulting in pixel sizes of 0.92-1.26 nm.

Image processing and segmentation: Tilt series alignment and tomographic reconstructions were performed using the IMOD software package (http://bio3d.colorado.edu/imod/). Gold nanoparticles served as the alignment fiduciaries. In the absence of fiduciaries, tilt series alignment was performed with the patch tracking setting in IMOD. Final alignment of the tilt series images was performed using the linear interpolation method in IMOD. No CTF correction was performed. Tilt series were reconstructed by either weighted backprojection or SIRT (10 iterations) and denoised with 10-15 iterations of non-linear anisotropic diffusion using IMOD's NAD module (Frangakis and Hegerl, 2001). Thresholding and segmentation of tomography volumes for the representation of cellular components was performed with Avizo software (FEI). Chromatophores were manually segmented as circles at their maximum diameters along the Z-axis in Avizo and exported as 2D .tif files. The .tif files were imported into MATLAB for quantitative analysis. The *regionprops* function was used to determine the diameter and location of the circle's centroid. The distance of the segmentation's centroids from the CM was analyzed using a custom-made script. A custom-made script was used to replace the 2D segmentation of each chromatophore with a 3D sphere of the same diameter. The generated spheres were saved as binary files and reintroduced into Avizo for 3D visualization.

4.6 Acknowledgements

We thank Felix J. B. Bäuerlein, Marion Jasnin, Tim Laugks, Alexander Rigort, Elizabeth Villa for fruitful discussions and technical support. This work was supported

by the David and Lucile Packard Foundation, the Max Planck Society and a Humboldt Research Fellowship.

REFERENCES

1. Al-Amoudi, A., Studer, D., and Dubochet, J. (2005) Cutting artefacts and cutting process in vitreous sections for cryo-electron microscopy. *J Struct Biol* **150**: 109–121.

2. Bahatyrova, S., Frese, R.N., Siebert, C.A., Olsen, J.D., Werf, K.O. Van Der, Grondelle, R. Van, *et al.* (2004) The native architecture of a photosynthetic membrane. *Nature* **430**: 1058–1062.
3. Boatman, E.S. (1964) Observations on the fine structure of spheroplasts of *Rhodospirillum rubrum*. *J Cell Biol* **20**: 297–311.

4. Cartron, M.L., Olsen, J.D., Sener, M., Jackson, P.J., Brindley, A.A., Qian, P., *et al.* (2014) Integration of energy and electron transfer processes in the photosynthetic membrane of *Rhodobacter sphaeroides*. *Biochim Biophys Acta - Bioenerg* **1837**: 1769–1780.

5. Cohen-Bazire, G., and Kunisawa, R. (1963) The fine structure of *Rhodospirillum rubrum*. *J Cell Biol* **16**: 401–19.

6. Dahlberg, P.D., Ting, P.-C., Massey, S.C., Allodi, M.A., Martin, E.C., Hunter, C.N., and Engel, G.S. (2017) Mapping the ultrafast flow of harvested solar energy in living photosynthetic cells. *Nat Commun* **8**: 988.

7. Drews, G., and Golecki, J.R. (1995) Structure, molecular organization, and biosynthesis of membranes of purple bacteria. In *Anoxygenic Photosynthetic Bacteria*. Blankenship, R. E., Madigan, M.T., and Bauer, C.E. (eds). Kluwer Academic Publishers: Dordrecht. pp. 231–257.

8. Dubochet, J., Adrian, M., Chang, J.-J., Homo, J.-C., Lepault, J., McDowall, A.W., and Schultz, P. (1988) Cryo-electron microscopy of vitrified specimens. *Q Rev Biophys* **21**: 129-228.

9. Engel, B.D., Schaffer, M., Kuhn Cuellar, L., Villa, E., Plitzko, J.M., and Baumeister, W. (2015) Native architecture of the *Chlamydomonas* chloroplast revealed by in situ cryo-electron tomography. *Elife* **4**.

10. Förster, T. (1946) Energiewanderung und fluoreszenz. *Naturwissenschaften* **33**: 166–175.

11. Förster, T. (1948) Zwischenmolekulare energiewanderung und fluoreszenz. *Ann Phys* **437**: 55–75.

12. Frangakis, A.S., and Hegerl, R. (2001) Noise reduction in electron

tomographic reconstructions using nonlinear anisotropic diffusion. *J Struct Biol* **135**: 239–250.

13. Geyer, T., and Helms, V. (2006b) A spatial model of the chromatophore vesicles of *Rhodobacter sphaeroides* and the position of the cytochrome bc_1 complex. *Biophys J* **91**: 921–926.

14. Grimm, R., Typke, D., Bärmann, M., and Baumeister, W. (1996) Determination of the inelastic mean free path in ice by examination of tilted vesicles and automated most probable loss imaging. *Ultramicroscopy* **63**: 169–179.

15. Han, H.-M., Zuber, B., and Dubochet, J. (2008) Compression and crevasses in vitreous sections under different cutting conditions. *J Microsc* **230**: 167–171.

16. Harris, M.A., Parkes-Loach, P.S., Springer, J.W., Jiang, J., Martin, E.C., Qian, P., *et al.* (2013) Integration of multiple chromophores with native photosynthetic antennas to enhance solar energy capture and delivery. *Chem Sci* **4**: 3924-3933.

17. Hitchcock, A., Hunter, C.N., and Sener, M. (2017) Determination of cell doubling times from the return-on-investment time of photosynthetic vesicles based on atomic detail structural models. *J Phys Chem B* **121**: 3787–3797.

18. *Holmqvist, O. (1979) Evidence of discontinuity between the cytoplasmic and intracytoplasmic membranes in* Rhodopseudomonas sphaeroides*: A study with ferrous gluconate as a tracer substance in electron microscopy and X-ray microanalysis. FEMS Microbiol Lett* ***6****: 37–40.*

19. Holt, S.C., and Marr, A.G. (1965) Location of chlorophyll in *Rhodospirillum Rubrum*. *J Bacteriol* **89**: 1402–1412.

20. Hu, X., Ritz, T., Damjanović, A., Autenrieth, F., and Schulten, K. (2002) Photosynthetic apparatus of purple bacteria. *Q Rev Biophys* **35**: 1–62.

21. Kiley, P.J., and Kaplan, S. (1988). Molecular genetics of photosynthetic membrane biosynthesis in *Rhodobacter sphaeroides*. *Microbiol Rev* **52**: 50-69.

22. Lučić, V., Förster, F., and Baumeister, W. (2005) Structural studies by electron tomography: from cells to molecules. *Annu Rev Biochem* **74**: 833–865.

23. Mahmoudzadeh, A., Saer, R., Jun, D., Mirvakili, S.M., Takshi, A., Iranpour, B., *et al.* (2011) Photocurrent generation by direct electron transfer using photosynthetic reaction centres. *Smart Mater Struct* **20**: 94019.

24. Marko, M., Hsieh, C., Moberlychan, W., Mannella, C.A., and Frank, J. (2006) Focused ion beam milling of vitreous water: prospects for an alternative to cryo-ultramicrotomy of frozen-hydrated biological samples. *J Microsc* **222**: 42–47.

25. Niederman, R.A., Mallon, D.E., and Parks, L.C. (1979) Membranes of *Rhodopseudomonas sphaeroides*. VI. isolation of a fraction enriched in newly synthesized bacteriochlorophyll alpha-protein complexes. *Biochim Biophys Acta* **555**: 210–20.

26. Oelze, J., and Drews, G. (1972) Membranes of photosynthetic bacteria. *Biochim Biophys Acta* **265**: 209–39.

27. Olsen, J.D., Tucker, J.D., Timney, J.A., Qian, P., Vassilev, C., and Hunter, C.N. (2008) The organization of LH2 complexes in membranes from *Rhodobacter sphaeroides*. *J Biol Chem* **283**: 30772–30779.

28. Ormerod, J.G., Ormerod, K.S., and Gest, H. (1961) Light-dependent utilization of organic compounds and photoproduction of molecular hydrogen by photosynthetic bacteria; relationships with nitrogen metabolism. *Arch Biochem Biophys* **94**: 449-463.

29. Pfennig, N., and Lippert, K.D. (1966) Über das vitamin B_{12}-bedürfnis phototropher schwefelbakterien. *Arch Mikrobiol* **55**: 245-256.

30. Pierson, J., Vos, M., McIntosh, J.R., and Peters, P.J. (2011) Perspectives on electron cryo-tomography of vitreous cryo-sections. *Microscopy* **60**: S93–S100.

31. Prince, R.C., Baccarini-Melandri, A., Hauska, G.A., Melandri, B.A., and Crofts, A.R. (1975) Asymmetry of an energy transducing membrane. The location of cytochrome c_2 in *Rhodopseudomonas spheroides* and *Rhodopseudomonas capsulata*. *Biochim Biophys Acta - Bioenerg* **387**: 212–227.

32. Richter, K. (1994) A cryoglue to mount vitreous biological specimens for cryoultramicrotomy at 110K. *J Microsc* **173**: 143–147.

33. Rigort, A., Bäuerlein, F.J.B., Villa, E., Eibauer, M., Laugks, T., Baumeister, W., and Plitzko, J.M. (2012) Focused ion beam micromachining of eukaryotic cells for cryoelectron tomography. *Proc Natl Acad Sci U S A* **109**: 4449–54.

34. Rigort, A., and Plitzko, J.M. (2015) Cryo-focused-ion-beam applications in

structural biology. *Arch Biochem Biophys* **581**: 122–130.

35. Rigort, A., Villa, E., Bäuerlein, F.J.B., Engel, B.D., and Plitzko, J.M. (2012) Integrative approaches for cellular cryo-electron tomography. In *Methods in cell biology*. pp. 259–281.

36. Scheuring, S., Nevo, R., Liu, L.N., Mangenot, S., Charuvi, D., Boudier, T., *et al.* (2014) The architecture of *Rhodobacter sphaeroides* chromatophores. *Biochim Biophys Acta - Bioenerg* **1837**: 1263–1270.

37. Şener, M., Strümpfer, J., Hsin, J., Chandler, D., Scheuring, S., Hunter, C.N., and Schulten, K. (2011) Förster energy transfer theory as reflected in the structures of photosynthetic light-harvesting systems. *ChemPhysChem* **12**: 518–531.

38. Şener, M., Strümpfer, J., Singharoy, A., Hunter, C.N., and Schulten, K. (2016) Overall energy conversion efficiency of a photosynthetic vesicle. *Elife* **5**.

39. Şener, M.K., Olsen, J.D., Hunter, C.N., and Schulten, K. (2007) Atomic-level structural and functional model of a bacterial photosynthetic membrane vesicle. *Proc Natl Acad Sci U S A* **104**: 15723–15728.

40. Shimoni, E., Rav-Hon, O., Ohad, I., Brumfeld, V., and Reich, Z. (2005) Three-dimensional organization of higher-plant chloroplast thylakoid membranes revealed by electron tomography. *Plant Cell Online* **17**.

41. Stone, J.E., Sener, M., Vandivort, K.L., Barragan, A., Singharoy, A., Teo, I., *et al.* (2015) Atomic detail visualization of photosynthetic membranes with GPU-accelerated ray tracing. *Parallel Comput* **55**: 17–27.

42. Tauschel, H.-D., and Drews, G. (1967) Thylakoidmorphogenese bei *Rhodopseudomonas palustris*. *Arch für Mikrobiol* **59**: 381–404.

43. Tucker, J.D., Siebert, C.A., Escalante, M., Adams, P.G., Olsen, J.D., Otto, C., *et al.* (2010) Membrane invagination in *Rhodobacter sphaeroides* is initiated at curved regions of the cytoplasmic membrane, then forms both budded and fully detached spherical vesicles. *Mol Microbiol* **76**: 833-847.

44. Vatter, A.E. and Wolfe, R.S. (1958) The structure of photosynthetic bacteria. *J Bacteriol* 75: 480–488.

45. Verméglio, A., and Joliot, P. (1999) The photosynthetic apparatus of *Rhodobacter sphaeroides*. *Trends Microbiol* **7**: 435–440.

46. Verméglio, A., Lavergne, J., and Rappaport, F. (2016) Connectivity of the intracytoplasmic membrane of *Rhodobacter sphaeroides*: a functional approach. *Photosynth Res* **127**: 13–24.

47. Yaghoubi, H., Li, Z., Jun, D., Lafalce, E., Jiang, X., Schlaf, R., *et al.* (2014) Hybrid wiring of the *Rhodobacter sphaeroides* reaction center for applications in bio-photoelectrochemical solar cells. *J Phys Chem C* **118**: 23509–23518.

48. Yen, G.S.L., Cain, B.D., and Kaplan, S. (1984). Cell-cycle-specific biosynthesis of the photosynthetic membrane of *Rhodopseudomonda sphaeroides*: structural implications. *Biochim Biophys Acta--Biomembr* **777**: 41-55.

49. Yilmaz, L.S., Kontur, W.S., Sanders, A.P., Sohmen, U., Donohue, T.J., and Noguera, D.R. (2010) Electron partitioning during light- and nutrient-powered hydrogen production by *Rhodobacter sphaeroides*. *Bioenergy Res* **3**: 55–66.

CHAPTER 5

CONCLUDING REMARKS

The studies in this dissertation—though disparate—were united through the use of cryo-EM techniques to visualize the structure of cells and cellular components. In Chapter 2, we used EFTEM to document the phenomenological changes to *Aedes aegypti* spermatozoa stored in the male seminal vesicle, the female bursa, and the female spermathecae. Using the spermatozoa obtained from the seminal vesicles of sexually-matured, virgin males as a control, we concluded that spermatozoa undergo no appreciable phenomenological modifications while stored in the female's short-term storage organ, the bursa. Sperm stored in the female's long-term storage organ, the spermathecae, underwent significant structural modifications. These changes involved the removal of the sperm coat and the sperm's outer membrane. The structural modifications in spermatozoa were coupled with significant changes in sperm motility, ranging from a state of near-quiescence to hypermotility. Both of these phenomenological changes initiated within the first hour of storage within the spermathecae, and largely concluded twelve hours post-storage.

Additionally, these phenomenological changes to mosquito sperm correlated with the number of viable eggs a female mosquito laid. Eggs laid by mosquitoes less than two hours after insemination did not hatch; fecundity gradually increased beginning at four hours post-insemination and plateaued near twelve hours after insemination. Although

we could not prove causation, we concluded that changes to sperm morphology, motility, and female fecundity all occur concurrently. Furthermore, we provide baseline evidence suggesting the possibility that sperm modifications may play a role in fertilization in *Aedes aegypti* mosquitoes. A similar phenomenon, called capacitation, is well-described in humans and other mammals (Chang, 1951; Austin, 1951; Bedford, 1970; De Jonge, 2005). Uncovering the existence of an analogous process in *Aedes aegpyti* may provide alternative vector control strategies in this medically relevant mosquito species.

Future work will elucidate the molecular and proteomic basis for sperm modification and quiescence during storage in the spermathecae. The most critical studies will sequence the male seminal proteome and the female's spermathecal fluid proteome. Once the proteomes have been established, subsequent studies will seek to identify which proteome induces sperm modification and which induces quiescence (or alternatively, reactivation of stored sperm at later times post-mating). In the likely event that there are both male and female contributions to sperm modification and storage, decoupling the two may require additional work. Finally, we recognize that although sperm modification and storage occur within the same window of time, they may represent two independent processes with very different mechanisms. Untangling these two would be an additional source of challenging, yet very interesting future work.

Another remaining question is whether sperm modification is necessary for just storage or both storage and fertilization. This question could be addressed by attempting to fertilize eggs with unmodified sperm. These experiments are also best done *in vivo*, which poses additional challenges in an organism as small as a mosquito.

Once the fundamentals of sperm modification and storage have been clarified, the genes encoding the molecular machinery in *Aedes aegypti* could be modified to encode for specific outcomes that can make fertilization less successful in this mosquito species. Reducing—or even eliminating—the *Aedes aegypti* population can prevent millions of infections and hundreds of thousands of deaths around the world each year (Brady *et al.*, 2012; Bhatt *et al.*, 2013, WHO, 2018). The impact on public health cannot be understated, and future work could benefit not only the entomological and medical communities, but billions of people worldwide.

In Chapter 3, we assessed the feasibility of several techniques in understanding the morphology of non-tumeriogenic and tumeriogenic cell lines. We concluded that both 10A and HAS3 cells cultured directly onto TEM grids exhibited morphologies similar to those grown on traditional substrates, such as glass or a Petri dish. When controlling for individual cell lines, we determined that cells prepared for imaging with RT- and cryo-TEM had different morphologies. Cells imaged with RT-SEM appeared flatter but the 3D structure of the tubular extensions from the cells' surfaces remained preserved. Cells imaged with cryo-SEM appeared rounder, but the tubular extensions lay flat on the grid. We concluded that both morphologies are a consequence of the

sample preparation processes for both RT- and cryo-SEM. The cells prepared for RT-SEM were chemically fixed and dehydrated, and the removal of water content may cause the cells to appear flatter. Cells prepared for cryo-SEM were vitrified, and blotting cell samples before plunge freezing may have collapsed the tubular extensions.

Nevertheless, a combination of techniques revealed that HAS3 cells contain more and longer microtubular extensions from their surface. These extensions interact weakly with the substrate and neighboring cells. The extensions from HAS3 cells contained microvesicles along their lengths, suggesting an additional mechanism for trafficking vesicles into the extracellular matrix.

We also characterized vesicles secreted into the cell media. The diameters of vesicles secreted from HAS3 cells were analyzed with both cryo-TEM and NTA. Due to low sample statistics, the size distribution of vesicles secreted from 10A cells could not be evaluated. The NTA and cryo-TEM diameter distributions of HAS3 vesicles did not look the same. The cryo-TEM data contained a larger range of vesicles with a broader distribution, while NTA diameter distribution contained a smaller range of vesicles distributed into two primary peaks. Larger vesicles comprised a greater proportion of vesicles in the cryo-TEM data than in the NTA data. The differences in the ranges of the two distributions may be attributed to the fact that vesicles greater than 1000 nm are excluded from analysis by the NTA software. The difference in proportion of smaller-to-larger vesicles in the datasets could be attributed to lower sample statistics

in the cryo-TEM data, but also to the presence of biological debris in the cell media. While one can differentiate between vesicles and debris in cryo-TEM micrographs, the NTA software cannot differentiate between vesicular and non-vesicular debris, so the presence of debris likely affects the particle distribution in NTA data.

Cancer biology is a very challenging field that has benefitted from a suite of both microscopic and analytical techniques. Our study suggests that a single technique cannot provide a comprehensive assessment of cell morphology, vesicle biogenesis, and vesicle characterization. Instead, researchers must use a combination of techniques to provide insight into these phenomena with an understanding of the potential limitations associated with each technique.

Future studies are manifold. One direction is to develop a reliable, reproducible method of differentiating between exosomes and microvesicles. Right now, exosomes and microvesicles are typically distinguished by their diameters, but this strategy is not robust (Bobrie *et al.*, 2011). There is often overlap between the sizes of larger exosomes and smaller microvesicles, and, as seen from our study, particle tracking methods cannot always distinguish between vesicles and non-vesicular data. One potential solution is labeling specific populations of vesicles to be tracked with NTA (Dragovic *et al.*, 2011).

Another exciting area of future work would be the *in situ*, 3D visualization of vesicle secretion from parental cells. For these studies to be successful, one must consider the following challenges: first, cancer cells are often several microns thick and may not

vitrify uniformly with plunge freezing. High pressure freezing will likely overcome this limitation, but requires access to expensive equipment. Second, microvesicle shedding occurs on the plasma membrane and has been visualized to some degree with both RT- and cryo-SEM. However, the cell's thickness even at its peripheries is often too great for high-resolution analysis of microvesicle secretion with cryo-TEM. Exosomes, which are housed completely within the cell, pose a greater challenge. Processes such as exosome trafficking and exocytosis are difficult—perhaps impossible—to visualize in whole cancer cells. The solution is to thin cells with cryo-FIB. This will not only produce an electron-transparent sample with potential for high-resolution imaging, but it will also provide access to the cell's cytoplasm, where exosomes can be visualized in their native state. As seen in Chapter 4, cryo-FIB can be combined with cryo-ET to provide 3D analysis of the development and secretion of extracellular vesicles. At the time of writing this thesis, such work has never been published, but would provide invaluable insight into the mechanisms of a disease that kills over half a million people a year in the US (Siegel *et al.*, 2018).

In Chapter 4, we used cryo-FIB and cryo-ET to probe the architecture of chromatophores in *Rhodobacter sphaeroides*. We found that chromatophore biogenesis initiates from the cytoplasmic membrane. Chromatophores maintain topological continuity with the cytoplasmic membrane during their development, and detach when mature. Mature chromatophores closest to the cell wall are mostly isolated, whereas chromatophores toward the center of the cell exist in both isolated and connected morphologies. Connected vesicles include clustered vesicles, which are

identified by the presence of a small bud protruding from the lipid bilayer of a developed chromatophore. This bud has access to the interior of the vesicle, and may be the result of the incorporation of proteins, pigments, and other membrane components into existing chromatophores after cell division. Chromatophores can also be connected to one or more neighboring chromatophores through small linkers, which are about 10 nm long and 5 nm wide. FRET suggests these linkers are physical, notfunctional, and their presence might be due to the specific light conditions under which the bacteria were grown. Although some centermost vesicles appeared to be truly isolated, the majority of centermost vesicles existed as connected structures. Additionally, we found that the chromatophores in aged *R. sphaeroides* fused with neighboring chromatophores, lost their spherical structure, and were greatly increased in volume. The morphology of vesicles in aged *R. sphaeroides* is likely the consequence of the aging process, and was unrelated to the connectivity in health bacteria. Our results suggest that chromatophores can adopt either isolated or connected morphologies within a single bacterium. This information may provide more fundamental insight into the arrangement of chromatophores in *R. sphaeroides* as well as inform the incorporation of chromatophores as the active components in biorenewable technologies.

Future work would attempt to locate and identify the positions of the bc_1 complex and ATP synthase on a single chromatophore. Previous studies have been unable to locate the bc_1 complex, although every chromatophore is presumed to have one (Geyer and Helms, 2006). Another unsolved problem is whether a chromatophore has one or two

ATP synthases. This question is complicated by the fact that an ATP synthase has yet to appear on a chromatophore in any microscopy data. One attempt at solving this problem involves using subtomogram averaging from existing cryo-ET data to generate a 3D model. If successful, the technique should elucidate the location of the ATP synthase, which is relatively large compared to the other proteins on a chromatophore surface. The model could potentially identify the bc_1 complex as well, or at least provide some insight into its potential location on a chromatophore.

Rhodobacter sphaeroides is a model organism that also served as a nice template to demonstrate the feasibility of advanced electron microscopy techniques. If I had more time, I would have liked to combine the techniques used in Chapter 4 to the projects in Chapters 2 and 3. I imagine that health, healthcare, and disease will pose some of this century's greatest challenges. It is my hope that future work in this group (and in general) will combine techniques such as cryo-FIB, cryo-ET, and others to understand the structural basis for disease. Current work in this area is dominated by SPA, which has been used to solve the structure of the Zika virus, tau filaments (which play a role in Alzheimer's disease), and α-synuclein fibrils (which play a role in Parkinson's disease), among others (Sirohi *et al.*, 2016; Kostyuchenko *et al.*, 2016; Fitzpatrick *et al.*, 2017; Guerrero-Ferreira *et al.*, 2018). However, I believe that a comprehensive assessment of disease will require an *in situ* understanding of unadulterated macromolecular assemblies, and their role in disease initiation and progression. To this end, I believe that cryo-ET will play an integral role in elucidating the mechanisms of disease, and informing future medical interventions.

REFERENCES

1. Austin, C.R. (1951) Observations on the penetration of the sperm in the mammalian egg. *Aust J Sci Res B* **4**: 581–96.

2. Bedford, J.M. (1970) Sperm capacitation and fertilization in mammals. *Biol Reprod Suppl* **2**: 128–58.

3. Bhatt, S., Gething, P.W., Brady, O.J., Messina, J.P., Farlow, A.W., Moyes, C.L., *et al.* (2013) The global distribution and burden of dengue. *Nature* **496**: 504–507.

4. Bobrie, A., Colombo, M., Raposo, G., and Théry, C. (2011) Exosome Secretion: Molecular Mechanisms and Roles in Immune Responses. *Traffic* **12**: 1659–1668.

5. Brady, O.J., Gething, P.W., Bhatt, S., Messina, J.P., Brownstein, J.S., Hoen, A.G., *et al.* (2012) Refining the Global Spatial Limits of Dengue Virus Transmission by Evidence-Based Consensus. *PLoS Negl Trop Dis* **6**: e1760.

6. Chang, M.C. (1951) Fertilizing Capacity of Spermatozoa deposited into the Fallopian Tubes. *Nature* **168**: 697–698.

7. Dragovic, R.A., Gardiner, C., Brooks, A.S., Tannetta, D.S., Ferguson, D.J.P., Hole, P., *et al.* (2011) Sizing and phenotyping of cellular vesicles using Nanoparticle Tracking Analysis. *Nanomedicine Nanotechnology, Biol Med* **7**: 780–788.

8. Fitzpatrick, A.W.P., Falcon, B., He, S., Murzin, A.G., Murshudov, G., Garringer, H.J., *et al.* (2017) Cryo-EM structures of tau filaments from Alzheimer's disease. *Nature* **547**: 185–190.

9. Geyer, T., and Helms, V. (2006) A Spatial Model of the Chromatophore Vesicles of Rhodobacter sphaeroides and the Position of the Cytochrome bc1 Complex. *Biophys J* **91**: 921–926.

10. Guerrero-Ferreira, R., Taylor, N.M.I., Mona, D., Ringler, P., Lauer, M.E., Riek, R., *et al.* (2018) Cryo-EM structure of alpha-synuclein fibrils. *bioRxiv* 276436.

11. Jonge, C. De (2005) Biological basis for human capacitation. *Hum Reprod Update* **11**: 205–214.

12. Kostyuchenko, V.A., Lim, E.X.Y., Zhang, S., Fibriansah, G., Ng, T.-S., Ooi, J.S.G., *et al.* (2016) Structure of the thermally stable Zika virus. *Nature* **533**: 425–428.

13. Siegel, R.L., Miller, K.D., and Jemal, A. (2018) Cancer statistics, 2018. *CA Cancer J Clin* **68**: 7–30.

14. Sirohi, D., Chen, Z., Sun, L., Klose, T., Pierson, T.C., Rossmann, M.G., and Kuhn, R.J. (2016) The 3.8 Å resolution cryo-EM structure of Zika virus. *Science* **352**: 467–70.

15. World Health Organization. (2018, May 1). Yellow Fever [Fact sheet]. Retrieved from http://www.who.int/news-room/fact-sheets/detail/yellow-fever.

APPENDIX

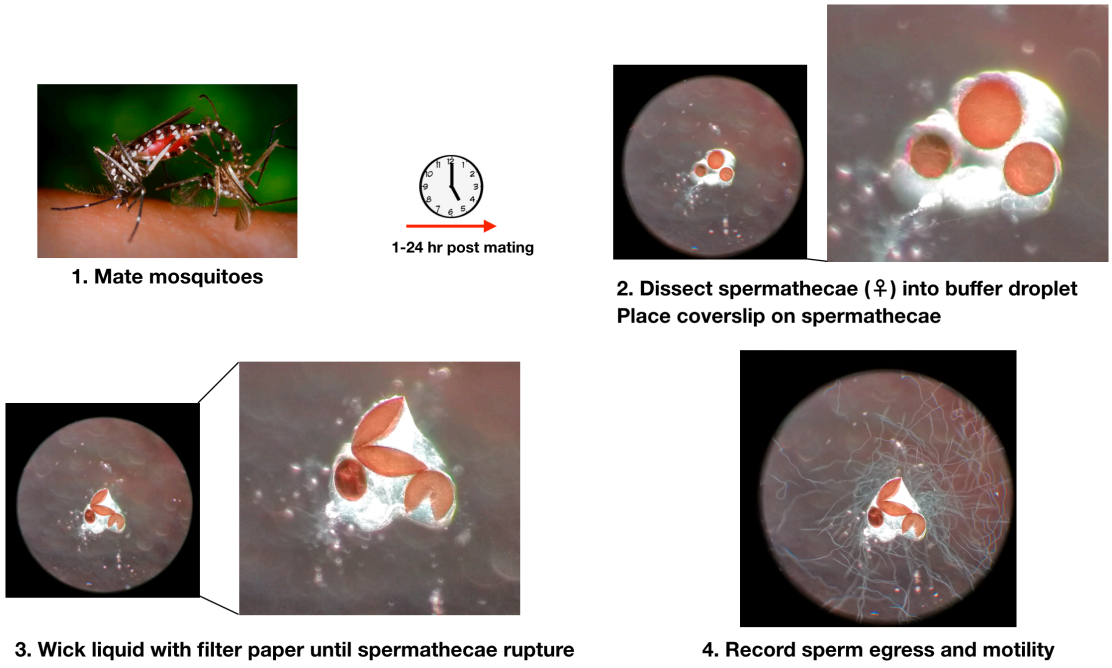

Fig. A.1. Sperm harvesting from the female spermathecae. *Aedes aegypti* male and females are mated in a 1:1 ratio (1). At a predetermined time 1-24 hours after mating, the spermathecae are dissected from the female into a droplet of buffer (2). The glass slide is covered with a cover slip, and fluid is wicked from beneath the cover slip with a piece of filter paper until the spermathecae crack (3). Sperm that leave the cracked spermathecae are either pipetted onto the TEM grid for vitrification, or their motility recorded.

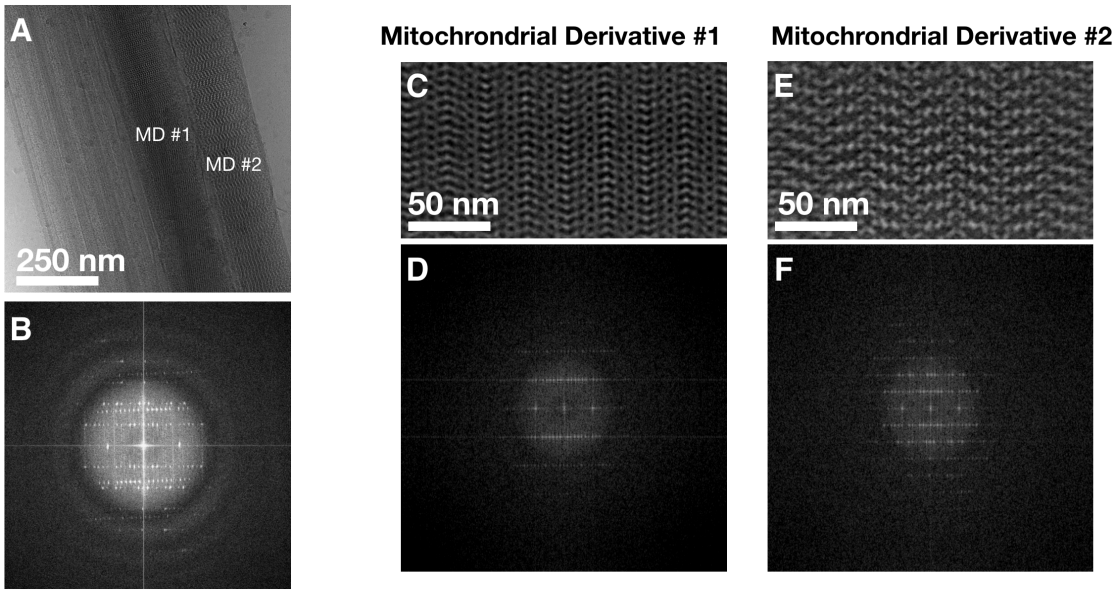

Fig. A.2. Paracrystalline structure in the mitochondrial derivatives. *Aedes aegypti* spermatozoa contain two MDs of approximately equal width (A). A Fourier transform of a region from the sperm flagellum shows periodic structure, largely due to the presence of the MDs and axoneme (B). Although resident within the same cytoplasm, and virtually identical in structure, the mitochondrial derivatives show different real space and FFT patterns (C-F). This highlights the differences in orientation of the individual MDs within the cytoplasm. *FFT scale bars: B: 250 nm^{-1}, D: 50 nm^{-1}, F: 50 nm^{-1}.*

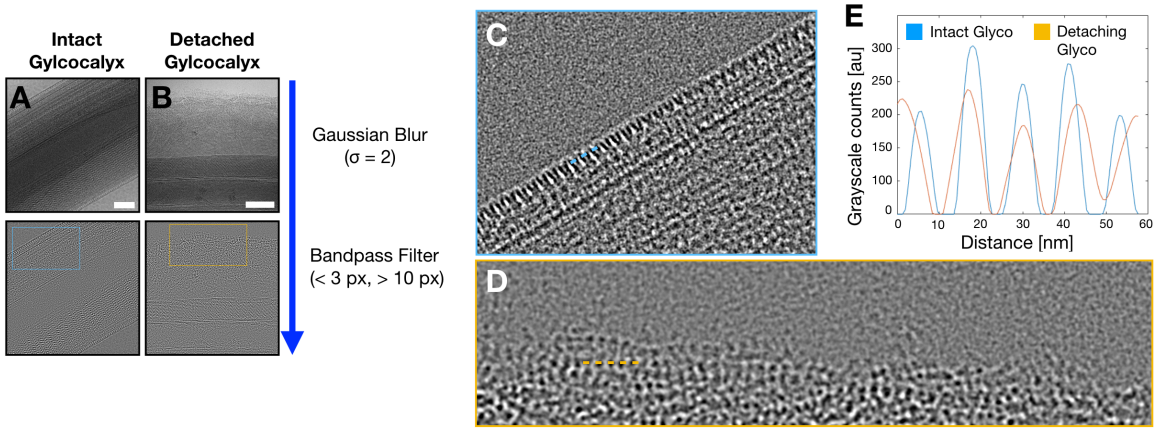

Fig. A.3. Organized structure of the sperm glycocalyx. *Aedes aegypti* spermatozoa contain a surface coat that has been previously described as a glycocalyx. The sperm glycocalyx in *Aedes aegypti* is organized and periodic, both when intact and as it is shed from the sperm.